COMPUTATIONAL STUDY OF INTERMETALLIC AND ALLOY MEMBRANES FOR HYDROGEN SEPARATION

A Thesis
Presented to
The Academic Faculty

by

Nita Chandrasekhar

In Partial Fulfillment
of the Requirements for the Degree
Doctor of Philosophy in the
School of Chemical & Biomolecular Engineering

Georgia Institute of Technology
May 2014

COMPUTATIONAL STUDY OF INTERMETALLIC AND ALLOY MEMBRANES FOR HYDROGEN SEPARATION

Approved by:

Dr. David S. Sholl, Advisor
School of Chemical & Biomolecular Engineering
Georgia Institute of Technology

Dr. Michael A. Filler
School of Chemical & Biomolecular Engineering
Georgia Institute of Technology

Dr. Christopher W. Jones
School of Chemical & Biomolecular Engineering
Georgia Institute of Technology

Dr. Andrei G. Fedorov
School of Mechanical Engineering
Georgia Institute of Technology

Dr. C. David Sherrill
School of Chemistry and Biochemistry
Georgia Institute of Technology

Date Approved: March 21 2014

To my parents, S.Chandrasekhar and Uma Chandrasekhar

For their love, laughter, guidance and endless support without which none of this would be possible.

To my sister, Smita,

For her eternal patience, love and fun-filled discussions.

To my pooch, Whisky,

Who is the love of my life and best friend.

To little Shevy,

For helping me survive graduate school.

ACKNOWLEDGEMENTS

I would first like to thank my advisor and mentor Dr. David S. Sholl for his guidance and rigorous training during my years in graduate school. Every discussion during these years has aided in developing my research skills and critical thinking ability. He has supported my growth not only as a professional but as an overall human being. His continuous encouragement and guidance has greatly improved my technical writing skills in addition to honing my abilities in all aspects of scientific research. His time-management skills, attention to details and impeccable work ethics are very inspiring and I wish to emulate these qualities throughout my career. It was an honor to have Dr.Sholl as my PhD advisor.

I would like to thank my thesis committee members, Dr. Christopher W. Jones, Dr. Michael A. Filler, Dr. C. David Sherrill and Dr. Andrei G. Fedorov, all eminent scientists, for their useful discussions and inputs. Their suggestions, comments and questions over the years improved the quality of my work significantly and enabled me to think deeply about my work.

I wish to thank the School of Chemical & Biomolecular Engineering for providing me all facilities to carry out my research. In particular, I would like to thank the personnel at the Georgia Tech Partnership for an Advanced Computing Environment (PACE) for their help and support. I would like to personally thank Dr. Wesley Emeneker for his prompt response, detailed help and interest. He has been instrumental in helping me complete my thesis despite many computing issues and has taught me a great deal about dealing with large computing clusters and useful scripting.

I was fortunate to work with very bright people in my research group. I am thankful to Dr. Shiqiang Hao, Dr. Sung Gu Kang, Dr. Emmanuel Haldoupis, Namory Keita, Dr. Melissa Lucero, Dieh Teng, Liwei Li, Rohan Awati, Kelly Nicholson and Daniel S.Wei for their help and discussions.

I was fortunate to find great friends in Atlanta who made it possible for me to complete my studies. Their encouragement and help in making my life fun and comfortable away from home is invaluable. I am particularly thankful to Ramanan, Manoj, Barani, Veena and Krishna among many others who have supported me over the years.

Most importantly, I would like to thank my family – my parents and my sister. If it were not for them, none of this would have been possible. They have always insisted upon education and allowed me to follow my dreams. They have supported and encouraged me during difficult times and celebrated my successes. They have always believed in my abilities and motivated me to strive for the best in everything I do. I am eternally grateful for everything they have done and hope to fulfil their expectations to the best of my ability. I am also very grateful to enjoy the company of my beloved pooch Whisky who has made every day joyful and helped me overcome every hurdle in his own way.

Nita Chandrasekhar, 6th March 2014

TABLE OF CONTENTS

LIST OF TABLES

LIST OF FIGURES

Page

SUMMARY

Metal membranes are useful for hydrogen separation from mixed gas streams. They can exhibit perfect selectivity for hydrogen. However, in order to be commercially viable, in addition to providing high hydrogen fluxes, they must also be resistant to poisoning, possess long operating lifetimes and be cost effective. Many types of metal membranes such as pure metals, disordered alloys and amorphous metals have been studied for this application. In this work, we aim to identify intermetallic stoichiometric compounds of two or more metals that could be used as potential membrane materials for hydrogen separation. In the past, first principle calculations combined with Monte Carlo methods have been developed that can accurately predict H_2 fluxes through metal membranes at different hydrogen pressures and temperatures. Although these models are accurate, they are computationally intensive. In this work, we use these methods and develop screening criteria based on calculated properties that enable us to perform detailed calculations on a diminishing set of materials and rapidly identify the favorable candidates for hydrogen separation. We screened 1059 intermetallics at this high level of theory, which is the largest set of materials studied for this application. We divided the intermetallics into Pd-based and non-Pd based materials using additional screening algorithms to reduce the number of calculations required to identify potential candidate materials. 8 intermetallics were identified that had permeabilities that was comparable or higher to that of pure Pd. $MgZn_2$ and MnTi were found to have the highest H permeabilities among all the intermetallics studied. In addition to ground state structures, metastable structures were also found to be stabilized in the presence of hydrogen. Our

work demonstrates the ability of these computational methods to identify potential novel materials for specific applications from large sets of materials that would not be possible experimentally.

In the models for hydrogen permeability developed above, H-induced metal lattice rearrangements were not considered. Experimental evidence suggests that hydrogen heat treated (HHT) Pd-Au alloys undergo lattice rearrangement that results in an ordered structure which has a higher solubility than the non-HHT alloys. Using a combination of cluster expansion methods developed for predicting hydrogen permeability of disordered alloys and Monte Carlo methods, we predicted the extent of H induced lattice rearrangement in $Pd_{96}Au_4$ and $Pd_{85}Au_{15}$ alloys. We also predicted the solubility, diffusivity and permeability of these rearranged phases and found that their H permeability is higher than the non-rearranged phases. Our models capture the H-induced lattice rearrangement and provide useful insight of the conditions where this phenomenon is significant. Using the tools developed in this work, similar alloys that have a tendency to undergo lattice rearrangement that results in enhanced H permeability can be identified.

PART 1: INTERMETALLICS

CHAPTER 1

INTRODUCTION

Hydrogen is an important energy source for the future given its favorable properties as a fuel. The majority of H_2 is currently generated from fossil fuel sources (steam reforming or partial oxidation of hydrocarbons) while the remainder is generated from electrolysis of water[1]. Separation of hydrogen from mixed gas streams is important since fuel-cell technology requires high-purity hydrogen[2]. In extraction of hydrogen using fossil fuels, it is necessary to separate and purify H_2 from mixed gas streams containing other gases such as CO_2 and H_2S[2].

1.1 Metal Membranes

Membrane separations have potential advantages over other approaches to hydrogen purification. Many different types of membranes including metallic alloys, composites, polymer membranes and inorganic membranes have been considered for hydrogen separations [1, 3, 4]. Metal membranes are ideal for use at high temperatures since they have high thermal stabilities at elevated temperatures. The physical mechanism of hydrogen transport through metal membranes involves adsorption of hydrogen, catalytic dissociation of hydrogen into H atoms on the surface, absorption of H atoms into the membrane, diffusion of H atoms through the membrane, formation of hydrogen molecules from H atoms on the permeate side and dissociation of hydrogen gas from the membrane[5]. Pure Pd remains widely used for hydrogen selective membranes despite challenges associated with hydrogen embrittlement and sulfur poisoning [6]. Alloying Pd with other metals such as Ag, Au, and Cu can reduce some of the shortcomings associated with pure Pd membranes. A large number of papers on the performance of pure Pd and Pd alloy membranes for hydrogen separation are available [3, 5, 7-13]. In addition to experimental methods, first principles-based calculations have been applied

to the task of finding Pd alloys with suitable membrane properties. The predicted properties using these predictive modeling methods are found to be in excellent agreement with experimental results [6, 14-20].

Amorphous metal membranes are another class of metal membranes that have been studied. Amorphous membranes possess short range order but no long range order, unlike crystalline materials. Studies and experiments conducted on a number of materials consisting of Zr-Ni, Zr-Ni-Nb and Fe-B have shown promising results [21-24]. Theoretical predictions backed by quantum chemistry calculations characterizing the performance of these membranes have accelerated their development [17, 19, 25, 26].

1.2 Intermetallics

The work on crystalline metal alloys summarized above focused exclusively on substitutionally disordered alloys. In many instances, however, alloying two metals leads to the formation of intermetallic compounds [27]. Intermetallic compounds are characterized by well-defined stoichiometric compositions and crystalline order. The structure of the intermetallic FeNi is shown in Fig.1.1. FeNi has a cubic Fm-3m structure.

Intermetallics can have properties and crystal structures that differ from their constituent metals [28]. The ability of intermetallics to absorb hydrogen gas makes them potential candidates for hydrogen storage materials and intermetallic hydrides have been studied extensively for this purpose [29]. In the next few chapters, we examine binary stoichiometric intermetallics as potential membrane materials for hydrogen separation applications. Considering this class of materials will considerably extend the existing work that has been done on disordered alloys and amorphous metals. Pure Pd is a known to show excellent hydrogen permeability properties and is used as a benchmark for this study.

One motivation for considering intermetallics as membranes is their potential thermodynamic stability with respect to contaminants. A critical failure mechanism for membranes when used for feed streams containing sulfur is the formation of bulk sulfides [6, 7, 30]. Thermodynamic calculations have been used to assess sulfide formation for disordered Pd binary alloys but the resistance of the alloys examined to date for sulfide formation is limited [31]. Intermetallic phases exist because they are more thermodynamically stable than the disordered alloys that can form with the same composition. It is therefore reasonable to expect that intermetallics may be less susceptible to sulfide formation than disordered alloys. This property however, would only be useful if intermetallics with high H permeability can be identified.

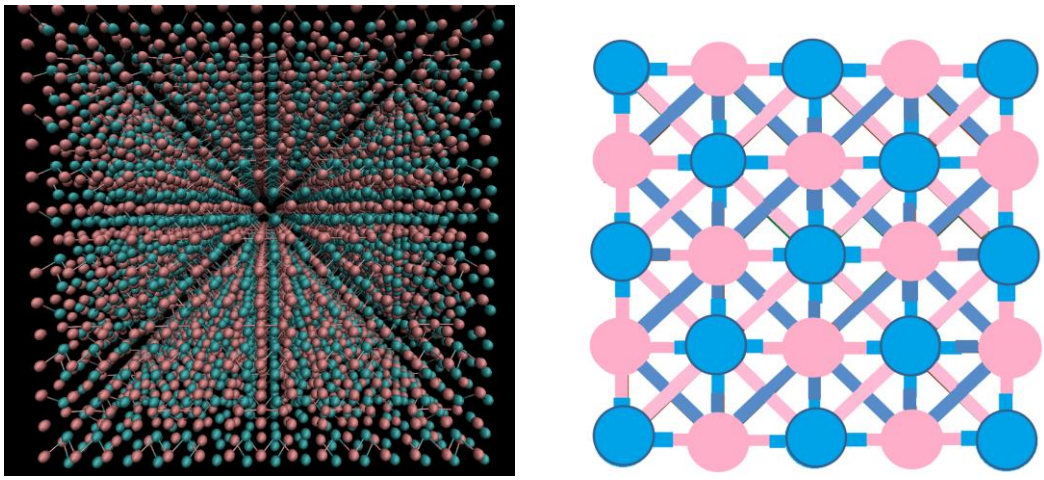

Figure 1.1: Structure of intermetallic FeNi. Fe (Ni) is represented by pink (blue) spheres. On the left is the bulk structure of FeNi and on the right is a unit cell. FeNi has a well-defined structure (fcc) and stoichiometric composition characteristic of intermetallics.

Thousands of distinct intermetallics exist in nature. The Inorganic Crystal Structure Database (ICSD) lists 2400 stoichiometric intermetallic compounds [32]. Previous studies examining large numbers of potential membrane materials have shown that most materials have very low H permeability relative to Pd [33, 34]. This suggests systematically exploring large numbers of intermetallics as membranes experimentally is likely to be unproductive. In the following chapters, we show that quantitative DFT-

based models can be used to efficiently predict the membrane performance of a large number of intermetallics.

1.3 Scope of work

In this work, we describe a screening procedure developed to predict hydrogen permeabilities of intermetallic membranes based on quantum chemistry calculations. This screening method uses only prior knowledge of the crystal structure and composition of the intermetallic as an input, making it invaluable for large-scale screening of candidate materials for hydrogen separation. Plane-wave Density Functional Theory (DFT) calculations [35] are well suited to quantitatively describing the properties of interstitial H in metals [20, 36]. DFT calculations in combination with Kinetic Monte Carlo methods are used to calculate the diffusivity of hydrogen in intermetallics. The details of calculations performed to predict hydrogen permeability of an intermetallic membrane are described in Chapter 2. In Chapter 3, the screening algorithm developed to study hundreds of binary intermetallics using DFT methods is described. This algorithm is based on the methods and screening criteria described in Chapter 2 that permit rapid evaluation of hundreds of binary intermetallics using minimal calculations. In Chapters 4 and 5, the results of the computational study of Pd-based and all binary intermetallics are described. In addition to screening ground-state structures of the Pd-based intermetallics, we performed calculations on metastable structures to determine their stability in the presence of hydrogen. In Chapter 5, we studied 981 non-Pd based intermetallic and shortlisted 8 materials that were predicted to have H permeability comparable to pure Pd.

1.4 References

[1] N.W. Ockwig, T.M. Nenoff, Membranes for hydrogen separation, Chemical Reviews, 107 (2007) 4078-4110.

[2] B.C.H. Steele, A. Heinzel, Materials for fuel-cell technologies, Nature, 414 (2001) 345-352.

[3] D.S. Sholl, Y.H. Ma, Dense Metal Membranes for the Production of High-Purity Hydrogen, MRS Bulletin, 31 (2006) 770-773.

[4] J.W. Phair, R. Donelson, Developments and Design of Novel (Non-Palladium-Based) Metal Membranes for Hydrogen Separation, Ind. Eng. Chem. Res., 45 (2006) 5657-5674.

[5] S.N. Paglieri, J.D. Way, Innovations in palladium membrane research, Sep. Purif. Methods, 31 (2002) 1-169.

[6] B.D. Morreale, B.H. Howard, O. Iyoha, R.M. Enick, C. Ling, D.S. Sholl, Experimental and computational prediction of the hydrogen transport properties of Pd_4S, Ind. Eng. Chem. Res., 46 (2007) 6313-6319.

[7] A. Kulprathipanja, G.O. Alptekin, J.L. Falconer, J.D. Way, Pd and Pd-Cu membranes: inhibition of H_2 permeation by H_2S, Journal of Membrane Science, 254 (2005) 49-62.

[8] N. Watanabe, H. Yukawa, T. Nambu, Y. Matsumoto, G.X. Zhang, M. Morinaga, Alloying effects of Ru and W on the resistance to hydrogen embrittlement and hydrogen permeability of niobium, Journal of Alloys and Compounds, 477 (2009) 851-854.

[9] H. Yukawa, G.X. Zhang, N. Watanabe, M. Morinaga, T. Nambu, Y. Matsumoto, Analysis of hydrogen diffusion coefficient during hydrogen permeation through niobium and its alloys, Journal of Alloys and Compounds, 476 (2009) 102-106.

[10] V. Gryaznov, Metal containing membranes for the production of ultrapure hydrogen and the recovery of hydrogen isotopes, Sep. Purif. Methods, 29 (2000) 171-187.

[11] P. Kamakoti, D.S. Sholl, A comparison of hydrogen diffusivities in Pd and CuPd alloys using density functional theory, J. Membr. Sci., 225 (2003) 145-154.

[12] T.M. Nenoff, R.J. Spontak, C.M. Aberg, Membranes for hydrogen purification: An important step toward a hydrogen-based economy, MRS Bulletin, 31 (2006) 735-741.

[13] M.D. Dolan, Non-Pd BCC alloy membranes for industrial hydrogen separation, J. Membr. Sci., 362 (2010) 12-28.

[14] L. Semidey-Flecha, C. Ling, D.S. Sholl, Detailed first-principles models of hydrogen permeation through PdCu-based ternary alloys, J. Membr. Sci., 362 (2010) 384-392.

[15] K.C. Kim, A.D. Kulkarni, J.K. Johnson, D.S. Sholl, Large-scale screening of metal hydrides for hydrogen storage from first-principles calculations based on equilibrium reaction thermodynamics, Physical Chemistry Chemical Physics, 13 (2011) 7218-7229.

[16] K.E. Coulter, J.D. Way, S.K. Gade, S. Chaudhari, D.S. Sholl, L. Semidey-Flecha, Predicting, Fabricating, and Permeability Testing of Free-Standing Ternary Palladium-Copper-Gold Membranes for Hydrogen Separation, Journal of Physical Chemistry C, 114 (2010) 17173-17180.

[17] S.Q. Hao, D.S. Sholl, Self-diffusion and macroscopic diffusion of hydrogen in amorphous metals from first-principles calculations, Journal of Chemical Physics, 130 (2009) 244705.

[18] L. Semidey-Flecha, S.Q. Hao, D.S. Sholl, Predictions of H isotope separation using crystalline and amorphous metal membranes: A computational approach, Journal of the Taiwan Institute of Chemical Engineers, 40 (2009) 246-252.

[19] S.Q. Hao, D.S. Sholl, Using first-principles calculations to accelerate materials discovery for hydrogen purification membranes by modeling amorphous metals, Energy & Environmental Science, 1 (2008) 175-183.

[20] S.V. Alapati, J.K. Johnson, D.S. Sholl, Large-scale screening of metal hydride mixtures for high-capacity hydrogen storage from first-principles calculations, Journal of Physical Chemistry C, 112 (2008) 5258-5262.

[21] M.D. Dolan, N.C. Dave, A.Y. Ilyushechkin, L.D. Morpeth, K.G. McLennan, Composition and operation of hydrogen-selective amorphous alloy membranes, J. Membr. Sci., 285 (2006) 30-55.

[22] S. Hara, K. Sakaki, N. Itoh, H.M. Kimura, K. Asami, A. Inoue, An amorphous alloy membrane without noble metals for gaseous hydrogen separation, J. Membr. Sci., 164 (2000) 289-294.

[23] S. Yamaura, S. Nakata, H. Kimura, Y. Shimpo, M. Nishida, A. Inoue, Hydrogen permeation of the melt-spun Ni-X-Zr amorphous membranes, Materials Transactions, 46 (2005) 1768-1770.

[24] S. Yamaura, M. Sakurai, M. Hasegawa, K. Wakoh, Y. Shimpo, M. Nishida, H. Kimura, E. Matsubara, A. Inoue, Hydrogen permeation and structural features of melt-spun Ni-Nb-Zr amorphous alloys, Acta Materialia, 53 (2005) 3703-3711.

[25] S.Q. Hao, D.S. Sholl, Comparison of first principles calculations and experiments for hydrogen permeation through amorphous ZrNi and ZrNiNb films, J. Membr. Sci., 350 (2010) 402-409.

[26] S. Hao, D.S. Sholl, First-Principles Models of Facilitating H_2 Transport through Metal Films Using Spillover, The Journal of Physical Chemistry C, 117 (2012) 1217-1223.

[27] R.W. Cahn, Intermetallics: new physics, Contemporary Physics, 42 (2001) 365-375.

[28] K.H.J. Buschow, Intermetallic Compounds of Rare-Earth and 3d Transition-Metals, Rep Prog Phys, 40 (1977) 1179-1256.

[29] R. Griessen, A. Driessen, D.G. Degroot, Search For New Metal Hydrogen Systems for Energy-Storage, Journal of the Less-Common Metals, 103 (1984) 235-244.

[30] C.P. O'Brien, B.H. Howard, J.B. Miller, B.D. Morreale, A.J. Gellman, Inhibition of hydrogen transport through Pd and $Pd_{47}Cu_{53}$ membranes by H_2S at 350 degrees C, J. Membr. Sci., 349 (2010) 380-384.

[31] K.C. Kim, S.G. Kang, D.S. Sholl, Predictions of Sulfur Resistance in Metal Membranes for H_2 Purification Using First-Principles Calculations, Industrial & Engineering Chemistry Research, 51 (2011) 301-309.

[32] G. Bergerhoff, I.D. Brown, Crystallographic Databases, International Union of Crystallography, Chester, 1987.

[33] C. Ling, D.S. Sholl, First principles investigation of metal sulfides as membranes in hydrogen purification, Journal of Membrane Science, 329 (2009) 153-159.

[34] S.G. Kang, K.E. Coulter, S.K. Gade, J.D. Way, D.S. Sholl, Identifying Metal Alloys with High Hydrogen Permeability Using High Throughput Theory and Experimental Testing, The Journal of Physical Chemistry Letters, 2 (2011) 3040-3044.

[35] D.S. Sholl, J. A.Steckel, Density Functional Theory: A Practical Introduction, John Wiley & Sons Inc. , 2009.

[36] P. Kamakoti, B.D. Morreale, M.V. Ciocco, B.H. Howard, R.P. Killmeyer, A.V. Cugini, D.S. Sholl, Prediction of hydrogen flux through sulfur-tolerant binary alloy membranes, Science, 307 (2005) 569-573.

CHAPTER 2

COMPUTATIONAL METHODS

Plane-wave density functional theory calculations were performed using the Vienna *ab initio* simulation package (VASP) [1-4]. DFT calculations were performed with the PW91 generalized gradient approximation functional using the projector augmented wave method [5-8]. Experimental crystal structures and lattice parameters were obtained from the ICSD [9]. A cut-off energy value of 250 eV was used and geometries were relaxed using a conjugate gradient method until the forces on all atoms were less than 0.03 eV/Å. The geometric relaxation to obtain the lattice parameters was performed using a dense k-point mesh to sample the reciprocal space and relaxing the lattice constants and all internal coordinates.

In this work, bulk diffusion and not surface reactions, was assumed to be the rate-limiting step. Surface reactions could be included in the model used to describe permeability, but this is outside the scope of this work [10]. Under the assumption that bulk diffusion is rate limiting, the concentration of hydrogen atoms in the metal θ_H are in equilibrium with the ambient hydrogen pressure [11]. At dilute hydrogen loadings i.e. $H/M < 0.1$, θ_H is given by Sieverts' Law. For higher hydrogen loadings, Grand Canonical Monte Carlo techniques are used to obtain the hydrogen solubility by equating the chemical potential of hydrogen in the gas phase and dissolved hydrogen [12]. However, the dilute loading assumption was found to be valid for a wide range of T and P for Pd and Pd-alloys [11]. Hence, this assumption was used to calculate the solubility of the Pd-based intermetallics.

2.1 Solubility

An intermetallic compound has a well-defined crystalline structure but does not always conform to one of the simple lattice structures (e.g. fcc,bcc, or hcp). This means that manual prediction of possible binding sites for the large collection of materials we consider would be difficult. Instead we adapted an automated method developed previously for amorphous materials by Hao and Sholl [13]. This method initially places hydrogen atoms on a grid inside the metal lattice and then computes the positions of hydrogen where the potential energy of the H atom is at a minimum using empirical Lennard-Jones potentials. This calculation gives an estimate of the location of the binding sites in the material. These initial estimates were used as the starting configurations for DFT calculations that minimized the system's energy while allowing all atoms (metal and H) to relax. The unit cell volume was held fixed in these calculations. This approach assumes that lattice expansion caused by the interstitial hydrogen is minimal, a reasonable assumption for materials in which the loading of interstitial H is low. The highest H concentration used in these calculations was one H in a super cell of 32 metal atoms. For materials with more than 32 metal atoms in the crystal unit cell, binding energies were calculated with one H atom in the unit cell.

The binding energies of each interstitial site is defined by [11]

$$E_b = E_{H-Metal} - E_{Metal} - \frac{1}{2} E_{H_2} \qquad (1)$$

where $E_{H-Metal}$ is the energy of the metal atoms including the hydrogen, E_{Metal} is the total energy of the bare metal and E_{H_2} is the total energy of a hydrogen molecule. We also calculated the vibrational frequencies and zero point energies of interstitial H using DFT. The frequencies were calculated by making small displacements of the H around the local minima at the binding sites with the assumption that the vibration of the interstitial H atom is decoupled from the phonons of the metal lattice [14]. Once the binding energy of each interstitial site and the zero point energies were available, the net

solubility of H was calculated using the method defined by Kamakoti and Sholl, which includes the effects of the multiple vibrational energy levels available to interstitial H atoms [11].

2.1.1 Solubility as a screening parameter

The hydrogen permeability of a dense metal membrane depends upon both solubility and diffusivity of interstitial H in the material. If the solubility is extremely low, however, then even a high diffusivity would lead to a low permeability value [15]. Thus, we use solubility as an initial screening parameter to remove the materials that would show extremely low permeability to hydrogen from being considered as potential candidates for hydrogen separation. The DOE target for hydrogen membranes for 2015 specifies operating temperatures of 250-500 ºC (523-773 K) [16]. We therefore consider solubility of H at 600 K. The solubility of H at a pressure of 1 atm H_2 in pure Pd at 600 K is 0.02 hydrogen per metal atom (H/M) [11]. To accommodate the possibility that a material could have diffusivity that is higher than pure Pd, resulting in equal or higher permeability than pure Pd, we use a cutoff value of H/M = 10^{-5} for the solubility as a screening value. Materials that are predicted to have solubility lower than 10^{-5} are considered to be unsuitable materials for hydrogen separation membranes and we did not examine H diffusion in these materials.

Materials that have solubility greater than ~0.1 H/M cannot be considered under the dilute loading assumption and hence their solubility cannot be calculated using Sievert's law. These materials have very favorable binding energies for hydrogen and show a high probability of forming hydride phases at the hydrogen pressures relevant for membrane operation. These materials are undesirable as membranes since the change in lattice constants associated with the metal to metal hydride transformation can lead to poor membrane integrity [17]. We therefore did not further consider materials with solubility > 0.1 H/M at 600 K as candidate membrane materials.

2.2 Diffusivity

We computed the overall solubility of H in a large number of Pd-based intermetallics. As just described, crystalline materials in which the solubility is too low ($H/M < 10^{-5}$) or too high ($H/M > 0.1$) will not lead to useful membrane materials. Materials between these extremes, however, have potential to show significant permeability if the diffusion of interstitial H is fast enough. In metals at moderate temperatures, interstitial diffusion occurs by discrete hops of H atoms from one binding site to another through a transition state. A rigorous method to compute the diffusivity of hydrogen in a metal when it moves by this mechanism has been developed previously using Kinetic Monte Carlo (KMC) [18]. This method requires the hopping rate between adjacent sites to be known, which in turn requires identification of transition states between binding sites. For efficient determination of transition states, a scheme developed by Hao and Sholl for amorphous materials was used [13]. This method identifies two adjacent binding sites separated by a search radius and generates a reasonable approximate location of the transition state. Once, the transition state has been estimated in this way, DFT can be used efficiently to rigorously locate the transition state and the zero point energy associated with this state. Site to site hopping rates were calculated from this information using quantum corrected harmonic transition state theory [18, 19].

2.2.1 Activation energy as a screening parameter

Prior to using KMC to determine the diffusivity, the activation barrier to every local diffusion path was considered to estimate the lowest barrier to diffuse through the material. The potential energy surface was mapped by determining the transition states using the algorithm described above. Once all the transition states and binding sites were known, the paths from one of the most favorable binding energy sites to another similar site were mapped. The minimum energy difference that must be overcome for hydrogen

to hop between the most favorable sites was taken as an estimate of the net activation energy barrier. If the estimated barrier was higher than 0.6 eV, no KMC calculations were performed on the material. This range of activation barrier energy (up to 0.6 eV) was chosen to accommodate the possibility of having a material with high solubility such that the permeability (product of diffusivity and solubility) would be in the favorable range. An activation energy barrier higher than 0.6 eV results in very low diffusivity values that would render the material unsuitable for membrane applications.

For the materials whose estimated barrier is lower than 0.6 eV, KMC was used to simulate the diffusivity of H using a large system and periodic boundary conditions (6×6×6 unit cells of the material). The simulation sizes vary from 864 atoms to greater than 2000 atoms for some larger unit cells. The minimum size (864 atoms) was shown to be sufficient by tests with larger cells. A minimum of 80 and a maximum of 100 H atoms were randomly distributed across the host metal. In the KMC simulation, each particle is uncorrelated (i.e. H-H interactions are explicitly ignored), so the KMC calculations correspond to a dilute loading of H in the metal. 5000 equilibration steps and 50,000 MC steps per H atom were performed to define trajectories of the diffusing atoms. Einstein's equation was then used to determine the diffusivity of H in the materials [18, 19].

2.3 Permeability

Once the solubility and diffusivity of H in a metal is known, the net permeability of H through the metal can be calculated [11, 15]. Hydrogen transport through a membrane is quantified in terms of permeability or flux. Using Fick's law and Sieverts' law, the net flux through the membrane can be written as

$$\text{flux} = \frac{1}{2} K_s D_s \frac{(P_{H,perm}^{0.5} - P_{H,ret}^{0.5})}{L} \qquad (2)$$

where D_s is the diffusivity and K_s is the Sieverts' constant in the membrane, $P_{H,ret}$ and $P_{H,perm}$ are the partial pressures of H_2 on the retentate and permeate side, and L is the membrane thickness[20]. This expression is valid for membranes in which transport though the bulk material is the rate-limiting step for permeation of hydrogen, not processes associated with the surfaces of the membrane [21, 22]. This limit is typically appropriate for describing metal membranes under practical operating conditions for H_2 purification. The above equation can be rewritten as [11, 15, 23]

$$\text{flux}=k\frac{(P_{H,perm}^{0.5}-P_{H,ret}^{0.5})}{L} \quad (3)$$

where $k=\frac{1}{2}K_sD_s$ is the permeability.

The definition of permeability makes it independent of the operating pressure and thickness. Using the methods outlined above, the permeability for individual intermetallics is computed without any experimental inputs. The permeability for H through Pd ranges from 10^{-8} to 10^{-6} mol/m/s/$Pa^{0.5}$ in a temperature range from 500-1000 K [11], and materials that could be used in practical settings need to have permeability that is similar or larger than pure Pd. Permeability of H in a temperature range from 600-1000 K was computed for materials that satisfied both the solubility and diffusivity screening criteria defined above. The intermetallics are broadly divided into two categories: Pd-based intermetallics, where one constituent element is Pd, and non-Pd based intermetallics. The results of the calculations performed for Pd and non-Pd based intermetallic membranes are discussed in chapters 4 and 5, respectively.

2.4 References

[1] G. Kresse, J. Hafner, Ab initio molecular dynamics for liquid metals, Physical Review B, 47 (1993) 558-561.

[2] G. Kresse, J. Hafner, Ab initio molecular-dynamics simulation of the liquid-metal–amorphous-semiconductor transition in germanium, Physical Review B, 49 (1994) 14251-14269.

[3] G. Kresse, J. Furthmüller, Efficiency of ab-initio total energy calculations for metals and semiconductors using a plane-wave basis set, Comput. Mater. Sci., 6 (1996) 15-50.

[4] G. Kresse, J. Furthmüller, Efficient iterative schemes for ab initio total-energy calculations using a plane-wave basis set, Physical Review B, 54 (1996) 11169-11186.

[5] G. Kresse, D. Joubert, From ultrasoft pseudopotentials to the projector augmented-wave method, Physical Review B, 59 (1999) 1758-1775.

[6] P.E. Blöchl, Projector augmented-wave method, Physical Review B, 50 (1994) 17953-17979.

[7] J.P. Perdew, J.A. Chevary, S.H. Vosko, K.A. Jackson, M.R. Pederson, D.J. Singh, C. Fiolhais, Atoms, molecules, solids, and surfaces: Applications of the generalized gradient approximation for exchange and correlation, Physical Review B, 46 (1992) 6671-6687.

[8] J.P. Perdew, J.A. Chevary, S.H. Vosko, K.A. Jackson, M.R. Pederson, D.J. Singh, C. Fiolhais, Erratum: Atoms, molecules, solids, and surfaces: Applications of the generalized gradient approximation for exchange and correlation, Physical Review B, 48 (1993) 4978-4978.

[9] G. Bergerhoff, I.D. Brown, Crystallographic Databases, International Union of Crystallography, Chester, 1987.

[10] C. Ling, D.S. Sholl, Using first-principles calculations to predict surface resistances to H_2 transport through metal alloy membranes, J. Membr. Sci., 303 (2007) 162-172.

[11] P. Kamakoti, B.D. Morreale, M.V. Ciocco, B.H. Howard, R.P. Killmeyer, A.V. Cugini, D.S. Sholl, Prediction of hydrogen flux through sulfur-tolerant binary alloy membranes, Science, 307 (2005) 569-573.

[12] S. Hao, D.S. Sholl, Computational prediction of durable amorphous metal membranes for H_2 purification, J. Membr. Sci., 381 (2011) 192-196.

[13] S.Q. Hao, D.S. Sholl, Comparison of first principles calculations and experiments for hydrogen permeation through amorphous ZrNi and ZrNiNb films, J. Membr. Sci., 350 (2010) 402-409.

[14] D.E. Jiang, E.A. Carter, Diffusion of interstitial hydrogen into and through bcc Fe from first principles, Physical Review B, 70 (2004) 064102.

[15] C. Ling, D.S. Sholl, First principles investigation of metal sulfides as membranes in hydrogen purification, Journal of Membrane Science, 329 (2009) 153-159.

[16] Materials Research, Small Business Innovation Research Program and Small Business Technology Transfer Program Office of Fossil Energy, 2005.

[17] N.W. Ockwig, T.M. Nenoff, Membranes for hydrogen separation, Chemical Reviews, 107 (2007) 4078-4110.

[18] P. Kamakoti, D.S. Sholl, Ab initio lattice-gas modeling of interstitial hydrogen diffusion in CuPd alloys, Physical Review B, 71 (2005) 9.

[19] L. Katz, M. Guinan, R.J. Borg, Diffusion of H_2, D_2, and T_2 in Single-Crystal Ni and Cu, Physical Review B, 4 (1971) 330-341.

[20] S.N. Paglieri, J.D. Way, Innovations in palladium membrane research, Sep. Purif. Methods, 31 (2002) 1-169.

[21] S. Hao, D.S. Sholl, First-Principles Models of Facilitating H_2 Transport through Metal Films Using Spillover, The Journal of Physical Chemistry C, 117 (2012) 1217-1223.

[22] B. Dai, D.S. Sholl, J.K. Johnson, First-principles investigation of adsorption and dissociation of hydrogen on Mg_2Si surfaces, J. Phys. Chem. C, 111 (2007) 6910-6916.

[23] L. Semidey-Flecha, D.S. Sholl, Combining density functional theory and cluster expansion methods to predict H_2 permeance through Pd-based binary alloy membranes, Journal of Chemical Physics, 128 (2008) 1-10.

CHAPTER 3

SCREENING METHODOLOGY FOR NON-Pd BASED INTERMETALLICS

A computational methodology for calculation of H permeability through an intermetallic given its crystal structure was developed for the systematic screening of potential membrane materials for hydrogen separation. The details of the calculations performed for computing H permeability are described in Chapter 2. In this chapter, we describe a procedure that was used to select the list of suitable candidates for H separation from the thousands of intermetallics listed in the ICSD [1].

The binary intermetallics that are reported in the ICSD have been classified into two categories: Pd-based intermetallics (where one constituent element is Pd) and non-Pd based intermetallics. In the previous chapter, the two main parameters for screening materials (solubility and diffusion activation barrier) were described. In this chapter, the methods used to perform efficient solubility based screening of the shortlisted materials are discussed in detail.

3.1 ICSD search

A search in the ICSD for binary intermetallics that are a combination of alkali and alkaline earth metals, all d-block metals and Al, Ga, In, Sn, Tl, Pb and Bi from the p-block lists 1625 unique materials.

From these entries, the materials unsuitable for membrane purposes due to factors such as thermal stability, existence as very high or low-pressure phases or lack of experimental evidence (purely computational entries) were removed from further consideration. The various criteria used to remove materials and the number of such entries removed from the list of candidates are listed in Table 3.1. When multiple entries

existed for the same material that listed identical crystal structures and lattice constants, the most recent entry was used for further analysis.

Table 3.1: List of the various conditions used to sort the candidate materials. The number of materials satisfying each condition is listed on the right.

Condition	No.
All ICSD entries	1625
Materials with multiple phases	127
Materials with T_{melt} < 1500 K	104
Materials stable only at high pressures (> 10 atm)	15
Materials stable only above 500 K	89
Purely computational structures	35
Remaining candidates	1255

There are 127 materials that show multiple phases i.e. undergo a phase transition at some temperature from 400-1200 K. For example, the intermetallic NiPt undergoes a change in structure from P4/mmm to Fm-3m at 1000 K. For these materials the individual phases were treated as separate materials at the conditions specified. For example, at temperatures < 1000 K, the calculations to predict solubility of NiPt were performed on its P4/mmm structure, while the Fm-3m structure was used at temperatures > 1000 K. The H solubility of each of the phases of the 127 materials was calculated individually for the relevant temperature ranges. These materials were included in the analysis of potential candidate materials and a total of 1382 materials (1255+127) were screening using the method described below.

Materials that are stable only at high temperatures (> 500 K) or high pressures (> 10 atm) were removed from the list. Many intermetallics had melting points < 1500 K. For

membrane purposes, thermal stability at high temperatures is essential since gas streams containing a mixture of hydrogen and other gases can be produced at 1093 K or higher temperatures [2] . Hence materials with melting points (T_{melt}) lower than 1500 K were removed from the list of potential candidates.

We did not include intermetallic phases whose existence was reported purely computationally. It is possible that other intermetallic structures exist that have not yet been discovered or reported in the ICSD. Their identification however, is beyond the scope of this work.

3.2 Sorting of Candidate Materials according to Space Groups

The 1255 candidate materials (without the multiple phase materials) were sorted according to their space groups. All the materials can be divided into 123 unique space groups. A plot with all the materials sorted by their space groups is shown in Figure 3.1.

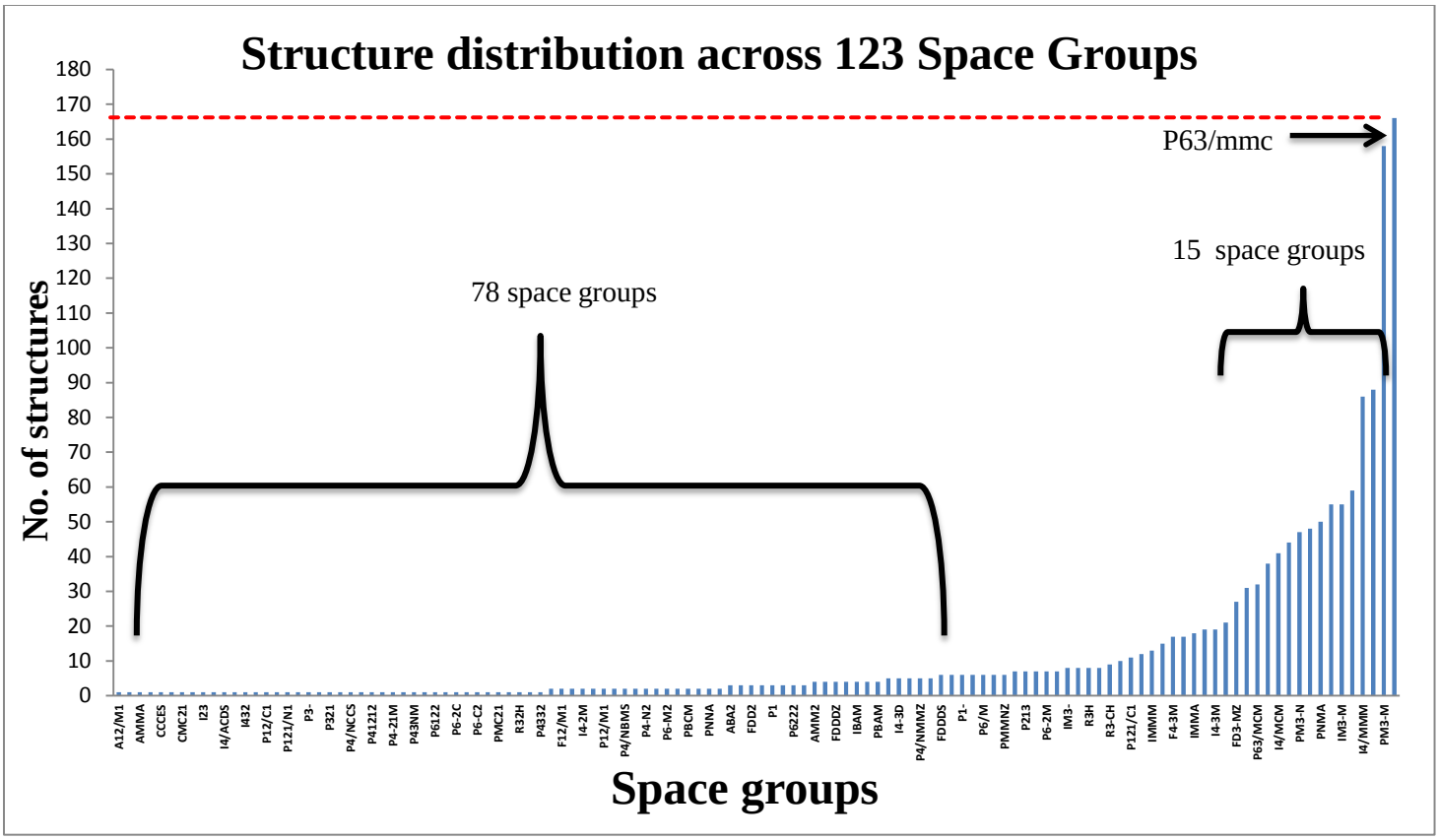

Figure 3.1: 1255 intermetallic materials sorted into 123 space groups. The horizontal axis represents the space groups and the vertical axis is the number of materials in each space group. 78 space groups having 5 materials or less are highlighted. P63/mmc is the space group with the maximum number of materials (166), shown by the red dashed line. The top 15 space groups in the plot are also highlighted.

From Fig. 3.1, we can observe that there are some space groups such as P63/mmc that have a large number of candidate structures (166) and there are 78 space groups that have 5 or less candidate structures. To make the screening process efficient, the space groups were ranked based on the number of candidate structures of each type in the space group and the top 15 were selected for the next steps in the screening process. A substantial proportion of structures (64%) belong to these 15 groups. These 15 space groups include 981 materials that meet the other criteria listed in Table 3.1.

To rapidly identify favorable candidates from the 981 materials in 15 space groups using solubility as a screening parameter and a minimum number of DFT calculations, a

representative structure was chosen randomly from each space group. The top 15 space groups and the representative material chosen for each space group are shown in Table 3.2. The total number of structures that belong to the 15 space groups is 995. This includes 14 materials that show two phases where both phases belong to the 15 space groups. This results in 981 unique materials (removing the double counted materials). In the case of Cu_3Sn, one of the structures belongs to the top 15 space groups (P63/mmc) however the other low temperature structure belongs to F4-3m space group which is not one of the 15 space groups. Similarly HfV_2 has two other low temperature phases (Fd-3mz and Imma) apart from Fd-3ms which are not included in these 15 space groups. NiTi shows three other structures apart from its Pm-3m structure i.e. P-, P121/m1 and P1121/m. For these three materials the 6 structures that do not belong to the 15 most populated space groups were also considered and the calculations were performed separately for the relevant temperatures. In total, in this work, calculations were performed on 1001 (995+6) structures.

During the solubility calculation using the methods described in Chapter 2, unique H binding sites in each material are identified. We simplified our analysis by assuming that the geometry of these unique binding sites is common between crystal structures within the same space group. This assumption is consistent with data from previous calculations for different Fm-3m (fcc) structures that resulted in consistent geometric locations of the H-binding sites [3, 4]. Although the locations of binding sites are the same in similar materials, the binding energy of H in each material depends on the material's constituent elements.

Table 3.2: The top 15 most common space groups along with the number of structures of each space group type are shown. The prototype column lists the composition of the intermetallic selected as the representative structure of the space group.

S.No	SG	No. of structures	Representative Structure
1	P63/mmc	166	Fe_2Nb_1
2	Pm-3m	158	Co_1Ti_1
3	Fm-3m	88	Ir_1Sn_2
4	I4/mcm	86	Ba_5Pb_3
5	Fd-3ms	57	Be_2Cu_1
6	Cmcm	55	Bi_2Ca_1
7	Im-3m	55	Nb_1Hf_1
8	Pnma	50	Au_1Y_2
9	P6/mmm	47	Fe_5Y_1
10	Pm-3n	47	Au_1Zn_3
11	R-3mh	44	Ir_3Y_1
12	I4/mmm	41	Au_2Hf_1
13	P4/mmm	38	Cd_3Zr_1
14	P63/mcm	32	Hf_5Ir_3
15	P42/mnm	31	Cr_2Ru_1

If the locations of H binding sites inside the material are known *a priori*, the number of calculations involved in computing the solubility of H in each materials decreases significantly. This is because the methods used in our earlier work to identify potential H binding sites results in the generation of hundreds of candidate binding sites. The identification of actual binding sites from this list involves hundreds of DFT calculations for each material. Adopting the H binding site positions obtained from one structure across crystal structures within a space group makes this screening process on an average more than 20 times faster in comparison to detailed calculation for every

material. It is important to note that the structure of each binding site is still fully optimized using DFT in our calculations. The efficiency in the approach just described lies in the reduction of the number of these DFT calculations that must be performed.

To calculate the binding energies of H in all 1001 structures, a python library called Pymatgen that enables easy manipulation of VASP input and output files and materials analysis was used[5, 6]. In addition to the various tools already available within the Pymatgen library, several modifications and new applications developed in Python and Shell helped in automating the process and minimizing human input in calculation of the solubility of these materials. This resulted in increased efficiency and speed of the DFT calculations.

The PW91 generalized gradient approximation functional using the projector augmented wave method was used for all calculations with crystal structures and lattice parameters obtained from ICSD using the Vienna *ab initio* simulation package (VASP) [7-14]. A cut-off energy value of 250 eV was used and geometries were relaxed using a conjugate gradient method until the forces on all atoms were less than 0.03 eV/Å. The geometric relaxation to obtain the lattice parameters was performed using a dense k-point mesh to sample the reciprocal space and relaxing the lattice constants and all internal coordinates.

Once the solubility of H in each of these materials is calculated, the same screening criteria described in Chapter 2 were used to select favorable candidates i.e. a solubility range of (10^{-1}-10^{-5} H/M). Materials with solubility lower than 10^{-5} H/M were removed from further consideration. Materials with H binding energies more favorable than -0.3 eV result in H loadings that cannot be calculated using Sieverts' Law (dilute loading) and were also eliminated from the list of potential membrane materials.

The next steps in H permeability calculation as described in the previous chapter are activation barrier estimation and diffusivity calculations for the selected candidates. The same procedure described earlier was used in final permeability calculation of the

favorable candidates selected after screening [4]. Pure Pd was used as a benchmark for this study to compare permeabilities of the selected candidate materials. The results of the screening of Pd-based intermetallics are in Chapter 4 and non-Pd based intermetallics are described in Chapter 5.

3.3 References

[1] G. Bergerhoff, I.D. Brown, Crystallographic Databases, International Union of Crystallography, Chester, 1987.

[2] N.W. Ockwig, T.M. Nenoff, Membranes for Hydrogen Separation, Chemical Reviews, 107 (2007) 4078-4110.

[3] S.G. Kang, K.E. Coulter, S.K. Gade, J.D. Way, D.S. Sholl, Identifying Metal Alloys with High Hydrogen Permeability Using High Throughput Theory and Experimental Testing, The Journal of Physical Chemistry Letters, 2 (2011) 3040-3044.

[4] N. Chandrasekhar, D.S. Sholl, Quantitative Computational Screening of Pd-based Intermetallic Membranes for Hydrogen Separation, Journal of Membrane Science 453, 516 (2014).

[5] S.P. Ong, W.D. Richards, A. Jain, G. Hautier, M. Kocher, S. Cholia, D. Gunter, V.L. Chevrier, K.A. Persson, G. Ceder, Python Materials Genomics (pymatgen): A robust, open-source python library for materials analysis, Comput. Mater. Sci., 68 (2013) 314-319.

[6] A. Jain, G. Hautier, C.J. Moore, S. Ping Ong, C.C. Fischer, T. Mueller, K.A. Persson, G. Ceder, A high-throughput infrastructure for density functional theory calculations, Comput. Mater. Sci., 50 (2011) 2295-2310.

[7] G. Kresse, J. Hafner, Ab initio molecular dynamics for liquid metals, Physical Review B, 47 (1993) 558-561.

[8] G. Kresse, J. Hafner, Ab initio molecular-dynamics simulation of the liquid-metal–amorphous-semiconductor transition in germanium, Physical Review B, 49 (1994) 14251-14269.

[9] G. Kresse, J. Furthmüller, Efficiency of ab-initio total energy calculations for metals and semiconductors using a plane-wave basis set, Comput. Mater. Sci., 6 (1996) 15-50.

[10] G. Kresse, J. Furthmüller, Efficient iterative schemes for ab initio total-energy calculations using a plane-wave basis set, Physical Review B, 54 (1996) 11169-11186.

[11] G. Kresse, D. Joubert, From ultrasoft pseudopotentials to the projector augmented-wave method, Physical Review B, 59 (1999) 1758-1775.

[12] P.E. Blöchl, Projector augmented-wave method, Physical Review B, 50 (1994) 17953-17979.

[13] J.P. Perdew, J.A. Chevary, S.H. Vosko, K.A. Jackson, M.R. Pederson, D.J. Singh, C. Fiolhais, Atoms, molecules, solids, and surfaces: Applications of the generalized gradient approximation for exchange and correlation, Physical Review B, 46 (1992) 6671-6687.

[14] J.P. Perdew, J.A. Chevary, S.H. Vosko, K.A. Jackson, M.R. Pederson, D.J. Singh, C. Fiolhais, Erratum: Atoms, molecules, solids, and surfaces: Applications of the generalized gradient approximation for exchange and correlation, Physical Review B, 48 (1993) 4978-4978.

CHAPTER 4

RESULTS FOR Pd-BASED INTERMETALLICS

We performed calculations for binary intermetallics containing Pd. The motivation for this choice was that Pd shows excellent hydrogen permeability and intermetallics are appealing if high permeability intermetallics were identified. The ICSD [1] reports 135 binary intermetallics of Pd, including some with the d-block metals Ga, Bi, In, Tl, Sn and Pb and the f-block metals. We did not perform calculations for intermetallics of the f-block elements because DFT calculations with the lanthanides and actinides have complications that have been extensively reviewed [2, 3]. We therefore considered the 88 Pd-based intermetallics with the d-block and the p-block metals. 88 such binary intermetallics were studied, out of which the ICSD structure for 10 of these materials did not match the nominal stoichiometry. There was incomplete information on 6 of the structures and in the case of $Pd_{41}Nb_9$, Pd_5In_3, $Pd_{13}Tl_{19}$ and Pd_3Zn_{10} the given structure was found to be highly unstable. As a result, calculations for H in 78 Pd-containing binary intermetallics were completed.

For one material, Pd_3Mn, calculations were used to assess a number of potential metastable crystal structures. For these structures, a cut off energy of 250 eV was used with a 10×10 ×10 k-point mesh. DDEC [4, 5] and Bader [6] charge analysis was performed to study the charges on the atoms in the most favorable binding site configuration.

4.1 Pd-based binary intermetallics

To establish if DFT gives accurate information about the structure of materials, the lattice parameters of the materials listed in ICSD were compared with the DFT derived lattice parameters, taking the most recent entries for the respective materials in ICSD as the starting point of our calculations. The optimized and experimental lattice parameters

are listed in Appendix A. The exchange-correlation functional PW91 tends to overestimate lattice constants [7]. The discrepancy between calculated and experimental lattice constants is more pronounced in 5-d transition metals [8].

The calculated lattice constants of the two intermetallics of 5-d elements, Hg and Hf, show significant deviation from ICSD reported values. The poor crystalline nature of PdHg results in a lower experimentally measured density than would be expected from the crystal structure [9]. There were differences between lattice parameters of naturally obtained and synthetically manufactured samples of PdHg, leading to unknown errors in reported lattice constants. The lattice parameters used for comparison in this work are the most recently reported values [8]. For Pd_5Hf, the lattice constants calculated in this study are very different from the ICSD values. The lattice constants for Pd_5Hf listed in the ICSD are theoretical calculations [10]; no experimental values are available. To verify the Pd_5Hf lattice constants calculated in this study, static DFT calculations (with no geometric relaxation) at different lattice parameters were performed. The lattice parameters obtained for the most stable structure from the static calculations matched those predicted with the methods used above. This suggests that these results are more reliable than the earlier theoretical results listed in the ICSD. The solubility of this material was calculated with the lattice constants obtained in this study. Apart from the two materials discussed above, the calculated and reported values are in good agreement with each other, as expected [11, 12]. The DFT optimized structures were used for further calculations.

The hydrogen solubility of 78 Pd-based binary intermetallics was studied and computed using the methods described in Chapter 2. Figure 4.1 shows the solubility of the intermetallics measured in hydrogen per metal atom (H/M) plotted against the volume per metal atom. The inset shows an expanded view of the solubility for volumes between 12 and 18 $Å^3$. The favorable range of solubility is bound by the solubility of

pure Pd (10^{-1} H/M) as the upper limit and 10^{-5} H/M as the lower limit. The black solid line (pure Pd) and the red dashed line (lower limit) in the inset show this solubility range that was used to screen candidates (10^{-1}-10^{-5} H/M). This range was chosen to accommodate the possibility of a material having lower solubility and higher diffusivity compared to pure Pd resulting in higher permeability.

The results indicate that among this diverse set of intermetallics, H solubility is not correlated with atomic volume. For example, the unit cell volume of PdFe, PdMo, PdIn, Pd_3Pb, PdAg and PdSc is ~ 20 $Å^3$/ metal atom but their solubilities vary by a factor of 10^7. Previous studies of H solubility in substitutionally-disordered Pd alloys with the fcc crystal structure indicate that increasing atomic volume correlates with enhanced solubility, although atomic volume cannot account for all of the variation that exists among these alloys[13, 14]. Our results imply that chemical interactions between the atoms of the intermetallic and H and the diverse crystal structures of the intermetallics play a critical role in the solubility of H.

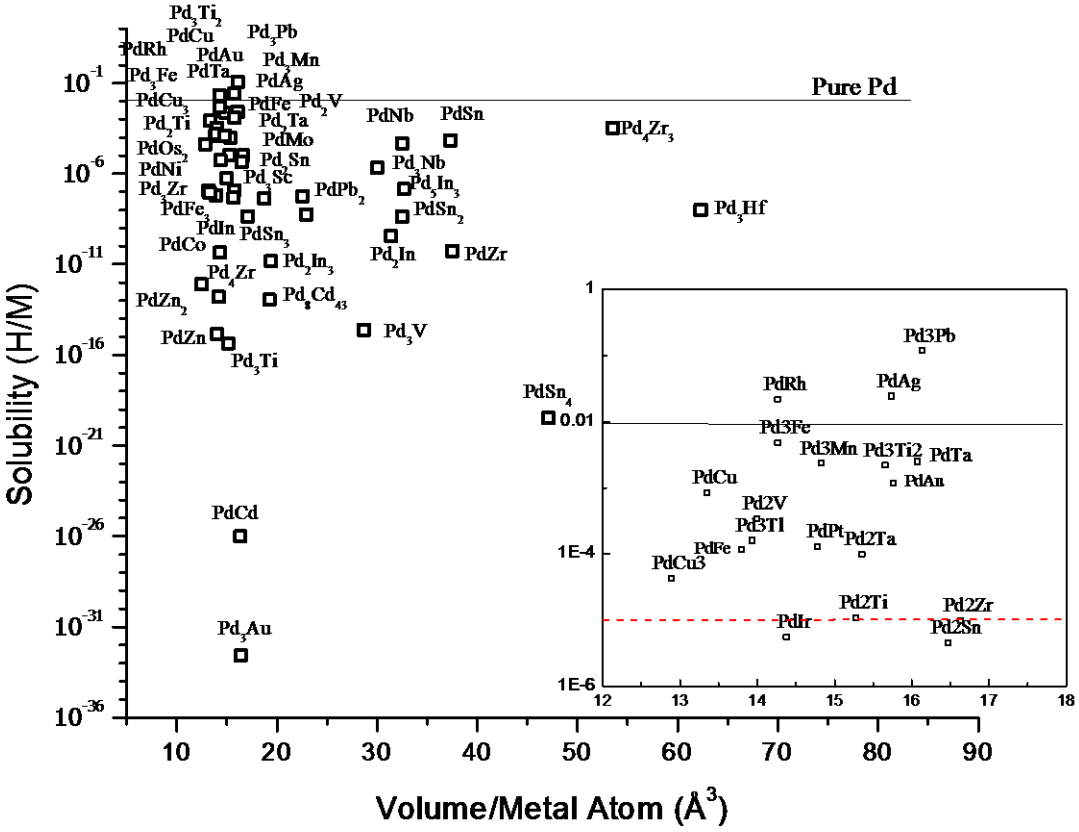

Figure 4.1: Solubility (H/M) of hydrogen at 600 K in 57 intermetallics. Each data point is labeled by the respective intermetallic. The solubility (H/M) for pure Pd computed with the same methods is shown as a horizontal line for comparison. The volume/metal atom for pure Pd is 15.9 Å^3. The inset shows an expanded view of the solubility for volumes between 12 and 18 Å^3. The black solid line and the red dashed line in the inset show the favorable solubility range used to screen candidates (10^{-1}-10^{-5} H/M).

Figure 4.1 illustrates examples where two intermetallics such as Pd_2Zr and $PdZr_2$, having same constituent elements, show very different properties. Pd_2Zr has limited solubility compared to $PdZr_2$, which shows hydride forming tendencies (high solubility). This observation has been reported earlier and d-band effects have been used to explain their different behavior [15].

Table 4.1 lists the Pd-binary intermetallics that have binding energies < -0.3 eV. Materials with interstitial site binding energies < -0.3 eV bind H very favorably. These materials have a tendency to form hydrides, thus altering the structure, composition and properties of the membrane. The current method in this study cannot be reliably extended to solubility calculations of these materials (binding energies <-0.3eV) due to the assumption of dilute loading. Therefore, the solubility of these materials was not calculated (Figure 4.1).

Table 4.1: List of intermetallic compounds and the energy of the most favorable H binding site. The solubility for these materials cannot be reliably calculated using Sieverts' law. These materials are not favorable for use as membranes.

Material composition	E_b (eV)	Material composition	E_b (eV)
Pd_3Y	-0.32	Mn_3Pd_5	-0.36
Pd_5Ti_3	-1.21	PdV_3	-0.54
PdTi	-1.22	$PdNb_3$	-0.72
PdSc	-0.37	Pd_3In	-0.44
PdMn	-0.64	Pd_5Hf	-0.48
$PdHf_2$	-2.70	Pd_2Ga	-0.40
Pd_3Cd	-0.28	Pd_3Sn	-0.29
$PdTi_2$	-0.81	Pd_5Ga_2	-0.56
$PdZr_2$	-0.58	Pd_3Ta	-0.21
Pd_7Ga_3	-0.76	Pd_2Hg_5	-1.20
$PdCu_4$	-0.26		

One of the assumptions we made in calculating hydrogen solubility was that interstitial H does not significantly alter the unit cell volume. Calculations were performed for selected materials in Table 4.1 where the unit cell volume was relaxed in the presence of hydrogen to determine if the lattice undergoes significant changes. Five materials with the most favorable H binding energies from Table 4.1 were chosen for this purpose. Table 4.2 lists the volume of the unit cell calculated at dilute loading of hydrogen with lattice relaxation. The volume increase ranged from -0.5 to 1.4% of the

volume of the original structure. These lattice expansions are small, indicating that our predictions for the binding energy of hydrogen using calculations that neglect lattice expansion are accurate.

Hydride formation is an undesirable property in membrane materials. Therefore, materials with hydride forming tendencies (E_b<-0.3 eV) have been removed from further consideration. Hydride forming materials typically have H binding energies in this range [16]. A majority of the non-Pd elements in Table 4.2 are known to form stable hydrides, so the possibility of hydride formation in their intermetallic phases is not unexpected [17]. It is useful to note, however, that the presence of a hydride-favorable element does not necessarily imply that hydride formation will be observed in an intermetallic. An example of this concept is Pd_3Ti_2. TiH_2 is a very stable hydride, but Pd_3Ti_2 is predicted by our calculations to have H solubility in the favorable range (10^{-1}-10^{-5} H/M) for membrane application [18].

Table 4.2: Effect of hydrogen on the volume of the unit cell of the intermetallic structures. The first column lists the name of the intermetallic; the second column lists the volumes of the intermetallic after volumetric expansion of the lattice in the presence of hydrogen. The volume of the pure unit cell is listed in column 3. The last column shows the percentage increase in the volume due to H relative to the volume of the pure material.

Intermetallic	Relaxed Volume (H induced) Å^3	Pure Volume Å^3	H induced volume change %
Pd_5Ti_3	1132.83	1129.91	0.23
$PdNb_3$	611.82	603.92	1.31
$PdTi_2$	779.49	768.21	1.47
PdTi	846.98	851.97	-0.59
Pd_7Ga_3	302.98	300.10	0.96

Diffusion calculations were performed for the materials having favorable H/M ratio (10^{-1}-10^{-5} at 600 K, 1 atm H_2) using the methods described in Chapter 2. Figure 4.2 illustrates the activation barriers calculated for these materials as a function of the volume per unit cell of the material. All materials were found to have activation barriers

higher than pure Pd except PdCu. The activation barriers of Pd_3Pb was found to be 0.95 eV .This barrier is very high compared to pure Pd, which would lead to very low diffusivity values. Hence, KMC calculations were not performed to compute diffusivity for this material.

The diffusivity of shortlisted materials (other than PdCu) was lower than pure Pd, as observed in Figure 4.3. Similar trends have been observed in previous studies [14, 19], where a higher activation barrier led to lower diffusivity. PdCu has a higher diffusivity than pure Pd. PdCu is a body-centered-cubic structure (bcc), which is known to have higher diffusivity of hydrogen than face-centered-cubic (fcc) structure [20]. No other material in Fig. 4.2 has a bcc structure.

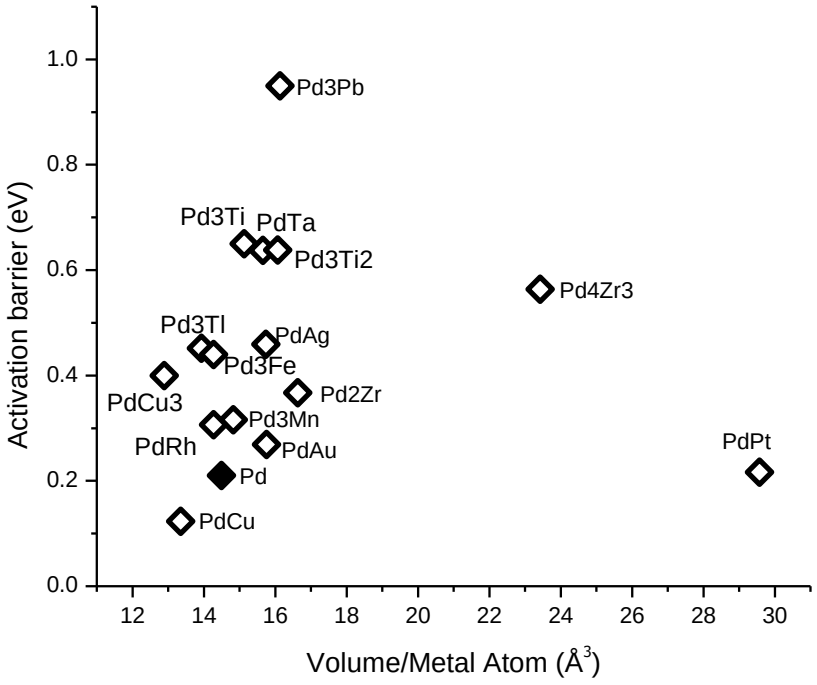

Figure 4.2: The activation barrier for H diffusion estimated from the difference in energy between the transition state and the binding site. The activation energy for pure Pd is highlighted by the filled symbol.

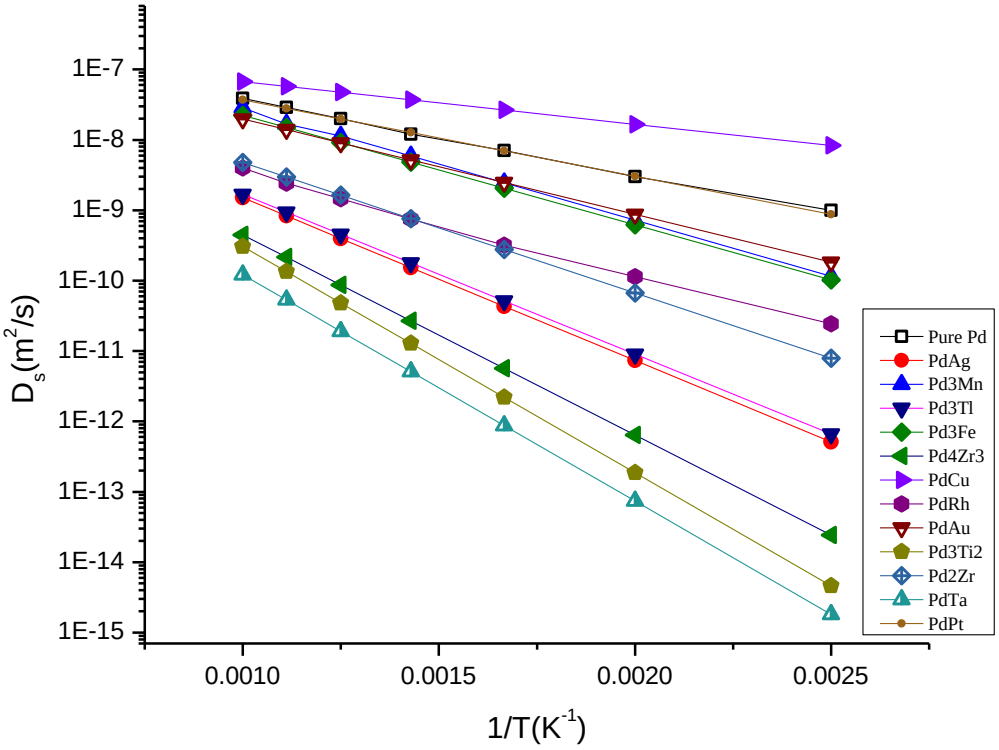

Figure 4.3: Diffusivity of selected intermetallics chosen on the basis of their solubility and activation barrier predicted by DFT based methods. Open squares show the result for pure Pd.

The permeability of H_2 through an intermetallic can be calculated using the solubility and diffusivity of H as defined in equation 3 in Chapter 2. The predicted permeabilities of the shortlisted intermetallics are shown in Figure 4.4 as a function of temperature at a pressure of 1 atm H_2. PdRh, PdCu and Pd_3Mn were found to have permeabilities one order of magnitude lower than pure Pd. The solubility of PdRh is higher than pure Pd. However, PdRh has an activation barrier of 0.306 eV, which is higher than that of pure Pd, resulting in a lower diffusivity and permeability. A similar decrease in diffusivity has been previously observed for disordered Pd-Rh alloys with compositions different from the PdRh intermetallic [21]. The activation barrier of Pd_3Mn (0.28 eV) is higher than that of pure Pd (0.21 eV) but has comparable solubility

(Figure 4.1 inset).This difference in diffusivity results in an order of magnitude decrease in the H permeability of Pd_3Mn compared to pure Pd. $PdCu_3$ was found to have a lower permeability than PdCu by two orders of magnitude. A similar observation was made previously in the case of disordered Pd-Cu alloys where increasing the alloy percentage of Cu resulted in a lower diffusivity and permeability [22]. Thus, increasing the percentage of Cu has similar effects on both Pd-Cu intermetallics and alloys. PdCu has lower permeability than pure Pd despite having a higher diffusivity since the solubility of PdCu is significantly lower than pure Pd. The main conclusion from these calculations is that after systematically examining all Pd-based intermetallics, no material was found to have higher hydrogen permeability than pure Pd.

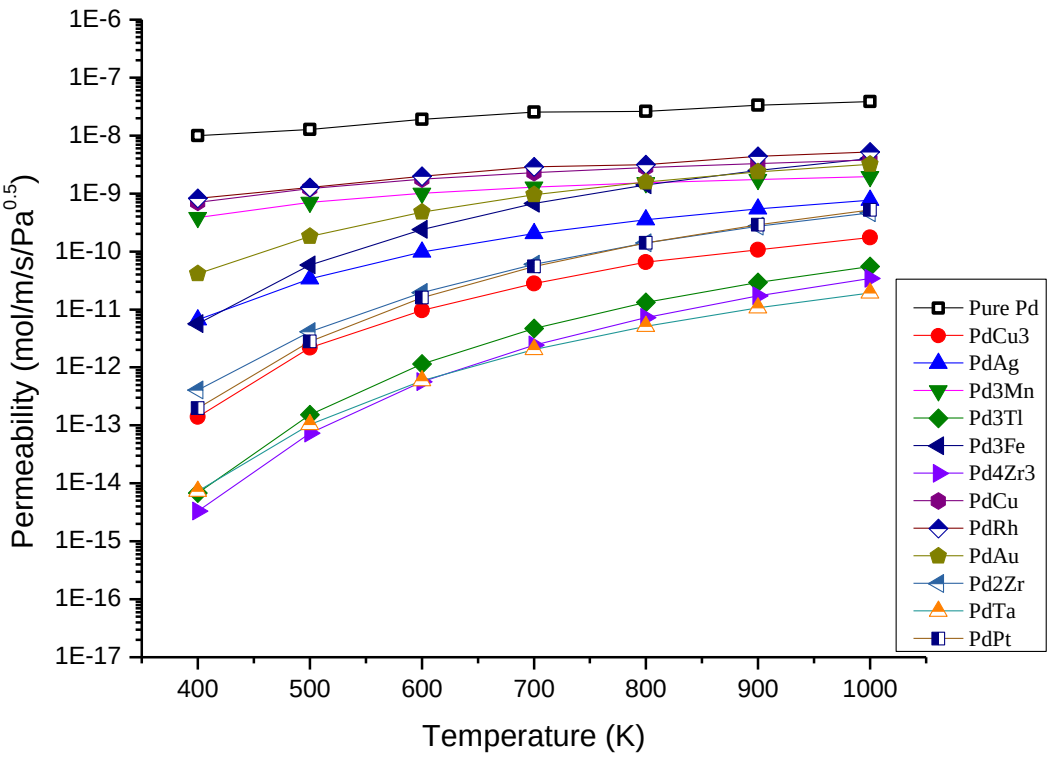

Figure 4.4: Permeability of selected intermetallics chosen based on their solubility and activation barrier predicted by the DFT based methods. Open squares show the result for pure Pd.

4.2 Metastable structures of Pd_3Mn

At a given stoichiometry, multiple different intermetallic crystal structures can exist. The most stable structure at a given stoichiometry is the ground state structure and it is this structure that will be observed experimentally at equilibrium. The structures that are less favorable than the ground state structures are called metastable structures. The relative stability of metastable structure can be described using convex hull diagrams [10, 11, 23]. All of the calculations above correspond to hydrogen solubility and diffusion in the ground state crystal structures of intermetallics. The calculations done in this work to determine the ground state structures do not include spin-orbit coupling effects. Spin-orbit interactions affect the energies of specific structures especially those involving heavy elements (4-d and 5-d elements). However, previous studies have shown that including these relativistic effects for transition metals does alter the total energies but does not change the relative stability of the different phases [10, 24]. Hence the structures predicted to be the ground states in this paper will not be qualitatively affected by the inclusion of these effects. It is conceivable, however, that the presence of interstitial hydrogen could alter the relative stability of metastable intermetallics. To investigate the potential influence of hydrogen on the stability of metastable phases, we examined a number of metastable structures of Pd_3Mn. Pd_3Mn was chosen since its binding energy, diffusion barrier and structure is similar to pure Pd.

A computationally-determined binary phase diagram that predicts the ground state structures of Pd-Mn by Curtarolo et al. showed a stable structure at a composition of Pd-75% Mn-25% [11]. These DFT calculations also identified multiple metastable structures at this composition. We chose 7 metastable Pd_3Mn structures close in energy to the ground state structure were selected. The enthalpy of formation at 0 K for each of

these structures was calculated using the DFT parameters described in the Chapter 2. These values are listed in in Table 4.3. Pd_3Mn in the $AuCu_3$ prototype with space group 221 (designated below as $AuCu_3$ (221)) was predicted to be the most stable. This is in agreement with the experimental structure that was the basis of our calculations in the previous section. The order of stability of the metastable structures predicted in our calculations relative to the ground state at 0 K differ from those earlier reported due to the differences in DFT parameters (e.g., k-points and cutoff energy)[11]. In the case of metastable Pd_3Mn in the Ni_3Ti (194) structure, the input structure for the geometric relaxation is a hexagonal cell with lattice parameter of 5.096 Å and c/a = 1.629. This structure transformed to a base centered orthorhombic cell with a lattice parameter of 5.414 Å, b/a=1.732 and c/a =1.631 after relaxation. This transformation in structure upon geometric relaxation is responsible for the large difference in the enthalpy values compared to those reported by Curtarolo et al [11].

The hydrogen binding energies in the interstitial sites in each of the 8 structures of Pd_3Mn (7 metastable and 1 ground state) were calculated using the procedure described in the beginning of this chapter. Using the binding energies, the net Sieverts' constant for each structure was determined [20]. At a pressure of 1 atm H_2 and 600 K, all structures except the Mo_3Ti (139) and the orthorhombic relaxed phase of Ni_3Ti (194) were found to have a Sieverts' constant lower than the ground state structure. At a pressure of 1 atm H_2 and 600 K, the hydrogen loading (H/M) in the Mo_3Ti (139) and the Ni_3Ti (194) phase was higher than the dilute loading limit of 0.1 H/M and thus out of the region where Sieverts' law is applicable. To compare H/M of all materials in the dilute limit, the total hydrogen pressure was reduced to a very low value, 10^{-12} atm, since

$$\frac{H}{M} = K_s \times \sqrt{P_{H_2}} \tag{4}$$

where, K_s is the Sieverts' constant and P_{H2} is the hydrogen pressure.

Table 4.3: The predicted properties of different Pd_3Mn metastable phases. The first column lists the Pd_3Mn structure prototype (space group). The second column lists the calculated enthalpy of formation at 0 K (ΔH) and the third column contains the volume per metal atom of each phase. The fourth column shows the Sieverts' constants ($atm^{-0.5}$) calculated at 1 atm P of H_2. The osmotic potential relative to $AuCu_3$ (221) is listed in the fifth column. The osmotic potential of the different structures was calculated at 10^{-12} atm P of H_2.

Structure	ΔH (eV/atom)	V/metal atom $Å^3$/atom	K_s (1 atm H_2, 600K)	$\Delta(\Omega_{T,p})$ J/metal atom
$AuCu_3$(221)	-0.175	15.2	0.0132	0
Cd_3Y(63)	-0.173	14.9	7.78E-07	1.36E-04
Al_3Zr(139)	-0.168	15.2	7.28E-03	6.11E-05
$NbPd_3$(59)	-0.152	14.9	4.08E-05	1.36E-04
Al_3Tl(139)	-0.143	15.3	5.42E-03	8.03E-05
Mo_3Ti(139)	-0.0971	15.1	22.3	-0.231
Ni_3Sn(194)	-0.0779	17.1	7.70E-03	5.67E-05
Ni_3Ti(194)	0.257	16.6	2.00E+04	-206.95

The aim of our calculations was to explore whether exposure to hydrogen can stabilize a metastable phase of an intermetallic. To determine the stability, the osmotic potential of the metastable phase after hydrogen absorption was calculated. The osmotic potential characterizes the free energy of a solid after the adsorption or absorption of another species [25, 26]. The different Sieverts' constant of the materials causes varied amounts of hydrogen to be absorbed [27]. To compare the relative stability of each of the Pd_3Mn structures after hydrogen absorption, the difference in osmotic potential of each structure relative to the ground state structure was calculated. For intermetallics with the same stoichiometry

$$\Delta(\Omega_{T,P}) = E_1 - E_2 + P(V_2 - V_1) - 2RT\sqrt{P_{H_2}}(K_{s_1} - K_{s_2}) \quad (5)$$

where E_1 and E_2 are the DFT calculated enthalpies of formation at 0 K, P is the hydrogen pressure, V_2 and V_1 are the volumes of the unit cells of the structures and K_{s_1} and K_{s_2} are the Sievert's constants of the structures being compared.

The difference in osmotic potential values of the 7 structures relative to the ground state is listed in Table 4.3. The ground state structure $AuCu_3$ (221) is used as a reference and hence has $\Delta(\Omega_{T,P}) = 0$. The Mo_3Ti (139) and Ni_3Ti (194) structures have lower osmotic potential than the ground state structure by 0.23 J/metal atom and 206.95 J/metal atom respectively. The highest H_2 pressure that can be considered for the hydrogen solubility in Ni_3Ti (194) structure while remaining in the Sieverts' region is only 2.5×10^{-11} atm. Hydrogen alters the relative stability of these metastable states by stabilizing the Mo_3Ti (139) and Ni_3Ti (194) structures preferentially relative to the H-free ground state structure.

To study the variation in the hydrogen binding energy in the different structures, the most favorable interstitial site in three structures (the ground state, Mo_3Ti (139) and Ni_3Ti (194)) was examined in greater detail. The coordination number of the most stable interstitial site and the distance of hydrogen from the nearest neighbors were calculated for each of the three structures. The results are listed in Table 4.4. The distances between the hydrogen and the metal atoms are similar in the three cases. This indicates that geometrical factors such as distance between hydrogen and the metal atom in the interstitial site are not a useful descriptor to the binding energy of hydrogen in the material.

Table 4.4: Properties of the most favorable binding site in the two metastable structures of Pd_3Mn Mo_3Ti (139) and Ni_3Ti (194) in comparison to the ground state $AuCu_3$ (221). The distance of H from each of the neighbor atoms is listed under distance.

Properties	**$AuCu_3$(221)**	**Mo_3Ti(139)**	**Ni_3Ti(194)**
Most favorable binding energy (eV)	-0.14	-0.51	-0.85
Type of site	6-coordinated	6 coordinated	4 coordinated
Type of atoms	6 Pd	5 Pd 1 Mn	4 Pd
Distance (Å)	**$AuCu_3$(221)**	**Mo_3Ti(139)**	**Ni_3Ti(194)**
Pd_1-H	2.02	1.879	1.904
Pd_2-H	1.987	2.09	1.888
Pd_3-H	2.002	1.973	2.057
Pd_4-H	1.971	1.939	2.076
Pd_5-H	1.95	1.934	--
Pd_6-H	1.982	--	--
Mn-H	--	2.189	--

To explore the difference in binding energy of H in the three phases further, DDEC and Bader charge analysis was performed. These methods are two possible ways of assigning point charges to nuclei based on the full electron distribution in a quantum chemistry calculation [4, 5, 28, 29]. The results are shown in Table 4.5. The charge calculated for Pd in the three cases is the average of the charge observed on the Pd atoms directly interacting with the interstitial hydrogen i.e. the Pd atoms in the coordination sphere. The Mn charge in the case of Mo_3Ti (139), where the most favorable H interstitial site directly interacts with one Mn atom in the coordination sphere, the charge in the table is the charge of the Mn atom. In the other two cases where the H coordination sphere does not have Mn atoms, the charge reported is the average of the charge on the Mn atoms closest to the hydrogen atom (next nearest neighbors).

The DDEC and Bader charge analysis give different values of the charges on the elements. These differences can be attributed to the different methods used to calculate them [4, 5, 28]. The goal of this analysis is to compare the charges on the Pd and Mn atoms in the three structures using a particular method. However, the charges predicted by either method for Pd and Mn atoms in the three structures do not show a trend

correlating in a simple way to the binding energy of H in the material. For example, using the DDEC method, the difference in charge on the Mn atom in $AuCu_3$ (221), Mo_3Ti (139) and Ni_3Ti (194) structures is -0.794, -0.749 and -1.069. While the charge on the Mn atom in Ni_3Ti (194) is more negative, the charge on Mn atom in Mo_3Ti (139) and $AuCu_3$ (221) is similar despite the large difference in H binding energy. Similarly in the case of Bader analysis, the charges on the atoms (Pd, Mn) in $AuCu_3$ (221) and Ni_3Ti (194) are similar but there is a significant difference in H binding energies in the two phases. Hence, we conclude that the charge analysis fails to predict any trend in the H binding energies in the three phases. This suggests that electrostatics is not a dominant driving force in the solubility of hydrogen in the interstitial sites in these materials.

Table 4.5: Charge calculation of each metastable configuration found to have more favorable H binding energy than the ground state, using bader and DDEC analysis.

Method	Element	$AuCu_3$(221)	Mo_3Ti(139)	Ni_3Ti(194)
Bader charge	Pd	0.246	0.273	0.453
	Mn	-0.749	-0.794	-1.069
	H	0.080	0.130	0.202
DDEC charge	Pd	-0.180	-0.292	-0.193
	Mn	0.112	0.265	0.120
	H	0.020	-0.042	-0.054

The permeability of H_2 in Ni_3Ti (194) was calculated using the method described above. The activation barrier was found to be 3.5 eV. This barrier is extremely high and can be explained by the high binding energy of H_2 in this material (-0.85 eV). The H_2 is bound very favorably in the interstitial site, resulting in the decrease in the diffusivity leading to very low permeability. Figure 4.5 shows the effect of structure on the permeability of Pd_3Mn at a H_2 pressure of 10^{-12} atm. We emphasize that this low pressure was chosen solely to make it possible to consider both materials within their Sieverts' law regime. Perhaps the most important outcome of these calculations is that H-induced stabilization of metastable intermetallic phases is possible. This observation implies that phases of this kind should be carefully considered after potentially

promising intermetallics have been identified in screening calculations such as those we described above.

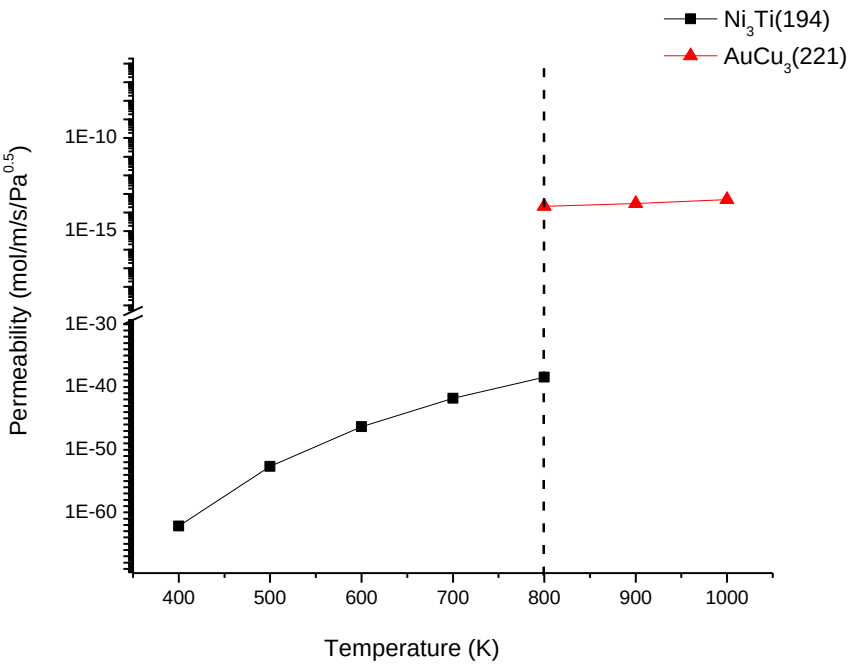

Figure 4.5: Effect of structure on permeability of hydrogen through Pd_3Mn. $AuCu_3$(221) is the ground state structure and Ni_3Ti(194) is a metastable structure of Pd_3Mn. Ni_3Ti(194) is more stable in the presence of hydrogen than the ground state structure at a temperature up to 800 K at a H_2 pressure of 10^{-12} atm.

4.3 QSPR Modeling

In this work, solubility was used as a screening parameter to shortlist probable candidate materials for hydrogen separation. The solubility was calculated using quantum chemistry methods that are computationally demanding. If the solubility could be calculated using a simple empirical expression instead of DFT calculations, the computational time would be negligible. This would help in large scale screening of materials using solubility as a screening parameter. Quantitative Structure Property Relationship (QSPR) is a systematic analysis where an expression to predict a property is generated using regression, from various descriptor variables. QSPR has been used

extensively in drug discovery and activity prediction of various biomolecules[30]. This methodology was used to seek an empirical expression for the ensemble average binding energy that predicts the solubility of the intermetallics. The ensemble average binding energy is defined as

$$E_{ens} = \sum_{i=1}^{n} \frac{E_i e^{\frac{-E_i}{kT}}}{e^{\frac{-E_i}{kT}}} \quad (6)$$

where E_i is the energy of binding site i and n is the total number of binding sites per unit cell of the material. This ensemble average is a useful description of the effective binding energy of the H in the material.

The descriptors we used to generate an expression for the ensemble average binding energy using QSPR are elemental properties that are expected to influence the solubility of hydrogen in the intermetallic but at the same time are simple to calculate. The descriptors chosen were the heat of hydride formation predicted by Griessen's model [31], the difference in electronegativity of the elements weighted according to their stoichiometry, volume per metal atom, weighted work function of the intermetallic and weighted elemental binding energy of the elements constituting the intermetallic [32]. The descriptors were weighted according to the stoichiometry of the compound. These different parameters were calculated for each of the intermetallics studied in this work.

75 out of the 78 intermetallics were used as the test set for generating the regression model. Three randomly chosen materials, Pd_3V, Pd_3Y and PdRh, were intentionally left out to be used as test cases for checking the performance of the predicted model. Different combinations of the descriptor variables were considered. Different non-linear regression expressions (up to third order terms) for prediction of ensemble average binding energy were generated by systematically increasing the number of X variables using different combinations of them. The expressions considered in this work are listed in Appendix A.

The highest R^2 value obtained among all the empirical expressions we tested was 0.58. The expression with this R^2 value (Appendix A) had 15 terms obtained from various combinations of the descriptors. The low R^2 value of this model indicates that the expression generated by QSPR cannot accurately calculate the ensemble average binding energies. Therefore, the comparison between the QSPR predicted binding energies and DFT predicted values of the three intermetallics (test cases) was not made. This is the first time that QSPR model has been used to predict the binding energy of H_2 in an intermetallic material. Although this model was unsuccessful, QSPR methodology could be further explored to develop expressions to rapidly predict properties that are computationally demanding.

4.4 Conclusion

In summary, we have used DFT-based methods to systematically examine hydrogen permeation through 78 Pd-based binary intermetallics. These calculations required no other input apart from the structure of the materials and are far more efficient than attempting to characterize the same set of materials experimentally. This work considerably extends the set of materials for which hydrogen permeability is known. We have compared our results with information available from literature about the behavior of a few intermetallics towards hydrogen and our results show agreement with previously reported data.

Solubility was shown to be an effective screening parameter for finding materials for hydrogen separation. The set of materials for which diffusivity calculations were performed were substantially reduced based on the solubility. Thus, using solubility of H as a screening parameter narrowed the list of probable candidate materials that were good for membrane applications, making the screening process efficient.

During the analysis of Pd_3Mn, we also examined the hydrogen solubility of metastable states and found that at low hydrogen pressures, there are metastable phases that are stabilized by hydrogen. This expands the set of possible membrane materials to include those having properties similar to Pd_3Mn. This implies that the search for favorable membrane materials for H separation should not be restricted to the ground state structures of the materials alone but should also include their metastable structures.

A QSPR model was also constructed to develop an empirical expression to estimate ensemble average binding energies for solubility calculation from various descriptors but the model could not predict the binding energies accurately.

4.5 References

[1] G. Bergerhoff, I.D. Brown, Crystallographic Databases, International Union of Crystallography, Chester, 1987.

[2] M. Pepper, B.E. Bursten, The electronic structure of actinide-containing molecules: a challenge to applied quantum chemistry, Chemical Reviews, 91 (1991) 719-741.

[3] P. Pyykko, Relativistic effects in structural chemistry, Chem. Rev., 88 (1988) 563-594.

[4] T.A. Manz, D.S. Sholl, Chemically Meaningful Atomic Charges That Reproduce the Electrostatic Potential in Periodic and Nonperiodic Materials, Journal of Chemical Theory and Computation, 6 (2010) 2455-2468.

[5] T.A. Manz, D.S. Sholl, Improved Atoms-in-Molecule Charge Partitioning Functional for Simultaneously Reproducing the Electrostatic Potential and Chemical States in Periodic and Nonperiodic Materials, Journal of Chemical Theory and Computation, 8 (2012) 2844-2867.

[6] W. Tang, E. Sanville, G. Henkelman, A grid-based Bader analysis algorithm without lattice bias, J Phys-Condens Mat, 21 (2009) 084204.

[7] Y.M. Juan, E. Kaxiras, Application of gradient corrections to density-functional theory for atoms and solids, Physical Review B, 48 (1993) 14944-14952.

[8] M. Korling, J. Haglund, Cohesive and electronic properties of transition metals: The generalized gradient approximation, Phys. Rev. B, 45 (1992) 13293.

[9] K. Terada, F.W. Cagle, The Crystal Structure of Potarite (PdHg) with some comments on Allopalladium, Am. Miner., 45 (1960) 1093-1097.

[10] O. Levy, G.L.W. Hart, S. Curtarolo, Hafnium binary alloys from experiments and first principles, Acta Mater., 58 (2010) 2887-2897.

[11] S. Curtarolo, D. Morgan, G. Ceder, Accuracy of ab initio methods in predicting the crystal structures of metals: A review of 80 binary alloys, Calphad, 29 (2005) 163-211.

[12] S.V. Alapati, J. Karl Johnson, D.S. Sholl, Using first principles calculations to identify new destabilized metal hydride reactions for reversible hydrogen storage, Physical Chemistry Chemical Physics, 9 (2007) 1438-1452.

[13] S.N. Paglieri, J.D. Way, Innovations in palladium membrane research, Sep. Purif. Methods, 31 (2002) 1-169.

[14] S.G. Kang, K.E. Coulter, S.K. Gade, J.D. Way, D.S. Sholl, Identifying Metal Alloys with High Hydrogen Permeability Using High Throughput Theory and Experimental Testing, The Journal of Physical Chemistry Letters, 2 (2011) 3040-3044.

[15] M. Gupta, R.P. Gupta, D.J. Singh, Origin of the Anomalous Absence of Hydride Formation by $ZrPd_2$, Physical Review Letters, 95 (2005) 056403.

[16] A. Singh, B. Yakobson, First principles calculations of H-storage in sorption materials, Journal of Materials Science, 47 (2012) 7356-7366.

[17] S.V. Alapati, J.K. Johnson, D.S. Sholl, Large-scale screening of metal hydride mixtures for high-capacity hydrogen storage from first-principles calculations, Journal of Physical Chemistry C, 112 (2008) 5258-5262.

[18] K.M. Nicholson, D.S. Sholl, Computationally efficient determination of hydrogen isotope effects on the thermodynamic stability of metal hydrides, Physical Review B, 86 (2012) 134113.

[19] C. Ling, D.S. Sholl, First principles investigation of metal sulfides as membranes in hydrogen purification, Journal of Membrane Science, 329 (2009) 153-159.

[20] P. Kamakoti, B.D. Morreale, M.V. Ciocco, B.H. Howard, R.P. Killmeyer, A.V. Cugini, D.S. Sholl, Prediction of hydrogen flux through sulfur-tolerant binary alloy membranes, Science, 307 (2005) 569-573.

[21] D. Artman, T.B. Flanagan, Diffusion of hydrogen in rhodium-palladium alloys, The Journal of Physical Chemistry, 77 (1973) 2804-2807.

[22] P. Kamakoti, D.S. Sholl, Ab initio lattice-gas modeling of interstitial hydrogen diffusion in CuPd alloys, Physical Review B, 71 (2005) 9.

[23] R.V. Chepulskii, S. Curtarolo, Revealing low-temperature atomic ordering in bulk Co-Pt with the high-throughput ab-initio method, Appl. Phys. Lett., 99 (2011) 261902.

[24] L.J. Nelson, G.L.W. Hart, S. Curtarolo, Ground-state characterizations of systems predicted to exhibit $L1_1$ or $L1_3$ crystal structures, Physical Review B, 85 (2012) 054203.

[25] F.X. Coudert, M. Jeffroy, A.H. Fuchs, A. Boutin, C. Mellot-Draznieks, Thermodynamics of Guest-Induced Structural Transitions in Hybrid Organic−Inorganic Frameworks, Journal of the American Chemical Society, 130 (2008) 14294.

[26] M. Jeffroy, A.H. Fuchs, A. Boutin, Structural changes in nanoporous solids due to fluid adsorption: thermodynamic analysis and Monte Carlo simulations, Chemical Communications, (2008) 3275.

[27] J. Zang, S. Nair, D.S. Sholl, Osmotic ensemble methods for predicting adsorption-induced structural transitions in nanoporous materials using molecular simulations, Journal of Chemical Physics, 134 (2011) 184103.

[28] T.A. Manz, D.S. Sholl, Methods for Computing Accurate Atomic Spin Moments for Collinear and Noncollinear Magnetism in Periodic and Nonperiodic Materials, Journal of Chemical Theory and Computation, 7 (2011) 4146-4164.

[29] G. Henkelman, A. Arnaldsson, H. Jonsson, A fast and robust algorithm for Bader decomposition of charge density, Comput. Mater. Sci., 36 (2006) 354-360.

[30] M. Karelson, V.S. Lobanov, A.R. Katritzky, Quantum-chemical descriptors in QSAR/QSPR studies, Chemical Reviews, 96 (1996) 1027-1043.

[31] R. Griessen, A. Driessen, Heat of Formation and Band-Structure of Binary and Ternary Metal-Hydrides, Physical Review B, 30 (1984) 4372-4381.

[32] S. Trasatti, Electronegativity, work function, and heat of adsorption of hydrogen on metals, Journal of the Chemical Society, Faraday Transactions 1: Physical Chemistry in Condensed Phases, 68 (1972) 229-236.

CHAPTER 5
RESULTS FOR NON-Pd BASED INTERMETALLICS

5.1 Introduction

In the previous chapter, the results of the calculations performed for all Pd-based intermetallics were described. In this chapter, we detail the results obtained after the systematic screening of non-Pd based intermetallics shortlisted using the criteria described in chapter 3. Two screening parameters, H solubility and the H diffusion activation barrier, are used to screen favorable candidates among the list of potential membrane materials. In this chapter, we screen materials based on the same criteria as Pd-based intermetallics. However, the number of DFT calculations performed to screen this large set of materials (981 materials, 1001 structures) has been greatly reduced using the methods described in chapter 3.

5.2 Lattice Constants

To ensure that DFT calculations give accurate lattice constants for the different materials considered, the lattice constants of the structures obtained from the ICSD [1] were compared with those obtained from DFT. The crystal structures obtained from the ICSD were used as input in geometric relaxation calculations performed using DFT. 169 of the candidate structures obtained from ICSD had partial occupancies or incomplete structures and could not be directly used as an input for DFT calculations. For these structures, the positions of the atoms were obtained from prototype structures and the lattice constants listed in the ICSD were used to construct a unit cell. For 158 structures, the resulting lattice parameters predicted by DFT calculations were in good agreement with the lattice constants listed in the ICSD. For the remaining 11 structures a difference in cell volume > 5% was found. These 11 structures are listed in Table 5.1 marked with an asterisk. In the remaining 832 structures whose structure files from the ICSD were directly used in DFT calculations, 25 structures had lattice constants that result in cell

volumes that differ by greater than 5% from the values listed in ICSD. These 25 structures are listed in Table 5.1 (without the asterisk). For these structures, the DFT optimized structures were used for further calculations. The lattice constants calculated using DFT for the remaining 807 structures obtained directly from ICSD are in good agreement with the ICSD values. We used the DFT optimized structures for all materials as a starting point for the next steps in the screening process.

Table 5.1: Comparison of the experimental and the DFT calculated structural parameters of intermetallics for structures where there was > 5% deviation in cell volume from the reported ICSD structures. All distances are in Angstroms and volume in Å^3. The structures marked with an asterisk are the structures for which the structures were generated manually and not using the cif files from ICSD.

Material	ICSD values	ICSD volume	Calculated lattice parameters	DFT volume	DFT vol./ ICSD vol.
$InSn_4$	a=3.21,c= 3, α =β=90°,γ=120°	26.81	a=3.3,c= 3.6, α=β=90°,γ=120°	47.21	1.45
Pt_2Re_3*	a=2.77,c= 4.43,α=β=90°,γ=120°	29.32	a=2.96,c= 4.73,α=β=90°,γ=120°	46.16	1.41
NiRu	a=2.61, c=4.20, α=β=90°,γ=120°	24.70	a=2.74, c=4.6, α=β=90°,γ=120°	38.81	1.40
Ga_2Sr_1*	a=4.35,c= 4.74, α=β=90°,γ=120°	77.55	a=4.45,c= 5.15, α=β=90°,γ=120°	120.71	1.32
$Mg_{47}Pb_3$*	a=3.21,c=5.42, α=β=90°,γ=120°	46.86	a=3.26,c=5.58, α=β=90°,γ=120°	82.37	1.27
In_9Pb	a=3.27,c=5.03, α=β=γ=90°	53.82	a=3.57,c=5.25,α=β=γ=90°	66.95	1.24
CrFe*	a=2.9 ,α=β=γ=90°	24.39	a=3.1 ,α=β=γ=90°	29.79	1.22
Ti_7Zr_3*	a=3.03,c= 4.83, α=β=90°,γ=120°	38.40	a=3.05,c= 5.03, α=β=90°,γ=120°	46.80	1.22
IrPt*	a=3.88 ,α=β=γ=90°	58.28	a=4.12 ,α=β=γ=90°	90.52	1.20
CoV_3*	a=4.68 ,α=β=γ=90°	102.24	a=4.98 ,α=β=γ=90°	123.51	1.20
TaTi	a=3.29 ,α=β=γ=90°	35.48	a=3.49 ,α=β=γ=90°	59.32	1.19
Co_8Sn_{44}*	a=12.14 ,α=β=γ=90°	1787.11	a=12.84 ,α=β=γ=90°	2708.8	1.18
$Cr_{13}Ga_{13}$	a=12.63,c=7.79,α=β=90°,γ=120°	1074.61	a=12.75,c=7.89,α=β=90°,γ=120°	1269.2	1.18
Pt_3V_2*	a=3.86 ,α=β=γ=90°	57.56	a=4.05 ,α=β=γ=90°	91.13	1.16
Cu_4Ti_3	a=3.13,c=19.97,α=β=γ=90°	195.09	a=3.35,c=20.11,α=β=γ=90°	225.68	1.16
Ta_6Zn_7	a=5.04,c=27.53, α=β=90°,γ=120°	604.37	a=5.24,c=27.73,α=β=90°,γ=120°	697.87	1.15
$Be_{17}Zr_2$	a=7.54,c=11.02, α=β=90°,γ=120°	542.04	a=7.68,c=11.15,α=β=90°,γ=120°	625.89	1.15
$Mo_{17}Pt_3$*	a=4.89 ,α=β=γ=90°	124.18	a=5.20 ,α=β=γ=90°	191.10	1.13

Table 5.1 continued

Material	ICSD values	ICSD volume	Calculated lattice parameters	DFT volume	DFT vol./ ICSD vol.
$AuBe_{12}$	a=7.243,c=4.25, α=β=γ=90°	223.06	a=7.45,c=4.55,α=β=γ=90°	252.54	1.13
$CdLi_3$*	a=4.26 ,α=β=γ=90°	77.25	a=4.41 ,α=β=γ=90°	122.02	1.11
NbTa	a=3.3,α=β=γ=90°	35.94	a=3.42,α=β=γ=90°	54.87	1.11
Na_7Ga_{13}	a=15.63,b=14.9,c=21.7,α=β=γ=90°	5073.67	a=15.9,b=15.7,c=22.5,α=β=γ=90°	5598.7	1.10
Co_7Cr_8	a=b=8.81,c=4.56, α=β=γ=90°	353.93	a=b=8.91,c=4.86,α=β=γ=90°	385.83	1.09
Cs_4Sn_{23}	a=b=c=12.10,α=β=γ=90°	1769.80	a=b=c=12.43,α=β=γ=90°	1920.5	1.09
Ca_7Sn_6	a=7.87,b=23.8,c=8.46,α=β=γ=90°	1586.14	a=7.98,b=24.02,c=8.9,α=β=γ=90°	1705.8	1.08
$Fe_{23}Y_6$	a=b=c=12.08,α=β=γ=90°	1763.67	a=12.35,α=β=γ=90°	1883.6	1.07
$Sn_{10}Y_{11}$	a=11.53,c=16.91,α=β=γ=90°	2248.03	a=11.83,c=17.02,α=β=γ=90°	2381.9	1.06
Ba_5Pb_3	a=9.04,c=16.81, α=β=γ=90°	1374.23	a=9.24,c=17.09,α=β=γ=90°	1459.1	1.06
Nb_3Os_2	a=b=9.86,a=5.06, α=β=γ=90°	492.02	a=b=9.88,c=5.32, α=β=γ=90°	517.00	1.05
$Ba_{11}Bi_{10}$	a=b=13.21,c=19.37, α=β=γ=90°	3389.51	a=b=13.41,c=19.58,α=β=γ=90°	3565.7	1.05
Pb_4Sr_5	a=8.5,b=17.3,c=9.01, α=β=γ=90°	1319.51	a=8.58,b=17.5,c=9.07,α=β=γ=90°	1385.4	1.05

Figure 5.1 shows the 981 intermetallics examined in this work as a combination of their elements. The colors represent the number of intermetallic structures that are a combination of the particular elements. For example, two intermetallics of Cu and Sc were considered in this study, CuSc and Cu_2Sc, as indicated by the number 2 in the plot. Only structures that satisfy the various factors for favorable membrane materials such as melting temperature, existence in high or low pressure phases (listed in ICSD) and experimental observation as described in Table 3.1 are listed in this figure.

One goal of constructing this Figure 5.1 was to map the element combinations screened in this work and to determine if certain element groups had a larger number of potential materials in comparison with others. However, the materials are distributed across element combinations with no obvious visible trends. Figure 5.1 also highlights the possibility of identification of a large number of intermetallic structures that are either not listed in the ICSD or have not been identified yet (indicated by an 'x'). The white squares represent the existing intermetallic combinations not considered in this work because they did not meet the physical criteria (computationally obtained structures, high or low pressure phase existence etc.) or they did not belong to the top 15 highest populated space groups.

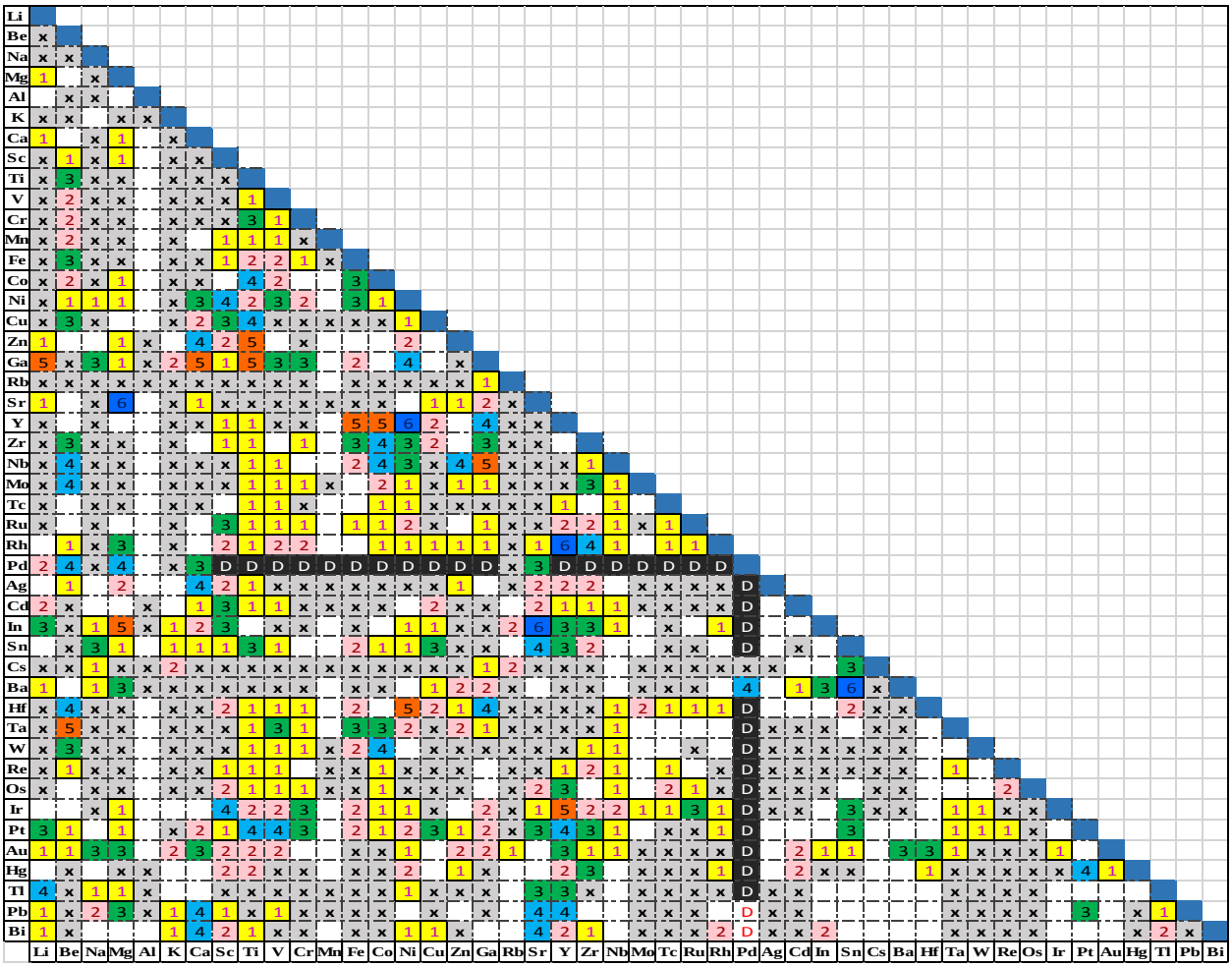

Figure 5.1: Summary of the intermetallics that were considered in this work. The numbers represent the number of intermetallics of each element combination that were studied. 'D' represents materials that have been studied previously in Chapter 4. The 'x' represents element combinations for which no intermetallic compounds have been listed in the ICSD.

5.3 Solubility

Using the efficient methods described in chapter 3 we calculated the H solubility of 1001 structures from 15 space groups. We also calculated the vibrational frequencies and zero point energies of interstitial H using DFT. The frequencies were calculated by making small displacements of the H around the local minima at the binding sites with the assumption that the vibration of the interstitial H atom is decoupled from the phonons of the metal lattice [2]. The binding energy and zero point energies were used to calculate the solubility at dilute H loadings as described in Chapters 2 and 3[3]. One

of the assumptions we made in calculating hydrogen solubility was that interstitial H does not significantly alter the unit cell volume. Based on the calculations performed for Pd-based intermetallics where no significant increase in volume were observed due to the interstitial hydrogen, lattice expansion was neglected in the calculation of binding energy for the 981 materials in this work[4].

Figure 5.2 shows the solubility of the intermetallics measured in hydrogen per metal atom (H/M) at 1 atm H_2 and 600 K plotted as a function of the volume/metal atom ($Å^3$) for the materials that belong to the space group Cmcm. For the materials with multiple phases, solubility was calculated using the structure stable at 600 K. For the materials shown in Fig. 5.2, 8 of the 29 structures were selected to have diffusion characterized based on this criterion. Similar plots were generated for the remaining 14 space groups. The other 14 plots are in Figure E.1 in Appendix E. A temperature of 600 K was chosen since it lies within the target operating temperatures of these membranes [4]. A solubility range of 10^{-1}-10^{-5} H/M was used to screen favorable candidates as was used for Pd-based intermetallics. The materials that have solubility that lie in this range were chosen for diffusivity calculations.

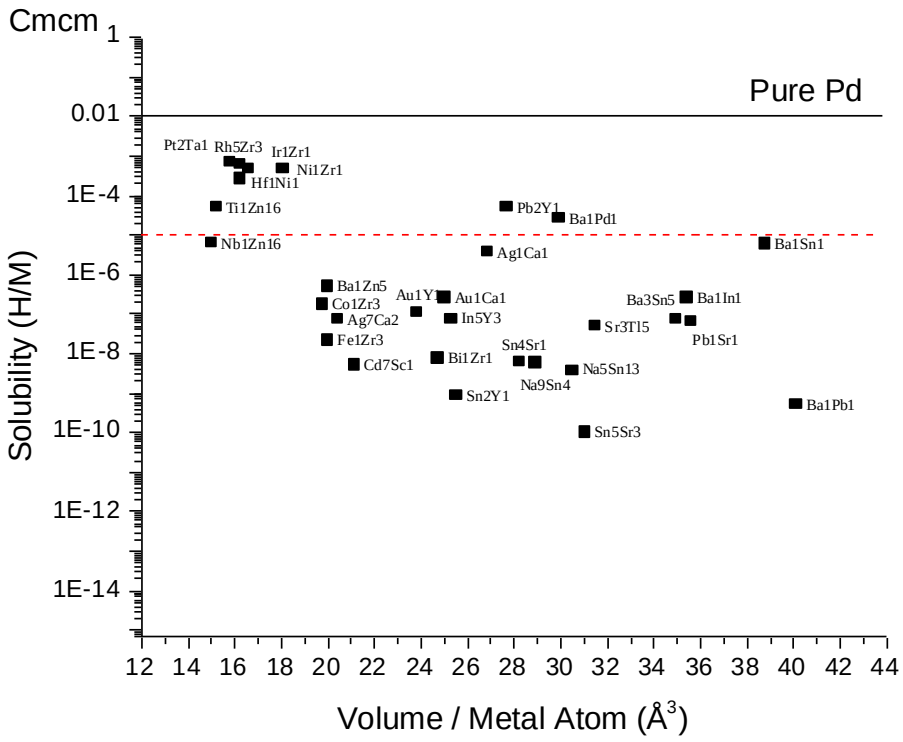

Figure 5.2: The solubility (H/M) of selected intermetallics that belong to Cmcm space group at 600 K and 1 atm H_2 plotted as a function of the volume/metal atom. The black solid line is the solubility of pure Pd. The red dashed line is the lower limit of solubility used for screening materials (10^{-5} H/M). Only the materials that lie between 10^{-1}-10^{-5} H/M at 600 K and 1 atm H_2 were used for further calculations.

Our results for H solubility in Fig. 5.2 and E.1, the results show that the H solubility is not correlated with atomic volume, as observed previously in Pd-based intermetallics [4]. There is no obvious trend among the element combinations of the materials that have solubilities in the favorable range. However, a large number of the favorable materials have one element that forms favorable hydrides i.e. bind hydrogen very favorably. These elements include Mg, Sc, Y, Ti, Zr and Hf [5, 6]. Out of 161 favorable materials chosen using the screening criteria described in Chapter 2, 113 (70.2%) have at least one element that is among the five elements listed above that form very stable hydrides for example, $FeHf_2$[6]. However, this trend is not predictive in nature since there are intermetallics that include a strong hydride former have lower solubility than

10^{-5} H/M. Cr_2Ti is an example of such an intermetallic, with a solubility of 7.3×10^{-7} H/M at 600 K and 1 atm H_2.

Another view of the H binding energies of all binary intermetallics in this work is given in Figure 5.3 where the distribution of the binding energy is shown in the form of a histogram for the 981 materials. The binding energy of H is given by [3]

$$E_b = E_{H-Metal} - E_{Metal} - \frac{1}{2}E_{H_2} \qquad (1)$$

where $E_{H-Metal}$ is the energy of the metal atoms including the hydrogen, E_{Metal} is the total energy of the bare metal and E_{H_2} is the total energy of a hydrogen molecule. For materials with multiple binding sites, the energy of the most favorable binding site is plotted in Figure 5.3.

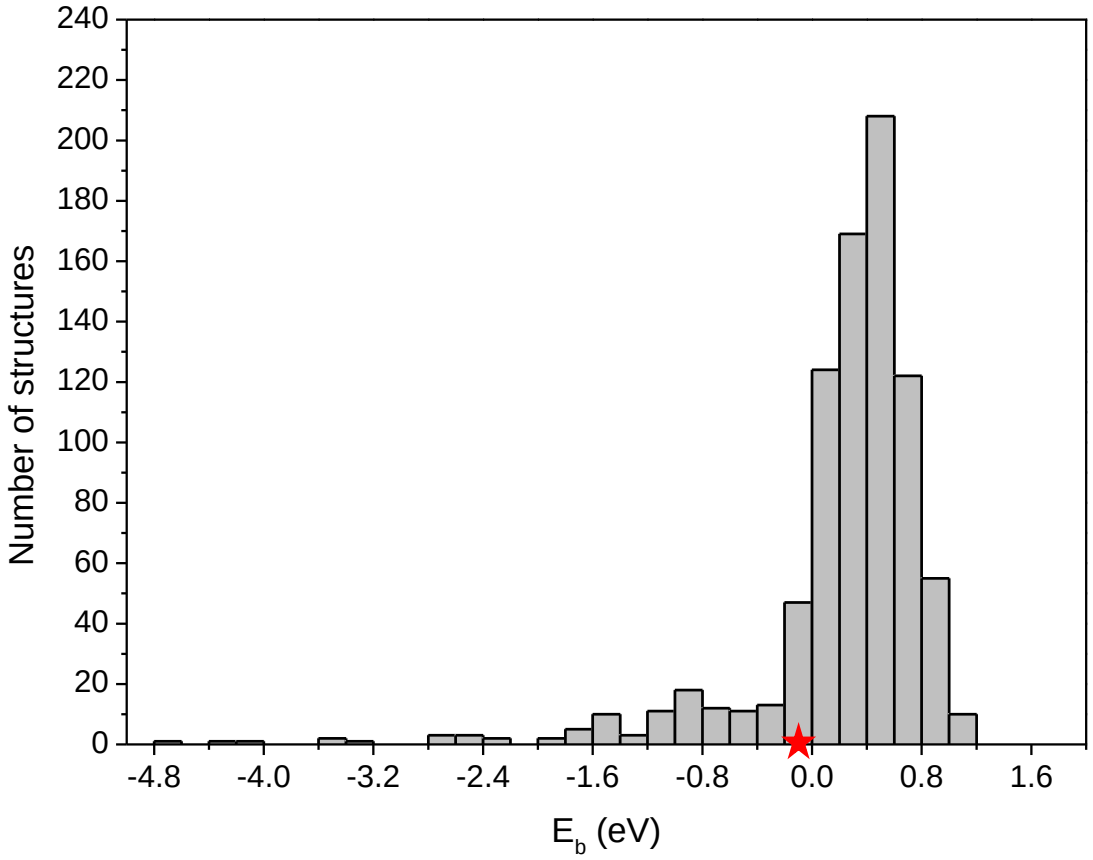

Figure 5.3: Histogram showing the binding energy for 981 materials at 600 K. The binding energy of pure Pd is marked with a red star.

One interesting observation from the histogram in Fig. 5.3 is that 62% of the structures have binding energies that lie between 0.1-0.8 eV. For all of these materials, the existence of interstitial H is energetically unfavored. The lowest binding energy encountered in our calculations is that of Ti_7Zr_3 which has E_b= -4.78 eV. Materials that exhibit such favorable binding energies have a strong tendency to form hydrides. This result is not unexpected since intermetallics formed by a combination of elements that individually form very stable hydrides such as Ti and Zr can demonstrate hydride forming tendencies.

From Fig. 5.3 one can also observe that only 25 materials have H solubilities more favorable than pure Pd but within the range for dilute loading i.e. between -0.12 eV and -0.3 eV. This indicates that the number of materials with H solubilities in the favorable range for membrane applications is very small in comparison to the large number of possible intermetallics. In this case only ~2.5% of all materials considered (binary intermetallics) show favorable solubilities for use as membranes. Such trends emphasize the value of computational screening of materials making experimental studies infeasible in the discovery of new intermetallics for hydrogen separation.

Figure 5.3 shows 92 materials that were found to have binding energies < -0.3 eV. These materials bind H very favorably and have a tendency to form hydrides. Hydride formation is not ideal for membrane materials since hydride formation can result in the alteration of structure, composition and destroys the integrity of the membrane [7, 8]. Solubility calculations performed using Sieverts' law cannot be reliably extended to calculate solubility of materials with very favorable H binding energies. Hence, these materials were removed from further consideration and are not shown in the solubility plots similar to Figure 5.2. These materials and their binding energies are listed in Table 5.2.

Table 5.2: List of intermetallic compounds and the energy of the most favorable H binding site. The solubility for these materials cannot be reliably calculated using Sieverts' law. These materials are not favorable for use as membranes.

Material	E_b (eV)	Material	E_b (eV)
Ti_7Zr_3	-4.78	Ga_2Y_3	-0.96
Ga_4Ti_6	-4.36	$Ga_{39}Na_{22}$	-0.92
$IrTi_3$	-4.03	Be_5Hf	-0.92
BiK_3	-3.56	Li_3Bi	-0.91
Ga_3Zr	-3.45	Ca_5Ga_3	-0.91
Ga_3Nb_5	-3.38	$CaGa_2$	-0.91
In_2Li_3	-2.8	GaLi	-0.91
$GaHf_2$	-2.77	$BaMg_2$	-0.9
$Bi_{10}Ca_{11}$	-2.7	CsRb	-0.89
MgIn	-2.6	Mg_2Sn	-0.87
Ga_3Hf_5	-2.56	Be_2Zr	-0.87
LiZn	-2.49	$Mg_{38}Sr_9$	-0.87
Ga_5Ni	-2.4	$Ga_{14}Li_3$	-0.86
$Bi_{10}Sr_{11}$	-2.3	CdLi	-0.86
Ga_4Nb_5	-1.93	$Ca_{11}Ga_7$	-0.85
Ga_3Ti_5	-1.86	$AuNa_2$	-0.84
$CaNi_2$	-1.78	Ga_3Hf_1	-0.81
$NaGa_4$	-1.75	Ga_3Sc_5	-0.78
$Mg_{23}Sr_6$	-1.7	$Ca_{13}Cd_{76}$	-0.76
$LiTl_1$	-1.65	Li_3Tl	-0.76
HfTi	-1.62	$CaMg_2$	-0.76
Ga_4Ti_5	-1.6	Ga_3Nb_2	-0.73
In_3Li_{13}	-1.6	Ga_2Li_3	-0.71
Ga_3Nb	-1.57	CaSr	-0.71
InNa	-1.57	$Ga_{10}Hf_{11}$	-0.67
$CdLi_3$	-1.56	TiZr	-0.67
$BaGa_4$	-1.56	K_8Sn_{46}	-0.65
Li_3Pd	-1.54	KPb_2	-0.65
Ga_3K_2	-1.54	Li_5Tl_2	-0.61
Li_2Sr_3	-1.5	$Na_{13}Pb_5$	-0.59
Sr_6Li_{23}	-1.46	HfSc	-0.57
$CaLi_2$	-1.35	Mg_2Pb	-0.56
$MgPd_3$	-1.34	$GaZr_2$	-0.56
Ga_4Sr	-1.34	$LiPt_2$	-0.54
$LiPt_7$	-1.2	$Ca_{31}Sn_{20}$	-0.52
$Be_{17}Hf_2$	-1.2	$BaLi_4$	-0.52
LiMg	-1.2	Mg_3In	-0.47
$GaTi_2$	-1.2	$BiSr_2$	-0.47
MgSc	-1.07	Ba_6Mg_{23}	-0.45
Ga_5Mg_2	-1.04	$Ba_{10}Ga$	-0.42
Be_2Hf	-1.04	Ag_3Ca_5	-0.38
MgRh	-1.04	Cs_6K_7	-0.37

Table 5.2 continued

Ga_7Li_2	-1.03	NaTl	-0.35
HfOs	-1.03	$BiCa_2$	-0.33
GaY	-1.03	Au_2Na	-0.33
$LiPd_7$	-0.98	In_4K	-0.3

Based on the solubility based screening criteria, 161 materials were chosen for calculation of activation barriers for diffusion.

5.4 Diffusivity

It is unclear, if the methods used to reduce the number of DFT calculations for solubility predictions for 981 materials (Chapter 3) would be applicable to reduce the number of DFT calculations for the prediction of transition state energies. The method described in chapter 2 was used for rigorous prediction of the transition sites and the transition state energies for two of the most populated space groups: Fm3-m and P63/mcm. For three structures from Fm-3m space group, CrPt and Fe_3Ni and $IrSn_2$, a detailed transition state search was carried out using the method developed by Hao and Sholl [9]. Graphical analysis of the diffusion path has been used earlier to study the diffusion in metal sulfides [10]. Using this method, the effective diffusion path was estimated using the path between the most energetically favored sites which have the lowest activation energy barrier in the three materials [10]. It was observed that though the activation energies for the three materials are different, the geometrical location of the transition state in the effective diffusion path remains the same.

However in the case of P63/mcm space group where Pd_3Y_5, Hf_5Ir_3 and AgCd were chosen, the location of the transition state in the effective diffusion path in AgCd was different from the other two materials. This difference is due to the different geometry of the most favorable binding site in AgCd in comparison to Pd_3Y_5 or Hf_5Ir_3. In AgCd, an octahedral site with 6 neighboring metal atoms was the most favorable, unlike Pd_3Y_5 or Hf_5Ir_3 where a tetrahedral site is most favorable. This results in a different effective diffusion path of H in AgCd in comparison to the other two materials. Hence, the

assumption of the effective diffusion path remaining geometrically identical across crystal structures within a space group is not valid.

As a result, DFT calculations for the full list of possible transition sites generated using the method of Hao and Sholl for the representative structures from each of the 15 space groups (listed in Table 3.2 in Chapter 3) were performed for transition state prediction. The prediction of the transition sites using this method includes many duplicates for each of the materials. Using only the unique sites after removal of the duplicates by performing DFT calculations reduces the number of calculations that need to be performed by up to 50% in many space groups. A list of the diffusion activation energies for the 161 materials is given in Appendix E, Table E.2. In Fig. 5.3, a histogram of these activation energies predicted for 161 materials is shown.

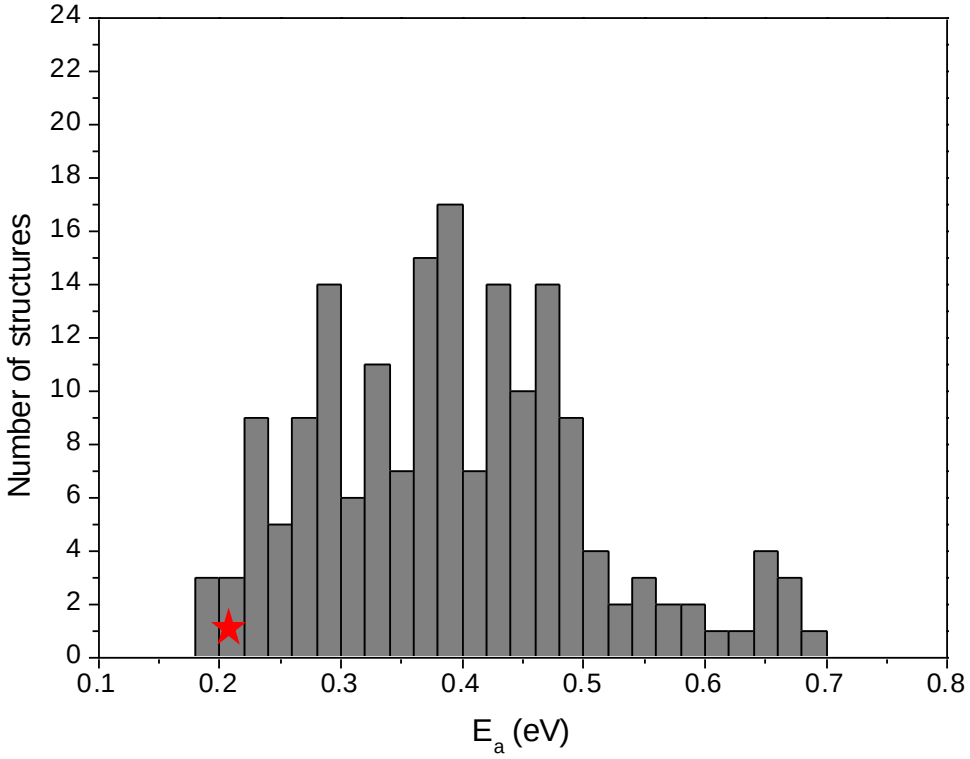

Figure 5.4: Histogram showing the diffusion activation energy for the 161 materials described in the text. The diffusion activation energy of pure Pd is marked with a red star.

Among the materials with favorable solubilities, the activation energy ranges from 0.19 eV for Sc_2Fe to a maximum of 0.69 eV for $SnTi_2$. The intermetallic Sc_2Fe has Fe as one of its constituents and bcc-Fe has the highest diffusivity of H among all pure metals [11]. From Fig. 5.3 and 5.4, it can be observed that among the intermetallics we have studied, a majority of the materials have higher diffusion activation energies than pure Pd.

The ensemble average binding energy E_{ens} is a useful descriptor of the effective binding energy of the H in the material at given conditions. It is defined by [4]

$$E_{ens} = \frac{1}{n}\sum_{i=1}^{n}\frac{E_i e^{\frac{-E_i}{kT}}}{e^{\frac{-E_i}{kT}}} \qquad (2)$$

where n is the number of binding sites in the material, E_i is the binding energy of each binding site, k is the Boltzmann's constant and T is the temperature. To examine whether a correlation exists between H binding energies and transition state energies, the ensemble average binding energies and activation barriers for 161 selected materials was plotted in Figure 5.4. There is no visible correlation between the two quantities. For example, there are materials that have binding energies ~-0.1 eV but have transition state energies that vary from 0.2 to 0.45 eV. Using this plot, we can easily determine the region where materials with favorable properties for hydrogen separation exist. The red box highlights the portion of the graph that has the activation barriers and binding energies that would make a material a favorable candidate for membrane-based hydrogen separation.

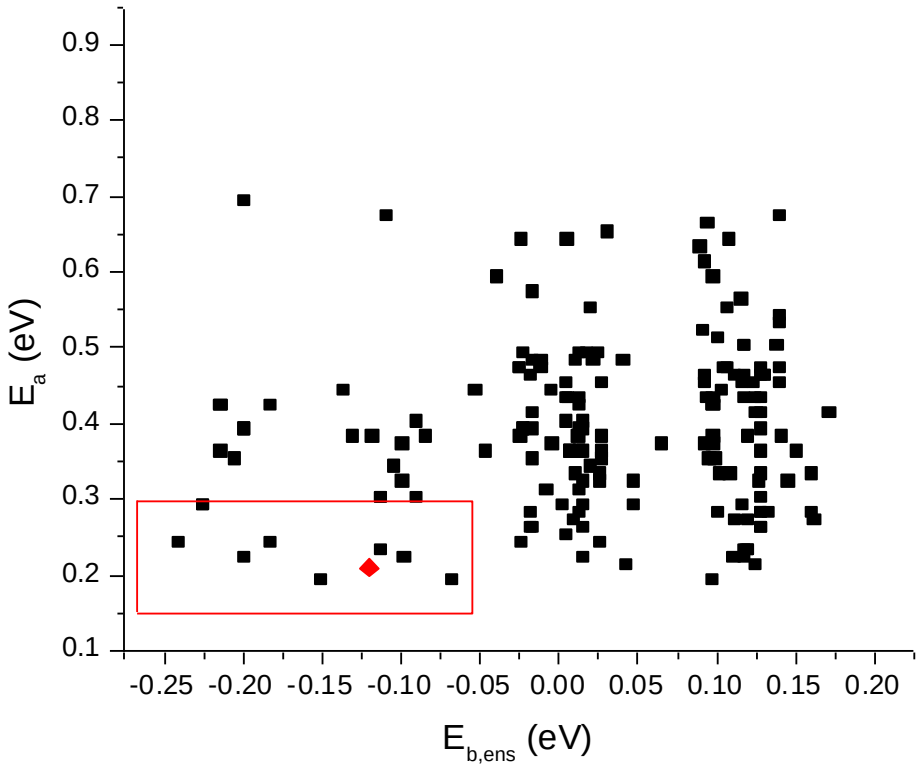

Figure 5.5: The ensemble average binding energy at 600 K and activation energy barriers for 161 materials. The red box highlights the favorable region for materials suitable for hydrogen separation. The red diamond represents pure Pd. 8 materials lie in the favorable region for potential use as membranes for hydrogen separation.

Diffusivity calculations for the 161 selected materials were performed using Kinetic Monte Carlo at various temperatures [12]. The procedure is described in detail in Chapter 2. 8 materials were found to have diffusivity greater than 10^{-13} m^2/s at all temperatures from 400-1200 K. The diffusivity of these materials is shown in Figure 5.6.

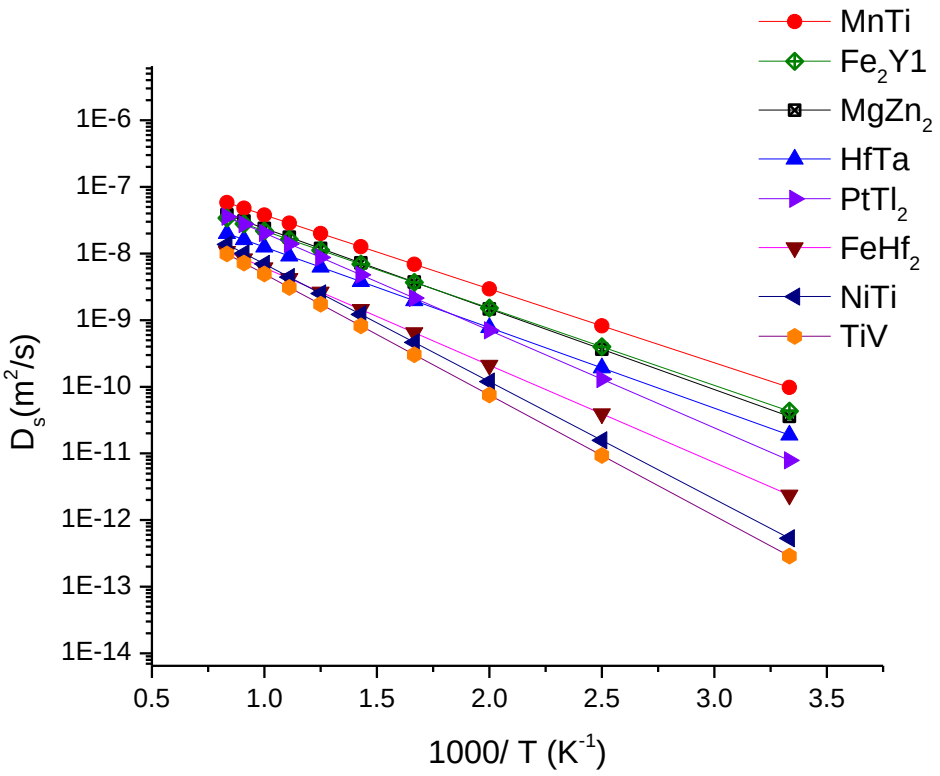

Figure 5.6: H diffusivity Diffusivity of 8 selected intermetallics chosen on the basis of their solubility and activation barrier predicted by DFT based methods.

The Arrhenius prefactor (D_o) and diffusion activation energy of these materials is listed in Table 5.3. The prefactor was extracted by fitting the Arrhenius equation to the diffusivity data for the 8 selected materials for the all temperatures [12].

Table 5.3: Arrhenius prefactor, D_o, and diffusion activation barriers for the 8 intermetallics shown in Figure 5.6.

Material	D_o (m^2/s)	E_a (eV)
MnTi	4.42×10^{-7}	0.22
Fe_2Y	3.15×10^{-7}	0.23
$MgZn_2$	3.87×10^{-7}	0.24
HfTa	1.77×10^{-7}	0.25
$PtTl_2$	5.34×10^{-7}	0.29
$FeHf_2$	1.95×10^{-7}	0.31
NiTi	4.04×10^{-7}	0.35
TiV	3.21×10^{-7}	0.36

5.5 Permeability

Using the solubility and diffusivity, the permeability of H in the selected intermetallics was calculated. The predicted permeabilities of the 8 intermetallics with the highest permeability are shown in Figure 5.7 as a function of temperature at a pressure of 1 atm H_2. These materials were chosen since their H permeabilities are within an order of magnitude of the permeability of pure Pd at all temperatures > 500 K.

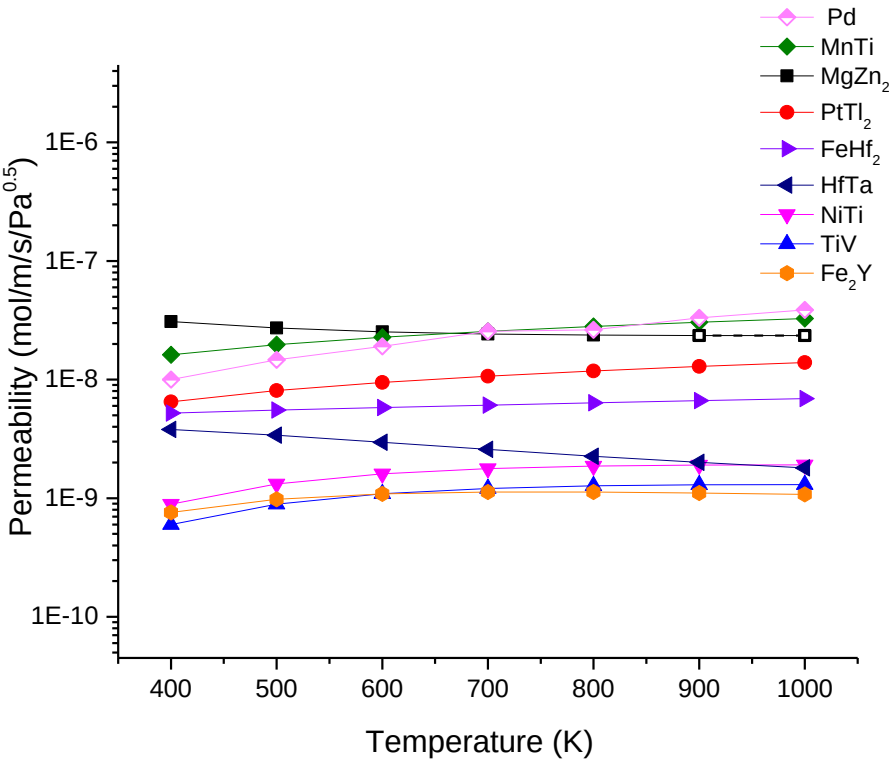

Figure 5.7: Plot of permeability of the materials having permeability > 10^{-9}mol/m/s/$Pa^{0.5}$ at all temperatures > 500 K. The permeability of pure Pd is shown for comparison. Lines are to guide the eye.

Two materials, MnTi and $MgZn_2$, show permeabilities that are similar to that of pure Pd. The most favorable binding energy in MnTi ($MgZn_2$) is -0.19 eV (-0.22 eV) and the activation barrier for diffusion is 0.24 eV (0.27 eV). These materials have higher solubility than pure Pd but have higher diffusion activation barriers than pure Pd, resulting in comparable permeabilities to that of pure Pd. At temperatures below 700 K, the predicted permeability of $MgZn_2$ and MnTi is higher than that of pure Pd. This is because at lower temperatures, the solubility is higher and it has a higher influence on the permeability than diffusivity at lower temperatures. At higher temperatures, the predicted permeability of pure Pd and MnTi is higher than $MgZn_2$ due to the dominant effects of diffusivity on the permeability over solubility.

In $MgZn_2$, which has a P63/mmc structure, the most favorable binding site has H surrounded by 5 Zn and 1 Mg atom and the transition site geometry is a bridge site between 2 Zn atoms and 1 Mg atom. H hops from the octahedral site to a tetrahedral site surrounded by 3 Zn and 1 Mg atom. MnTi has a Pm3-m crystal structure where the most favorable binding site is a tetrahedral site consisting of 2 Mn and 2 Ti atoms and the transition site is surrounded by 4 Mn atoms and 1 Ti atom. The octahedral site consists of 3 Mn and 3 Ti atoms. From the analysis of the distance between H and the nearest metal atoms in both these materials in all three types of sites, no simple trends could be identified that result in the predicted favorable binding and diffusion activation barriers. This is in agreement with a similar analysis done previously, where no electrostatic or geometric trends were visible that explained favorable properties in materials [4]. This leads us to the conclusion that no simple predictive trends can explain why some materials are more favorable than the others since H binding is a complex interplay of various factors that include geometry, chemistry of the elements (band interactions) and must be evaluated on a case-by-case basis.

The phase diagram of $MgZn_2$ reveals that this intermetallic phase has a melting temperature of 588°C [13, 14] making this intermetallic unsuitable for use at temperatures above 861 K. In Figs. 5.6 and 5.7, the diffusivity and permeability for $MgZn_2$ above 861 K is shown using open symbols and dashed lines.

MnTi is a stable intermetallic with a melting temperature of 1200 °C according to Massalski et. al. [14]. The minimum temperature in this phase diagram was 500 °C. Using the procedure developed by Alapati and Sholl to evaluate the stability of phases for combinations of up to four elements and hydrogen, we predicted the phase diagram of Mn-Ti-H at 1, 3 and 10 atm H_2 pressures [15-17]. Figure 5.9 shows the predicted Mn-Ti-H phase diagram at 1 atm H_2. The phase diagrams at 3 and 10 atm H_2 are in Figure E.2 in Appendix E.

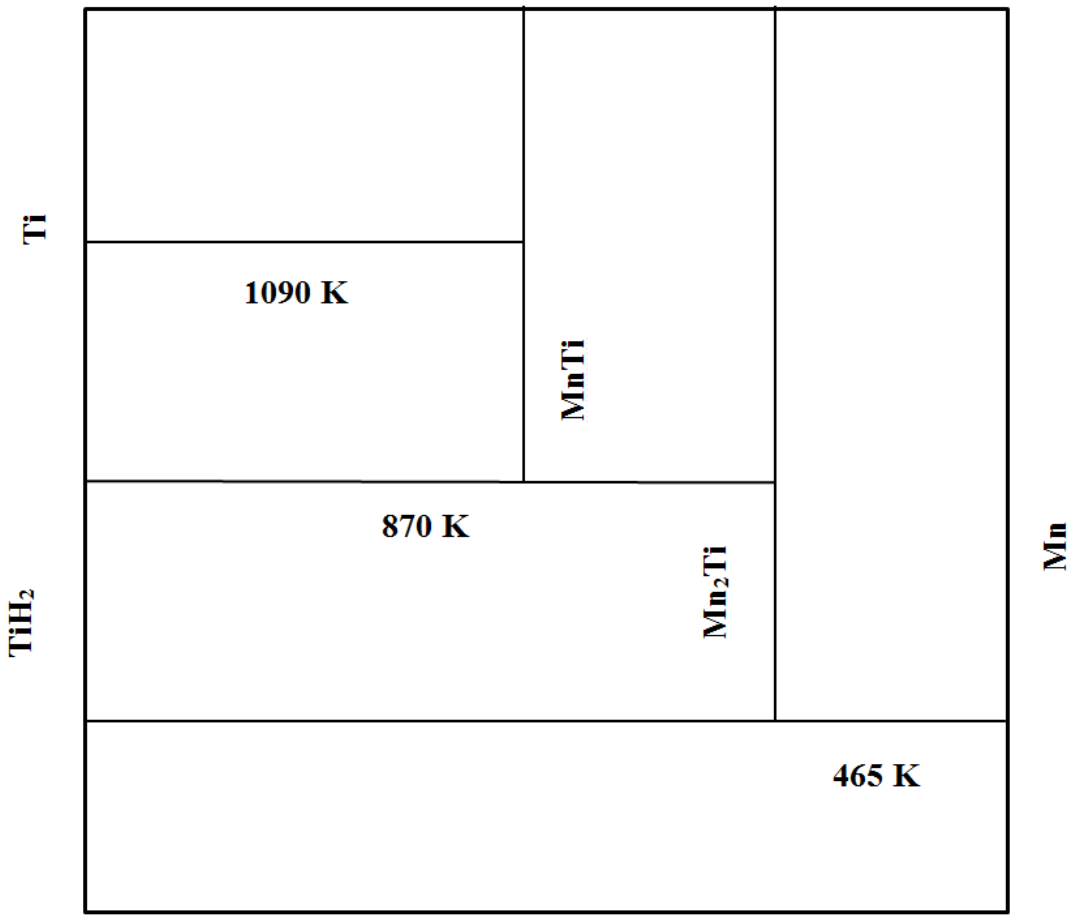

Figure 5.8: Mn-Ti-H calculated equilibrium phase diagram at 1 atm H_2.The decomposition temperatures of various phases are shown using horizontal lines. The vertical lines indicate the compounds formed. No entropic (vibration effects) were considered in these calculations.

According to our calculations, MnTi is formed at temperatures greater than 870 K. At lower temperatures, MnTi separates to form Mn_2Ti (870-465 K) and further dissociates into the more stable Mn and TiH_2 phases. These calculations were performed at 0 K and do not include vibrational effects. Inclusion of vibrational effects typically lowers the decomposition temperatures but does not qualitatively affect the predicted phase diagram [18]. Since MnTi is thermodynamically stable at higher temperatures, methods such as quenching can be used to synthesize intermetallic MnTi temperatures below 870 K.

From the NiTi phase diagram, the intermetallic structure is stable only from 903 K-1583 K reported in 1986 [14]. However, a stable Pm3-m structure was reported at 313 K in 2009[19] making this intermetallic a potential candidate for hydrogen separation membrane. Fe_2Y is also a stable intermetallic with a melting temperature of 1150 °C [14].

The phase diagram reported by Massalski et.al [14] for $PtTl_2$ does not show an intermetallic structure at this composition. However, a crystal structure with $CuAl_2$ (C16)-type structure has been reported for $PtTl_2$. The melting temperature of this intermetallic has not been reported [20].

$FeHf_2$ has H solubility of 0.09 H/M at 1 atm H_2 and 600 K. At temperatures below 400 K, the solubility is higher than what can be reliably calculated by Sieverts' law (> 0.1 H/M). These results are in agreement with previous literature where $FeHf_2$ has H/M of 1.03 at 3 atm H_2 at 300 K and is reported to form hydrides at these conditions and also at higher H_2 pressures [21]. Hence this material is favorable for use as a membrane only at low hydrogen pressures and high temperatures. This is similar to the properties of pure Pd [22].

Two of the intermetallics which have predicted H permeabilities comparable to pure Pd, TiV and HfTa do not have intermetallic structures reported in literature. These materials had structure files that could not be used directly from ICSD and were generated by hand using representative structures from each space group (Im3-m). Our calculations indicate that, if they exist, these intermetallics may have useful properties. This suggests further work to refine the phase diagram of Ti-V and Hf-Ta would be worthwhile [23, 24].

To understand if the variation in the performance of these intermetallics is mainly due to solubility or diffusivity, we plotted the diffusivity and solubility of 161 materials normalized to pure Pd in Figure 5.8. If the variation is primarily due to one property (solubility or diffusivity), it would be possible to model membrane performance focused on this property alone [25]. This would greatly reduce computational efforts to predict H permeability in intermetallics in addition to making the screening process rapid enabling the study of larger sets of materials.

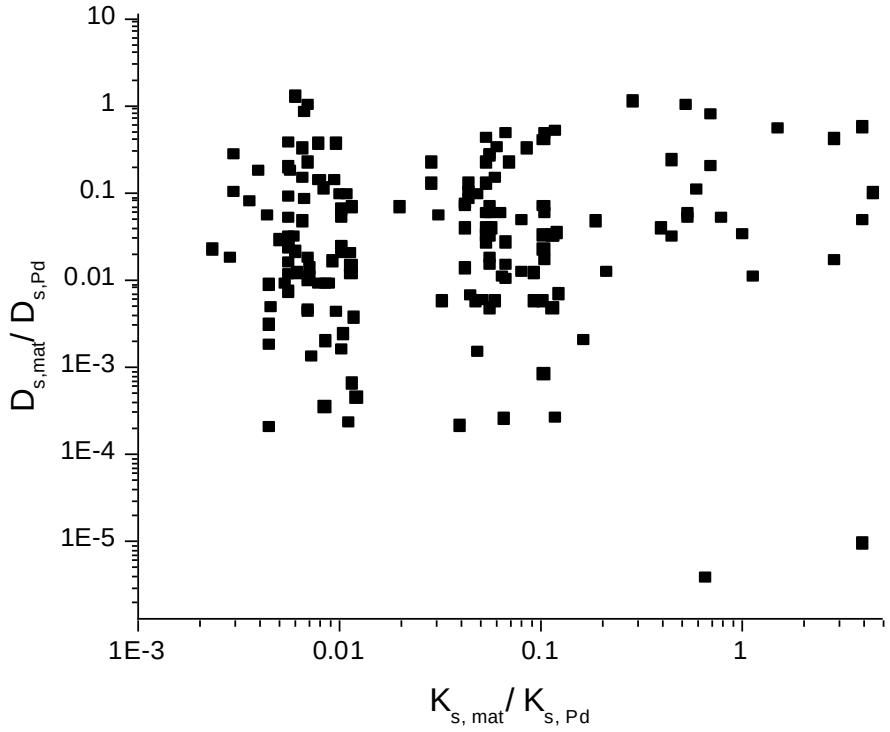

Figure 5.9: Normalized diffusivity as a function of normalized solubility for 161 intermetallics. The reference system is pure Pd. All properties were calculated at 600 K and 1 atm H_2.

The diffusivity and solubility plotted in Fig. 5.8 are calculated at 600 K and 1 atm H_2. From this plot, we can observe that neither the solubility nor the diffusivity alone can predict the overall permeability of binary intermetallics. In the case of both

solubility and diffusivity there are examples where one quantity is relatively invariant among the materials while the other varies by many orders of magnitude. Thus, for prediction of H permeability in binary intermetallics, assessment of both solubility and diffusivity calculations is necessary.

5.6 Conclusion

In summary, we have used DFT-based methods to systematically examine hydrogen solubility, diffusivity and permeation through 981 binary intermetallics (1001 structures). This is one of the largest sets of materials to be examined at this high level of theory. These calculations required no input apart from the structure of the materials and are useful for identifying suitable materials for hydrogen separation.

Solubility was shown to be an effective initial screening parameter for finding materials for hydrogen separation. The set of materials for which diffusivity calculations were performed were substantially reduced based on initial calculations predicting H solubility. Thus, using solubility of H as a screening parameter narrowed the list of probable candidate materials that were good for membrane applications, making the screening process efficient.

Our screening methods have reduced the computational effort required to screen such a large set of materials by more than 20 orders of magnitude on an average in comparison to detailed calculation for every material without compensating on the quality of our predictions. This large reduction in the number of DFT calculations needed to calculate the H permeability can enable the computational screening of large databases of similar ordered materials.

Using solubility and diffusion activation barrier as screening parameters, we systemically eliminated materials that are unfavorable for hydrogen separation. 8 materials were identified which have predicted permeabilities higher or similar to that of pure Pd. We have also compared our results with information available from literature

about the behavior of a few intermetallics towards hydrogen and our results show agreement with previously reported data.

The constituent elements of a majority of the most promising 8 intermetallics are inexpensive in comparison to pure Pd. With the exception of Pt, Y and Hf, the remaining 8 elements (Zn, Mg, Mn, Ti, Ni, Fe, Ta, Tl) cost less than 1% of the price of Pd[26]. For implementation of these materials as membranes, experimental testing needs to be performed to examine possible issues such as phase separation and hydrogen embrittlement in these alloys. The set of suitable materials identified in this work is based on operating pressures of 1 atm H_2. We have not examined the stability of these materials and their behavior at higher hydrogen pressures where hydride formation is a possibility.

The calculations in this work assume bulk diffusion as the rate limiting step and do not consider surface effects, which can influence membrane performance under low temperature conditions [27]. Dissociation of hydrogen on the surface is assumed to be instantaneous in our models. For non-Pd membranes various coatings can be used to enhance the surface dissociation, and hence the overall membrane performance [28].

5.7 References

[1] G. Bergerhoff, I.D. Brown, Crystallographic Databases, International Union of Crystallography, Chester, 1987.

[2] D.E. Jiang, E.A. Carter, Diffusion of interstitial hydrogen into and through bcc Fe from first principles, Physical Review B, 70 (2004) 064102.

[3] P. Kamakoti, B.D. Morreale, M.V. Ciocco, B.H. Howard, R.P. Killmeyer, A.V. Cugini, D.S. Sholl, Prediction of hydrogen flux through sulfur-tolerant binary alloy membranes, Science, 307 (2005) 569-573.

[4] N. Chandrasekhar, D.S. Sholl, Quantitative Computational Screening of Pd-based Intermetallic Membranes for Hydrogen Separation, Journal of Membrane Science.

[5] S.V. Alapati, J.K. Johnson, D.S. Sholl, Large-Scale Screening of Metal Hydride Mixtures for High-Capacity Hydrogen Storage from First-Principles Calculations, The Journal of Physical Chemistry C, 112 (2008) 5258-5262.

[6] K.C. Kim, A.D. Kulkarni, J.K. Johnson, D.S. Sholl, Large-scale screening of metal hydrides for hydrogen storage from first-principles calculations based on equilibrium reaction thermodynamics, Physical Chemistry Chemical Physics, 13 (2011) 7218-7229.

[7] B.D. Morreale, B.H. Howard, O. Iyoha, R.M. Enick, C. Ling, D.S. Sholl, Experimental and computational prediction of the hydrogen transport properties of Pd_4S, Ind. Eng. Chem. Res., 46 (2007) 6313-6319.

[8] A. Kulprathipanja, G.O. Alptekin, J.L. Falconer, J.D. Way, Pd and Pd-Cu membranes: inhibition of H_2 permeation by H_2S, Journal of Membrane Science, 254 (2005) 49-62.

[9] S.Q. Hao, D.S. Sholl, Comparison of first principles calculations and experiments for hydrogen permeation through amorphous ZrNi and ZrNiNb films, Journal of Membrane Science, 350 (2010) 402-409.

[10] C. Ling, D.S. Sholl, First principles investigation of metal sulfides as membranes in hydrogen purification, Journal of Membrane Science, 329 (2009) 153-159.

[11] W. Beck, J.O.M. Bockris, M.A. Genshaw, P.K. Subramanyan, Diffusivity and Solubility of Hydrogen as a Function of Composition in Fe-Ni Alloys, Metallurgical Transactions, 2 (1971) 883-888.

[12] P. Kamakoti, D.S. Sholl, Ab initio lattice-gas modeling of interstitial hydrogen diffusion in CuPd alloys, Physical Review B, 71 (2005) 9.

[13] G. Wandahl, A.N. Christensen, Occurrence of extinction correlated with crystal-growth mode for crystals of Pd_3Ce and $MgZn_2$, Acta Chemica Scandinavica, 43 (1989) 296-297.

[14] T.B. Massalski, J. L.Murray, L.H. Bennett, H. Baker, Binary Alloy Phase Diagrams, Metals Park Ohio: American Society for Metals, Ohio, 1986.

[15] S.P. Ong, L. Wang, B. Kang, G. Ceder, Li-Fe-P-O-2 phase diagram from first principles calculations, Chemistry of Materials, 20 (2008) 1798-1807.

[16] S.V. Alapati, J. Karl Johnson, D.S. Sholl, Using first principles calculations to identify new destabilized metal hydride reactions for reversible hydrogen storage, Physical Chemistry Chemical Physics, 9 (2007) 1438-1452.

[17] A.R. Akbarzadeh, V. Ozolins, C. Wolverton, First-principles determination of multicomponent hydride phase diagrams: application to the Li-Mg-N-H system, Advanced Materials, 19 (2007) 3233-+.

[18] K.M. Nicholson, D.S. Sholl, Computationally efficient determination of hydrogen isotope effects on the thermodynamic stability of metal hydrides, Physical Review B, 86 (2012) 134113.

[19] H. Sitepu, Texture and structural refinement using neutron diffraction data from molybdite (MoO_3) and calcite ($CaCO_3$) powders and a Ni-rich $Ni_{50.7}Ti_{49.30}$ alloy, Powder Diffraction, 24 (2009) 315-326.

[20] E.E. Havinga, H. Damsma, P. Hokkeling, Compounds and pseudo-binary alloys with the $CuAl_2$(C16)-type structure I. Preparation and X-ray results, Journal of the Less Common Metals, 27 (1972) 169-186.

[21] R.M. Van Essen, K.H.J. Buschow, Hydrogen absorption in various zirconium- and hafnium-based intermetallic compounds, Journal of the Less Common Metals, 64 (1979) 277-284.

[22] B.D. Morreale, M.V. Ciocco, R.M. Enick, B.I. Morsi, B.H. Howard, A.V. Cugini, K.S. Rothenberger, The permeability of hydrogen in bulk palladium at elevated temperatures and pressures, Journal of Membrane Science, 212 (2003) 87-97.

[23] G.L.W. Hart, S. Curtarolo, T.B. Massalski, O. Levy, Comprehensive Search for New Phases and Compounds in Binary Alloy Systems Based on Platinum-Group Metals, Using a Computational First-Principles Approach, Physical Review X, 3 (2013) 041035.

[24] M. Jahnátek, O. Levy, G.L.W. Hart, L.J. Nelson, R.V. Chepulskii, J. Xue, S. Curtarolo, Ordered phases in ruthenium binary alloys from high-throughput first-principles calculations, Physical Review B, 84 (2011) 214110.

[25] S. Hao, D.S. Sholl, Rapid prediction of hydrogen permeation through amorphous metal membranes: an efficient computational screening approach, Energy & Environmental Science, 6 (2013) 232-240.

[26] Barrientos, M., & Sora, C. (2013). Indexmundi. Retrieved February 5, 2014, from www.indexmundi.com

[27] C. Ling, D.S. Sholl, Using first-principles calculations to predict surface resistances to H_2 transport through metal alloy membranes, Journal of Membrane Science, 303 (2007) 162-172.

[28] S. Hao, D.S. Sholl, First-Principles Models of Facilitating H_2 Transport through Metal Films Using Spillover, The Journal of Physical Chemistry C, 117 (2012) 1217-1223.

PART 2: Pd-Au ALLOYS

CHAPTER 6

INTRODUCTION

Hydrogen is an important energy carrier for a clean and sustainable future. H_2 is primarily produced from the steam reforming of fossil fuels resulting in the production of hydrogen with a mixture of other gases [1, 2]. To generate pure H_2, the separation of hydrogen from this mixture of gases is necessary [3]. Membrane separations have significant advantages over other approaches to hydrogen purification as discussed in the previous chapters.

Dense metal membranes are well-suited for use at high temperatures since they have perfect selectivity for hydrogen and good thermal stabilities at elevated temperatures [4]. First-principles based models of interstitial H in metals have been used to predict the performance of dense metal membranes for a wide range of substitutionally disordered alloys,[5-7] amorphous metal alloys[8, 9] and stoichiometric intermetallics[10]. In Part A of this thesis, detailed computational models to predict hydrogen permeability through intermetallics were described. All of these prior calculations, however, have assumed that the ordering of the metal is unaffected by the presence of interstitial H.

Hydrogen is known to induce changes in many Pd-based alloys. Pd-Mn, Pd-Ni and Pd-Rh have shown lattice-ordering tendencies in the presence of H. In the presence of H, the transition from ordered structures to disordered alloys is also faster, indicating that dissolved H assists metal atom rearrangement [11-13].

H induced lattice rearrangement in Pd-Au alloys was experimentally observed in the work of Lee et al. [14]. In that work solubility was used as a measure of lattice rearrangement in $Pd_{81}Au_{19}$, since H is sensitive to metal atom changes in the vicinity of an interstitial site. Lee et al. observed that hydrogen heat treatment (HHT) i.e. prolonged exposure to H_2 at elevated temperatures, causes ordering in Pd-Au alloys, which increases the solubility of H in the alloy.

Pd-Au alloys form a continuous series of fcc solid solutions with no long-range order except at two stoichiometric compositions, $PdAu_3$ and Pd_3Au [15-17]. These two ordered phases are only thermodynamically stable at temperatures less than 400 K[15, 17]. At other compositions, Pd-Au alloys are known to exhibit short-range order (SRO). The presence of SRO in Pd-Au alloys has been experimentally observed in multiple studies [14, 18]. Negative (exothermic) enthalpies of mixing indicate a tendency for ordering in Pd-Au system [14, 19]. Lee et al. showed that hydrogen heat treatment of PdAu can lead to significant changes in H solubility [14]. No information is currently available, however, on the role of H-induced SRO on diffusion of H in PdAu alloys or H permeance through these alloys.

In the following chapters, we introduce methods to predict the appearance of short-range order (SRO) in PdAu alloys using first-principles based methods, and examine the impact of this H-induced SRO on permeance of H through PdAu membranes. Our interest in these alloys is encouraged by the fact that PdAu alloys have been found to have favorable H permeabilities for H separation [7, 20-23]. The solubility of $Pd_{96}Au_4$ was predicted by first-principles methods to be higher than pure Pd at 1 atm H_2 and temperatures from 400-1000 K [7]. Using similar methods, Sonwane et al. predicted a maximum in permeability for PdAu membranes with composition $Pd_{88}Au_{12}$, in qualitative agreement with experimental results [24].

In this work, we computationally simulate lattice rearrangement induced by interstitial H in two PdAu alloys at various H_2 pressures and temperatures. Two PdAu alloys, $Pd_{96}Au_4$ and $Pd_{85}Au_{15}$, were studied in this work. Throughout our work, alloy compositions are defined in atomic % (not weight %). $Pd_{96}Au_4$ was chosen since previous studies on this alloy reported favorable permeabilities of H [7]. $Pd_{85}Au_{15}$ was chosen since this composition is close to the average composition of Pd-Au alloys studied earlier for H induced lattice rearrangement in the surface and bulk [14, 25].

In Chapter 7 we describe the methods developed to study H induced lattice rearrangement using a combination of cluster expansion, Monte Carlo and grand canonical Monte Carlo (GCMC) methods. In Chapter 8 the results obtained for the SRO and permeability calculations for both $Pd_{96}Au_4$ and $Pd_{85}Au_{15}$ alloys are described.

6.1 References

[1] N.W. Ockwig, T.M. Nenoff, Membranes for Hydrogen Separation, Chemical Reviews, 107 (2007) 4078-4110.

[2] T.M. Nenoff, R.J. Spontak, C.M. Aberg, Membranes for hydrogen purification: An important step toward a hydrogen-based economy, MRS Bull., 31 (2006) 735-741.

[3] B.C.H. Steele, A. Heinzel, Materials for fuel-cell technologies, Nature, 414 (2001) 345-352.

[4] D.S. Sholl, Y.H. Ma, Dense metal membranes for the production of high-purity hydrogen, MRS Bull., 31 (2006) 770-773.

[5] P. Kamakoti, B.D. Morreale, M.V. Ciocco, B.H. Howard, R.P. Killmeyer, A.V. Cugini, D.S. Sholl, Prediction of hydrogen flux through sulfur-tolerant binary alloy membranes, Science, 307 (2005) 569-573.

[6] S.G. Kang, K.E. Coulter, S.K. Gade, J.D. Way, D.S. Sholl, Identifying Metal Alloys with High Hydrogen Permeability Using High Throughput Theory and Experimental Testing, The Journal of Physical Chemistry Letters, 2 (2011) 3040-3044.

[7] L. Semidey-Flecha, D.S. Sholl, Combining density functional theory and cluster expansion methods to predict H_2 permeance through Pd-based binary alloy membranes, J. Chem. Phys., 128 (2008).

[8] S. Hao, D.S. Sholl, Rapid prediction of hydrogen permeation through amorphous metal membranes: an efficient computational screening approach, Energy & Environmental Science, 6 (2013) 232-240.

[9] S.Q. Hao, D.S. Sholl, Comparison of first principles calculations and experiments for hydrogen permeation through amorphous ZrNi and ZrNiNb films, Journal of Membrane Science, 350 (2010) 402-409.

[10] N. Chandrasekhar, D.S. Sholl, Quantitative computational screening of Pd-based intermetallic membranes for hydrogen separation, Journal of Membrane Science, 453 (2014) 516-524.

[11] H. Noh, J.D. Clewley, T.B. Flanagan, A.P. Craft, Hydrogen-induced phase separation in Pd-Rh alloys, Journal of Alloys and Compounds, 240 (1996) 235-248.

[12] T.B. Flanagan, H. Noh, J.D. Clewley, J.G. Barker, Evidence from SANS and H_2 solubilities for H-enhanced metal atom diffusion in Pd-Ni alloys, Scripta Materialia, 39 (1998) 1607-1611.

[13] T.B. Flanagan, C.N. Park, Hydrogen-induced rearrangements in Pd-rich alloys, Journal of Alloys and Compounds, 293–295 (1999) 161-168.

[14] S.M. Lee, H. Noh, B.F. Ted, S. Luo, Hydrogen-induced lattice rearrangement of a $Pd_{0.81}Au_{0.19}$ alloy, Journal of Physics: Condensed Matter, 19 (2007) 326222.

[15] S.V. Barabash, V. Blum, S. Müller, A. Zunger, Prediction of unusual stable ordered structures of Au-Pd alloys via a first-principles cluster expansion, Physical Review B, 74 (2006) 035108.

[16] H. Okamoto, T.B. Massalski, The Au−Pd (Gold-Palladium) system, Bulletin of Alloy Phase Diagrams, 6 (1985) 229-235.

[17] M.H.F. Sluiter, C. Colinet, A. Pasturel, *Ab initio* calculation of the phase stability in Au-Pd and Ag-Pt alloys, Physical Review B, 73 (2006) 174204.

[18] W.D. Copeland, M.E. Nicholson, X-ray evidence of short range order in Au-Pd system, Acta Metallurgica, 12 (1964) 321-322.

[19] J.B. Darby Jr, The relative heats of formation of solid gold-palladium alloys, Acta Metallurgica, 14 (1966) 265-270.

[20] S. Maestas, T.B. Flanagan, Diffusion of hydrogen in gold-palladium alloys, The Journal of Physical Chemistry, 77 (1973) 850-854.

[21] C.G. Sonwane, J. Wilcox, Y.H. Ma, Achieving optimum hydrogen permeability in PdAg and PdAu alloys, The Journal of Chemical Physics, 125 (2006) 184714.

[22] T.B. Flanagan, D. Wang, Hydrogen Permeation through fcc Pd-Au Alloy Membranes, J. Phys. Chem. C, 115 (2011) 11618-11623.

[23] K.E. Coulter, J.D. Way, S.K. Gade, S. Chaudhari, G.O. Alptekin, S.J. DeVoss, S.N. Paglieri, B. Pledger, Sulfur tolerant PdAu and PdAuPt alloy hydrogen separation membranes, Journal of Membrane Science, 405–406 (2012) 11-19.

[24] V. Gryaznov, Metal containing membranes for the production of ultrapure hydrogen and the recovery of hydrogen isotopes, Separation and Purification Methods, 29 (2000) 171-187.

[25] Y. Kawasaki, S. Ino, S. Ogawa, Electron Diffraction Study on the Superlattice Formation in the Gold-Palladium Alloy System, Journal of the Physical Society of Japan, 30 (1971) 1758-1759.

CHAPTER 7

COMPUTATIONAL METHODS

7.1 Warren Cowley Parameter

A short-range order (SRO) parameter was used to quantify the extent of H induced lattice rearrangement in $Pd_{96}Au_4$ and $Pd_{85}Au_{15}$ alloys. SRO defines the extent of disorder in a real alloy from an ideal random alloy. Most solid solutions or substitutionally disordered alloys show some short-range order[1, 2]. SRO can be quantified using the Warren Cowley parameter:

$$a_j = 1 - \frac{P_j^{Au(Pd)}}{x_{Pd}} \qquad (2)$$

where P_j is the conditional probability that given an Au atom at the origin there is a Pd atom at the j^{th} neighbor distance and x_{Pd} is the atomic fraction of Pd in the alloy. The sign of α_j indicates whether atoms in a given distance j prefer Pd-Au ordering ($\alpha_j < 0$) or clustering of like atoms ($\alpha_j > 0$). This parameter is normalized such that $-1 \leq \alpha_j \leq 1$ and $\alpha=0$ represents a substitutionally random alloy. In this work, the extent of ordering was determined with respect to the nearest neighbor shell only (j=1).

To study the effect of ordering on the solubility and diffusivity of H, fcc alloy structures with predetermined α were generated using a Reverse Monte Carlo procedure [3]. Initially, a completely random fcc alloy was generated with α very close to 0. Moves that switched atom identities were then generated randomly. Moves that brought the α of the current structure closer to the target α were accepted with a probability of 1. Unfavorable moves were accepted with a probability of $\exp(-b|a_c - a_f|)$ where β was adjusted from 0.005 to 0.009 for different target values of α. Here, α_c represents the SRO of the current structure and α_f represent the target α. The maximum ordering that one can achieve in $Pd_{96}Au_4$ ($Pd_{85}Au_{15}$) has α = -0.04 (-0.08).

7.2 Cluster Expansion for Pd-Au alloy energies

Substitutionally disordered alloys can exhibit a very large number of possible configurations. Cluster expansion (CE) methods are a powerful tool to predict properties of disordered alloys [4-7]. Sluiter et al. developed a CE for the calculation of ground state energies of Pd-Au alloys on the fcc lattice [8]. Sluiter et al.'s 23 cluster CE was used to predict the enthalpy of the different alloy configurations and gave good agreement with values calculated using Density Functional Theory (DFT) methods.

To calculate the equilibrium SRO for each alloy composition as a function of temperature, NVT-Monte Carlo was performed using the energy defined by Sluiter's cluster expansion. Simulations were performed on a system of 4000 metal atoms with periodic boundary conditions. A MC step is defined as an attempt to swap two metal atoms. Unless otherwise stated, equilibrium structures were taken after performing 10^7 MC steps.

7.3 H solubility, diffusivity & permeability at low H_2 pressures

For ab-initio prediction of the solubility of interstitial H in an alloy, the binding energy and zero-point energies (ZPE) of H can be calculated using DFT [3, 9]. However, in disordered PdAu alloys, a plethora of possible binding site configurations exist, making these calculations a challenge in these materials.

A CE for predicting the binding energies and ZPE of H in $Pd_{96}Au_4$ fcc alloy was developed by Semidey-Flecha and Sholl[7]. The details of the cluster expansion developed for $Pd_{96}Au_4$ is described in Reference 7. A limitation of the CE parameters developed by Semidey-Flecha et al. is that it only applies to the fcc-$Pd_{96}Au_4$ alloy. To allow examination of H properties in different alloy compositions such as $Pd_{85}Au_{15}$, a new CE for interstitial H was developed in this work. It is important to note that the CEs for interstitial H were developed primarily with calculations that assumed the H was present in substitutionally disordered alloys at low concentrations. We use these CEs to

describe alloys with SRO, assuming that the CE parameters are transferable to this situation. The parameters for the cluster expansion developed to predict the hydrogen binding energies in fcc $Pd_{85}Au_{15}$ were derived in a similar manner as the $Pd_{96}Au_4$ alloy. Further details of the CE model developed for $Pd_{85}Au_{15}$ are given in Appendix B.

In metals with a dilute loading of hydrogen, the net solubility of hydrogen in a metal can be accurately calculated using Sieverts' law [7, 10]. Our calculations of H solubility, diffusivity and permeability in both PdAu alloys at low H_2 pressures follow the methodology developed by Semidey-Flecha and Sholl[7]. The solubility of H was calculated using a 4000 atom cell with periodic boundary conditions. Once the binding energies of interstitial H in the different binding sites are calculated using the CE for interstitial H, the Sieverts' constant can be computed using the method of Kamakoti and Sholl[3]. At low pressures, the Sieverts' constant is related to the H loading per metal atom, θ (H/M), by

$$q = K_s\sqrt{P_{H_2}} \qquad (3)$$

where P_{H_2} is the partial pressure of hydrogen and K_s is the Sieverts' constant. The maximum pressure that can be considered for the H solubility to remain in the dilute loading region for both alloys is 0.01 atm. The low hydrogen pressure calculations were performed at this pressure for temperatures ranging from 600-1000 K.

At elevated temperatures, H diffuses in fcc metals through discrete hops between adjacent octahedral (O) and tetrahedral (T) sites [11, 12]. To determine the diffusivity of hydrogen, the energy of the transition states for diffusion must be known. The transition state energies were calculated using the CE developed from a large set of DFT calculations for each alloy composition [7].

Kinetic Monte Carlo (KMC) simulations were used to compute the self-diffusivity of H in each of the alloys. At dilute loading the diffusivity of H can be accurately described by the self-diffusivity [13]. The KMC algorithm developed by Kamakoti and Sholl[3]

was used in this work for diffusivity calculations in both the alloys. Interactions between H atoms in the system were neglected since our calculations are in the dilute limit. The permeability of H through a metal membrane is the product of the solubility and the diffusivity [10]. Here, as in previous modeling work, we assume that bulk diffusion and not surface effects is the rate-limiting step in the permeation of hydrogen through the membrane [14, 15]. Once the solubility and diffusivity values of H at low pressures were obtained, the permeability of H can be determined [3, 7].

7.4 Hydrogen properties at high H pressures

The previous sections describe the methods used to calculate H permeability at low H_2 pressures. At higher H_2 pressures, the net solubility of H (H/M) in PdAu alloys can be calculated as a function of temperature and pressure using grand canonical Monte Carlo (GCMC) simulations. In these calculations, the chemical potential of the H_2 molecules in the gas phase is equated to the chemical potential of atomic hydrogen in the interstitial sites. The gas phase molecular H_2 is treated as an ideal gas [16, 17]. A maximum H_2 pressure of 1000 atm was considered in our calculations. This choice was motivated by earlier experiments in which PdAu alloys were subjected to HHT up to pressures of 986.92 atm (100 MPa)[18]. The cluster expansion method described above was used to define the energies and ZPE of H in interstitial sites and transition states.

Lattice expansion due to non-negligible concentrations of H atoms in the system was not considered in our calculations. To determine whether this approach is reasonable, we performed calculations to quantify the effects of lattice expansion on H loading at the maximum loading obtained using GCMC. Specifically, we examined the $Pd_{96}Au_4$ alloy at 600 K and 1000 atm of H_2, where the loading predicted without including lattice expansion was 0.27 (H/M) for an alloy with α=-0.04. To calculate the lattice expansion due to H at these loadings, the final structure obtained after GCMC was extracted. The 4000 metal atoms and 1080 H atoms in the final structure were then divided into domains containing 100 metal atoms and the necessary H atoms for plane wave DFT

calculations using periodic boundary conditions. Among the 40 periodic cells, 3 had H atoms near the boundaries of the cell that resulted in H-H distances < 2.1 Å, violating the Westlake criteria [19]. These configurations were not included in the averaging of the lattice expansion. A full geometry relaxation DFT calculation was performed for each of the remaining 37 cells and the average lattice expansion due to H in each of the 37 cells was averaged.

These DFT calculations were performed using the Vienna *ab initio* simulation package (VASP) with the PW91 generalized gradient approximation functional using the projector augmented wave method [20-26]. A cut-off energy value of 250 eV was used and geometries were relaxed using a conjugate gradient method until the forces on all atoms were less than 0.03 eV/A. Geometric relaxation to obtain the lattice expansion was performed using a 4×4×4 k-point mesh to sample the reciprocal space and relaxing the lattice constants and all internal coordinates.

The increase in the lattice constant averaged across the 37 DFT calculations was 4% in comparison to the bulk metal in the absence of H. By comparing the energy of this 127-atom sample after relaxation with DFT to the energy predicted by the GCMC calculation, the change in binding energy of each H atom due to the alloy's expansion was estimated. For these systems, the binding energy averaged across the different sets of atoms became more favorable by 0.023 eV. Using these increased binding energies added uniformly to every interstitial site, we performed GCMC on the entire 4000 metal atom system to estimate the net hydrogen loading at 1000 atm of H and 600 K after including lattice expansion effects. The loading of H after consideration of lattice expansion was 0.287, which was only marginally larger than the result before including these effects, 0.27. Similar calculations were performed at 900 K and 1000 K at 1000 atm H_2 at α =-0.04. The change in binding energy averaged across the system at 900 K (1000 K) was 0.003 eV (0.001 eV). The increase in loading due to lattice expansion at 900 K was even smaller than that observed at 600 K, with no increase observed at 1000

K. This analysis indicates that our assumption of neglecting lattice expansion effects in the remainder of our calculations is reasonable.

At high hydrogen loadings, the self-diffusivity, which describes the motion of individual tracer particles, cannot completely describe the hydrogen diffusion. The transport diffusion coefficient described in Fick's law is not equal to the self-diffusivity except at dilute H loadings, and it is the transport diffusion coefficient that is needed to describe net mass transfer [13, 17]. The transport diffusivity can be rewritten as a product of the corrected diffusivity (single component Maxwell-Stefan diffusivity) and the thermodynamic correction factor [27-29]. At higher H loadings, the corrected diffusivity was calculated using KMC. The method used to calculate the corrected diffusivity in this work followed the methods developed by Hao and Sholl [17]. In the KMC simulations, H-H interactions were included using the Westlake criterion i.e. no hops that place a H atom within 2.1 Å of another H atom were accepted, although the time was incremented as it would be for the same event occurring without H-H interactions. The Westlake criterion was also used for initial placement of H atoms in the KMC simulation cell [17]. In the KMC simulations, the effect of lattice expansion due to H was not considered. This is reasonable because if the binding energy of H in all sites is modified by the same value, the local hopping rates are unaffected.

Corrected diffusivities were obtained by averaging over 30 independent KMC simulations at every state point (temperature and H concentration) and structure at the given conditions defined by α. The thermodynamic correction factors were calculated directly from GCMC simulations used to determine solubility at high H pressures [17]. The thermodynamic correction factor approaches unity at dilute loadings and was calculated at the same conditions (pressure, temperature, α) used to compute the H loadings (H/M) for the KMC simulations. Once the transport diffusivity and solubility were computed at high H pressures, the permeability of the alloy was predicted using the method described previously.

7.5 H induced lattice rearrangement in Pd-Au alloys

The cluster expansions defined above were combined to study lattice rearrangement using the SRO parameter in Pd-Au alloys at different H pressures and temperatures. An fcc structure was generated with each atom being randomly defined as Pd or Au to reach the desired composition (α =0) and the hydrogen solubility was calculated at a particular temperature and fixed hydrogen pressure (both low and high H_2 pressures). Hydrogen was initially inserted with a distribution adjusted for operating pressure in the various interstitial sites in the alloy using

$$probability = \frac{\exp(\frac{-E_i}{k_b T})}{\sum_i \exp(\frac{-E_i}{k_b T})} \times \sqrt{P_{H_2}} \times K_{s_i} \qquad (4)$$

where E_i is the binding energy of site i, k_b is the Boltzmann constant, P_{H_2} is the pressure of hydrogen and T is the temperature and K_{s_i} is the Sieverts' constant calculated using E_i.

The positions of the H atoms were then kept fixed and Metropolis NVT-Monte Carlo was performed on the metal atoms alone to sample the most favorable alloy configurations. The system containing metal atoms and interstitial H was equilibrated using the total energy of the system including the enthalpy of formation and the binding energies of H in the alloy. At each NVT-MC step, trial moves involved two dissimilar metal atoms that were randomly swapped. Trial moves were accepted or rejected using a standard Metropolis approach [3, 30].

After 10^7 steps of NVT Monte Carlo were performed, the metal atoms were found to be in equilibrium with the hydrogen present in the material. The H solubility was computed in the new structure at a given pressure and temperature. This solubility differs from that of the initial structure because the local composition of the hydrogen interstitial sites has changed. The existing H atoms were removed and new H atoms

were inserted using the procedure described above after recalculating the binding energy of H in each site. This process of performing NVT-MC of metal atoms and reinsertion of new H atoms was repeated until the solubility computed before and after the metal atom rearrangement was equal within a small tolerance.

The SRO parameter of the final system was calculated to determine the extent of ordering/clustering due to the interstitial hydrogen. In the next chapter we first describe the SRO of alloy structures in equilibrium at different temperatures in the absence of interstitial H, followed by the solubility and diffusivity of H through the alloys at different values of α.

7.6 References

[1] M. Stefan, Bulk and surface ordering phenomena in binary metal alloys, Journal of Physics: Condensed Matter, 15 (2003) R1429.

[2] G.E. Ice, C.J. Sparks, Modern Resonant X-Ray Studies of Alloys: Local Order and Displacements, Annu. Rev. Mater. Sci., 29 (1999) 25-52.

[3] P. Kamakoti, D.S. Sholl, Ab initio lattice-gas modeling of interstitial hydrogen diffusion in CuPd alloys, Physical Review B, 71 (2005) 9.

[4] R. Drautz, R. Singer, M. Fähnle, Cluster expansion technique: An efficient tool to search for ground-state configurations of adatoms on plane surfaces, Physical Review B, 67 (2003) 035418.

[5] V. Blum, A. Zunger, Mixed-basis cluster expansion for thermodynamics of bcc alloys, Physical Review B, 70 (2004) 155108.

[6] G.L.W. Hart, V. Blum, M.J. Walorski, A. Zunger, Evolutionary approach for determining first-principles hamiltonians, Nature Materials, 4 (2005) 391-394.

[7] L. Semidey-Flecha, D.S. Sholl, Combining density functional theory and cluster expansion methods to predict H_2 permeance through Pd-based binary alloy membranes, J. Chem. Phys., 128 (2008).

[8] M.H.F. Sluiter, C. Colinet, A. Pasturel, *Ab initio* calculation of the phase stability in Au-Pd and Ag-Pt alloys, Physical Review B, 73 (2006) 174204.

[9] K. M.Nicholson, N. Chandrasekhar, D.S. Sholl, Powered by DFT: Screening Methods that Accelerate Materials Development for Hydrogen in Metals Applications, Accounts of Chemical Research, (2014) In Print.

[10] P. Kamakoti, B.D. Morreale, M.V. Ciocco, B.H. Howard, R.P. Killmeyer, A.V. Cugini, D.S. Sholl, Prediction of hydrogen flux through sulfur-tolerant binary alloy membranes, Science, 307 (2005) 569-573.

[11] H. Barlag, L. Opara, H. Züchner, Hydrogen diffusion in palladium based f.c.c. alloys, Journal of Alloys and Compounds, 330–332 (2002) 434-437.

[12] S. Fujita, A. Garcia, Theory of hydrogen diffusion in metals. Quantum isotope effects, Journal of Physics and Chemistry of Solids, 52 (1991) 351-355.

[13] D.S. Sholl, Understanding Macroscopic Diffusion of Adsorbed Molecules in Crystalline Nanoporous Materials via Atomistic Simulations, Accounts of Chemical Research, 39 (2006) 403-411.

[14] S. Hao, R.B. Rankin, J.K. Johnson, D.S. Sholl, Surface reactions of AsH_3, H_2Se, and H_2S on the Zn_2TiO_4(010) surface, Surface Science, 605 (2011) 818-823.

[15] C. Ling, D.S. Sholl, Using first-principles calculations to predict surface resistances to H_2 transport through metal alloy membranes, Journal of Membrane Science, 303 (2007) 162-172.

[16] S. Hao, D.S. Sholl, Comparison of first principles calculations and experiments for hydrogen permeation through amorphous ZrNi and ZrNiNb films, Journal of Membrane Science, 350 (2010) 402-409.

[17] S.Q. Hao, D.S. Sholl, Comparison of first principles calculations and experiments for hydrogen permeation through amorphous ZrNi and ZrNiNb films, Journal of Membrane Science, 350 (2010) 402-409.

[18] S.M. Lee, H. Noh, B.F. Ted, S. Luo, Hydrogen-induced lattice rearrangement of a $Pd_{0.81}Au_{0.19}$ alloy, Journal of Physics: Condensed Matter, 19 (2007) 326222.

[19] S. Hao, D.S. Sholl, Computational prediction of durable amorphous metal membranes for H2 purification, Journal of Membrane Science, 381 (2011) 192-196.

[20] G. Kresse, J. Hafner, Ab initio molecular-dynamics simulation of the liquid-metal–amorphous-semiconductor transition in germanium, Physical Review B, 49 (1994) 14251-14269.

[21] G. Kresse, J. Furthmüller, Efficiency of ab-initio total energy calculations for metals and semiconductors using a plane-wave basis set, Computational Materials Science, 6 (1996) 15-50.

[22] G. Kresse, J. Furthmüller, Efficient iterative schemes for ab initio total-energy calculations using a plane-wave basis set, Physical Review B, 54 (1996) 11169-11186.

[23] G. Kresse, D. Joubert, From ultrasoft pseudopotentials to the projector augmented-wave method, Physical Review B, 59 (1999) 1758-1775.

[24] P.E. Blöchl, Projector augmented-wave method, Physical Review B, 50 (1994) 17953-17979.

[25] J.P. Perdew, J.A. Chevary, S.H. Vosko, K.A. Jackson, M.R. Pederson, D.J. Singh, C. Fiolhais, Atoms, molecules, solids, and surfaces: Applications of the generalized gradient approximation for exchange and correlation, Physical Review B, 46 (1992) 6671-6687.

[26] J.P. Perdew, J.A. Chevary, S.H. Vosko, K.A. Jackson, M.R. Pederson, D.J. Singh, C. Fiolhais, Erratum: Atoms, molecules, solids, and surfaces: Applications of the generalized gradient approximation for exchange and correlation, Physical Review B, 48 (1993) 4978-4978.

[27] R. Krishna, J.M. van Baten, Diffusion of Alkane Mixtures in Zeolites: Validating the Maxwell−Stefan Formulation Using MD Simulations, The Journal of Physical Chemistry B, 109 (2005) 6386-6396.

[28] A.I. Skoulidas, D.S. Sholl, R. Krishna, Correlation Effects in Diffusion of CH_4/CF_4 Mixtures in MFI Zeolite. A Study Linking MD Simulations with the Maxwell−Stefan Formulation, Langmuir, 19 (2003) 7977-7988.

[29] C. Uebing, R. Gomer, A Monte Carlo study of surface diffusion coefficients in the presence of adsorbate–adsorbate interactions. I. Repulsive interactions, The Journal of Chemical Physics, 95 (1991) 7626-7635.

[30] K.A. Fichthorn, W.H. Weinberg, Theoretical foundations of dynamical Monte Carlo simulations, The Journal of Chemical Physics, 95 (1991) 1090-1096.

CHAPTER 8

RESULTS

In chapters 6 and 7, we described the methods used to study H induced lattice rearrangement in $Pd_{96}Au_4$ and $Pd_{85}Au_{15}$. In this chapter we first discuss the SRO observed in these alloys after hydrogen heat treatment (HHT) under various hydrogen pressures and temperatures. We then study the HHT induced effects on the permeability of H comparing the permeability of HHT alloys with pure alloys (non- HHT). All studies were performed using the methods described in Chapter 7.

8.1 Equilibrium structures at different temperatures

Figure 8.1 shows the equilibrium SRO and energy/atom as a function of the temperature for $Pd_{96}Au_4$ and $Pd_{85}Au_{15}$ in the absence of hydrogen. At higher temperatures, the energy of each alloy increases because of compensating entropic effects. As temperature increases, there is a small increase in SRO in each alloy, indicating that clustering is favored at higher temperatures. Over the whole temperature range examined, however, the extent of SRO is small.

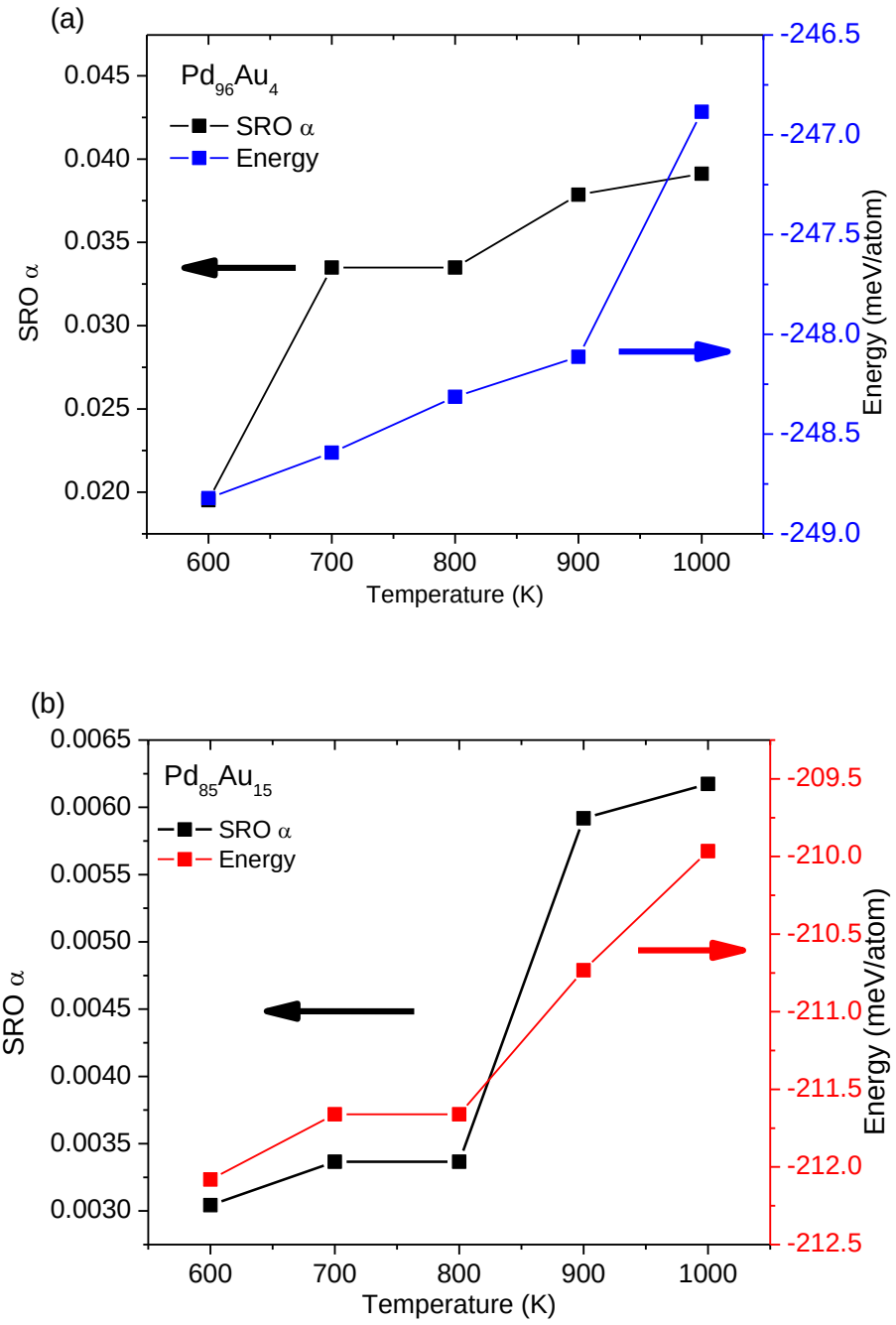

Figure 8.6: The equilibrium SRO (open symbols) and energy in meV/atom (filled symbols) of (a) $Pd_{96}Au_4$ and (b) $Pd_{85}Au_{15}$ as a function of temperature.

8.2 H solubility and diffusivity as a function of SRO at different temperatures

To study the effect of SRO on the solubility and diffusivity of H in Pd-Au alloys, structures with specified values of α were generated using the Reverse Monte Carlo method described in Chapter 7. Figure 7.2 shows the H solubility in $Pd_{96}Au_4$ and $Pd_{85}Au_{15}$ as a function of α. As observed in this figure, the solubility is sensitive to the SRO of the atoms in the alloy. The H solubility (θ) at maximum ordering in $Pd_{96}Au_4$ (α = -0.04) is 2.2 times the value at maximum clustering (α=0.5) at 600 K and 1 atm H_2.

For both $Pd_{96}Au_4$ and $Pd_{85}Au_{15}$, as α increases the solubility of the alloy moves closer to the solubility of pure Pd at the lattice constant of the alloy (3.97 Å and 4.02 Å respectively). This is because when similar atoms cluster together, there are regions of the alloy that are composed of pure Pd. The increased lattice constant due to the presence of Au atoms results in more favorable binding energy resulting in a higher solubility than pure bulk Pd, which has a lattice constant of 3.96 Å when treated with the same DFT calculations used to describe the alloys in this work [1].

Figure 8.2 also shows the diffusivity of H in $Pd_{96}Au_4$ and $Pd_{85}Au_{15}$ computed using the methods described above at different SRO. The diffusivity is calculated using the average loading of H calculated previously for the alloys in Fig. 8.2(a) and (b). The diffusivities obtained using the average H loading and at infinite dilution were very similar. The increase in lattice constant of both the alloys in comparison to pure Pd due to the larger Au atoms results in a more favorable binding site for H atoms and subsequently a higher activation barrier for diffusion. This causes the diffusivity of the alloy to be lower than that of pure Pd. However, as clustering occurs and regions of bulk-Pd are formed, the diffusivity of the alloy moves towards that of pure Pd. At maximum ordering (α=-0.04) in $Pd_{96}Au_4$, the diffusion activation energy barrier is 0.23 eV and at maximum clustering (α=0.5) the diffusion activation barrier decreases slightly to 0.21 eV due to formation of regions of bulk-like Pd.

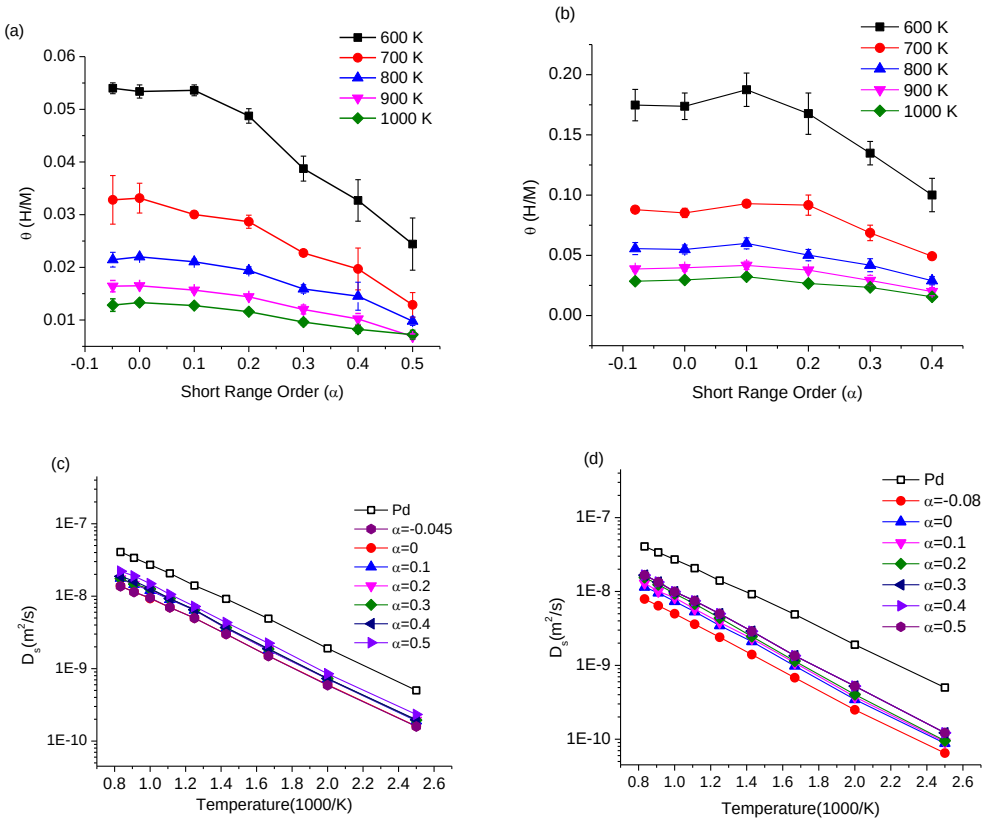

Figure 8.7: H loading (H/M) as a function of the SRO parameter for (a) $Pd_{96}Au_4$ and the (b) $Pd_{85}Au_{15}$ and diffusivity as a function of SRO parameter for (c) $Pd_{96}Au_4$ and (d) $Pd85Au_{15}$. The values shown in (a) and (b) are the average of 10 independent simulations at each temperature and value of α. The diffusivity of pure Pd is shown using open black squares for comparison of the diffusivity of H in the alloys.

In $Pd_{85}Au_{15}$, similar effects of solubility are observed as for $Pd_{96}Au_4$. As clustering occurs, H solubility decreases. The solubility of $Pd_{85}Au_{15}$ is greater than $Pd_{96}Au_4$; the increased lattice constant of the former alloy results in higher solubility despite the increase in the concentration of Au atoms [2].

The higher amount of Au in $Pd_{85}Au_{15}$ in comparison to $Pd_{96}Au_4$ results in lower diffusivity even at maximum clustering (Fig 8.2(d)) due to the more favorable binding energy of H in $Pd_{85}Au_{15}$. The diffusivity of $Pd_{85}Au_{15}$ is also lower than that of pure Pd for all values of α. At maximum ordering for $Pd_{85}Au_{15}$ (α=-0.08) the activation barrier for diffusion of H across the alloy is 0.25 eV. At maximum clustering (α=0.5) the barrier decreases slightly to 0.24 eV. Similar observations of the formation of Pd-clusters that

showed highly favorable H diffusivity in Pd-Cu alloys have been observed previously in literature [3].

8.3 Change in solubility as a function of SRO at low and high H_2 pressures

In the previous section, we studied the change in solubility of H in the alloys as a function of the SRO parameter. In those calculations, however, the alloy structures of $Pd_{96}Au_4$ and $Pd_{85}Au_{15}$ were generated at fixed α values. Under experimental conditions, in contrast, changes in the SRO of the alloy structures occur due to hydrogen dissolution. We calculate these changes in SRO in this section. The rearrangement of metal atoms due to the presence of H was computed using changes in the SRO parameter following the combined Monte Carlo procedure outlined in the previous chapter.

8.3.1 Low H pressures

At low pressure (0.01 atm H_2) the extent of atom rearrangement is, unsurprisingly, very small. The change in SRO parameter was plotted as a function of the number of hydrogen insertion steps. It was found that after 12 H insertion cycles, the system equilibrated at all temperatures (see Figure C.1 in Appendix C). Consistent with the results above, these calculations indicate that as SRO decreases the solubility increases. It must be emphasized, however, that the changes observed in SRO due to interstitial H at low pressures are marginal because of the very small number of H atoms present in the system. To observe if significant lattice rearrangement due to interstitial H can occur, the system was studied under higher H_2 pressures.

8.3.2 High H pressures

In the high H_2 pressure cases, the maximum pressure considered was 1000 atm. The SRO and the H loading are plotted as a function of the pressure in Figure 3 at 600 K, 800 K and 1000 K. The plots at 700 K and 900 K for $Pd_{96}Au_4$ and $Pd_{85}Au_{15}$ are in

Figure C.2 and C.3 in Appendix C. Each point in the plot represents the equilibrium loading and SRO for the alloy at the particular conditions. The equilibrium values were obtained by performing the H insertion steps 12 times at each pressure and temperature.

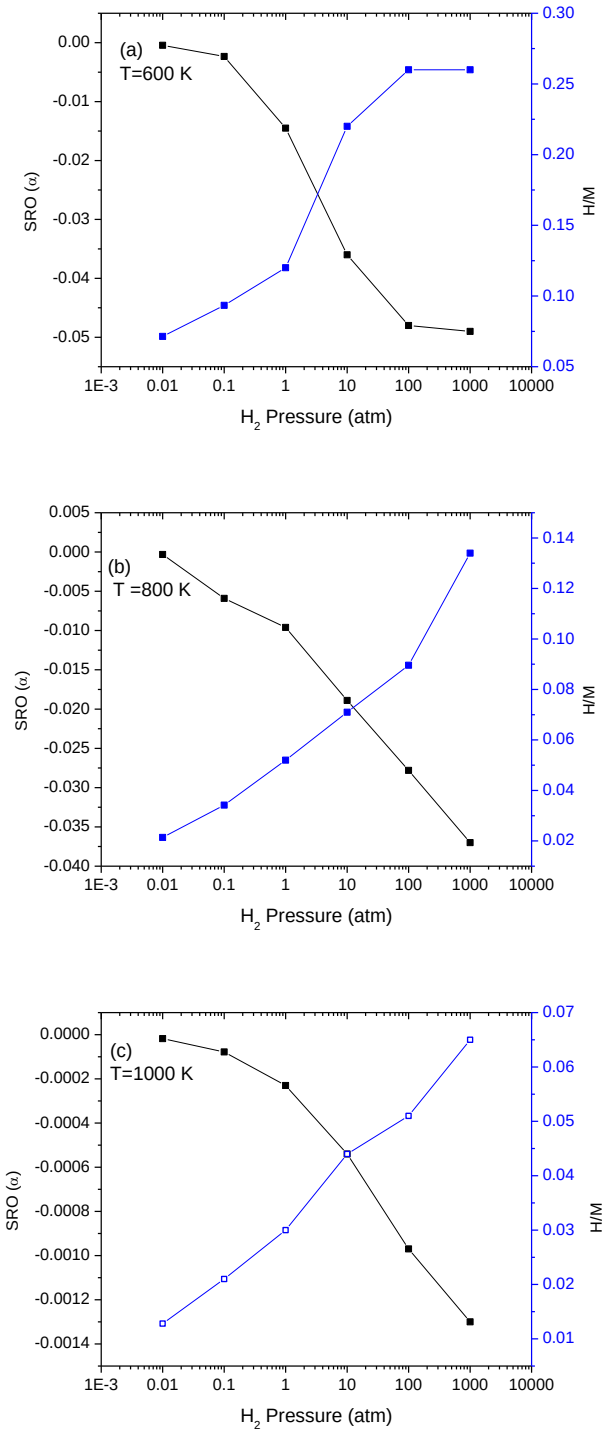

Figure 8.8: SRO and H_2 loadings (H/M) as a function of hydrogen pressure for $Pd_{96}Au_4$ at (a) 600 K (b) 800 K, and (c) 1000 K. The filled squares represent the SRO and the open squares are the hydrogen loadings.

As expected, the extent of ordering is higher at higher H pressures and low temperatures because the solubility of H decreases as the temperature increases. Similar observations were made for $Pd_{85}Au_{15}$ (Figure 8.4). The solubility in the ordered alloy is significantly higher than the alloy that has not been treated with H_2. The solubility calculations for the pure alloy $Pd_{96}Au_4$ at 1 atm H_2 and temperatures ranging from 400-1200 K have been reported in the literature [2]. At 600 K and 1 atm H_2, H/M of hydrogen heat treated $Pd_{96}Au_4$ increases by 25% in comparison with the pure alloy. A similar trend of increasing solubility after HHT of the alloys was observed by Lee et al. when $Pd_{81}Au_{19}$ was treated with hydrogen under identical conditions [4]. In $Pd_{85}Au_{15}$, the H/M after HHT at similar conditions increases up to 2 times that of the pure alloy. The calculations for solubility of pure $Pd_{85}Au_{15}$ were performed using the CE method described in the previous section without considering rearrangement of metal atoms.

Hydrogen induces ordering of metal atoms in the Pd-Au alloy. A higher concentration of H atoms in the system results in more prominent rearrangement of metal atoms. For example at 1000 atm H_2, H/M=0.27 at 600 K, which is higher than H/M=0.067 at 1000 K in $Pd_{96}Au_4$. Consequently, the α of the alloy structure at 1000 atm is -0.05 at 600 K and -0.0014 at 1000 K. A more negative α represents a greater extent of ordering due to higher amount of H in the system.

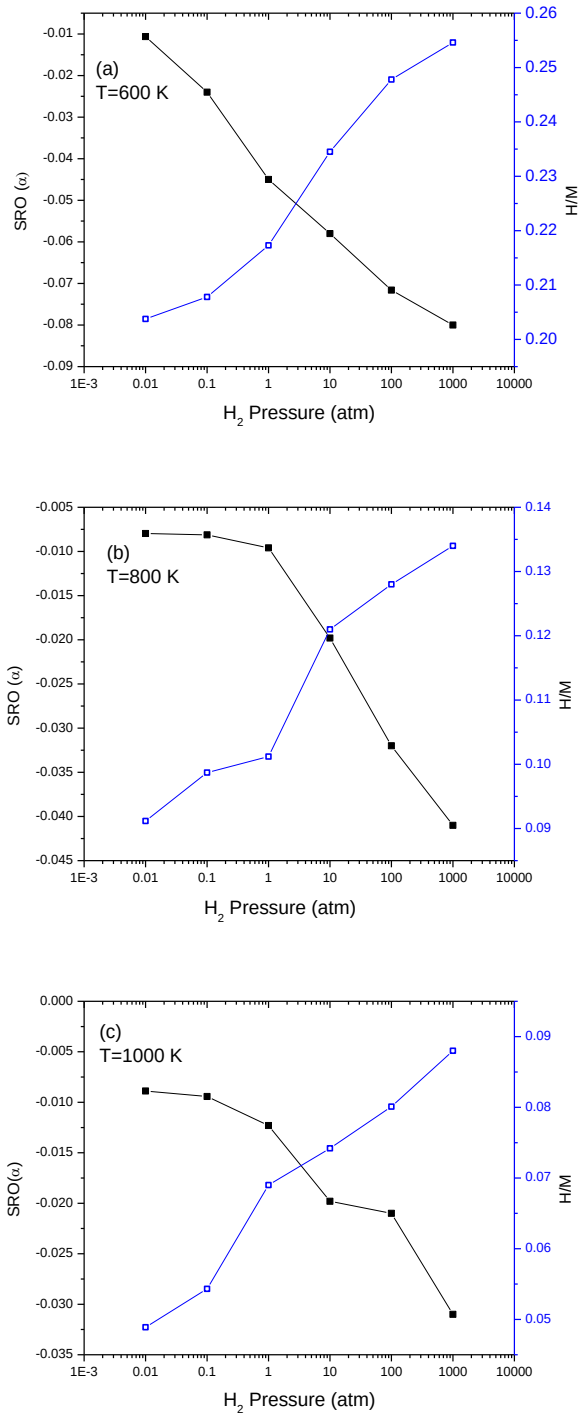

Figure 8.9: SRO and H_2 loadings (H/M) as a function of hydrogen pressure for $Pd_{85}Au_{15}$ at (a) 600 K (b) 800 K, and (c) 1000 K. The filled squares represent the SRO and the open squares are the hydrogen loadings.

8.4 Effect of hydrogen on diffusivity

The diffusivity of H in the alloy as a function of H pressure was calculated using the CE for the transition state energies and KMC methods discussed in Chapter 7. At each state point (SRO and H_2 pressure), the initial number of H atoms was obtained from the loadings obtained previously in the solubility calculations (Figs. 8.3 and 8.4).

In Figure 8.5, we plot the transport diffusivity (D) of H in the alloys as a function of H_2 pressure. The transport diffusivity is a product of the corrected diffusivity and the thermodynamic correction factor (TCF) as described in previous chapter. At low H_2 pressures (< 1 atm) and temperatures above 800 K, the corrected diffusivity is identical to the self-diffusivity in these materials since the TCF is ≈ 1. The thermodynamic correction factors at various H_2 pressures and temperatures are shown in Figure D.1 in Appendix D.

The diffusivity of H is highest at 1000 K and 1000 atm H_2 in $Pd_{96}Au_4$ and $Pd_{85}Au_{15}$. The diffusivity of H through the alloy increases with increase in temperature (600 K to 1000 K) and hydrogen pressure (0.01 atm to 1000 atm) as observed in Fig. 8.5. This increase in diffusivity with increase in the hydrogen pressure and temperature is observed in both alloys.

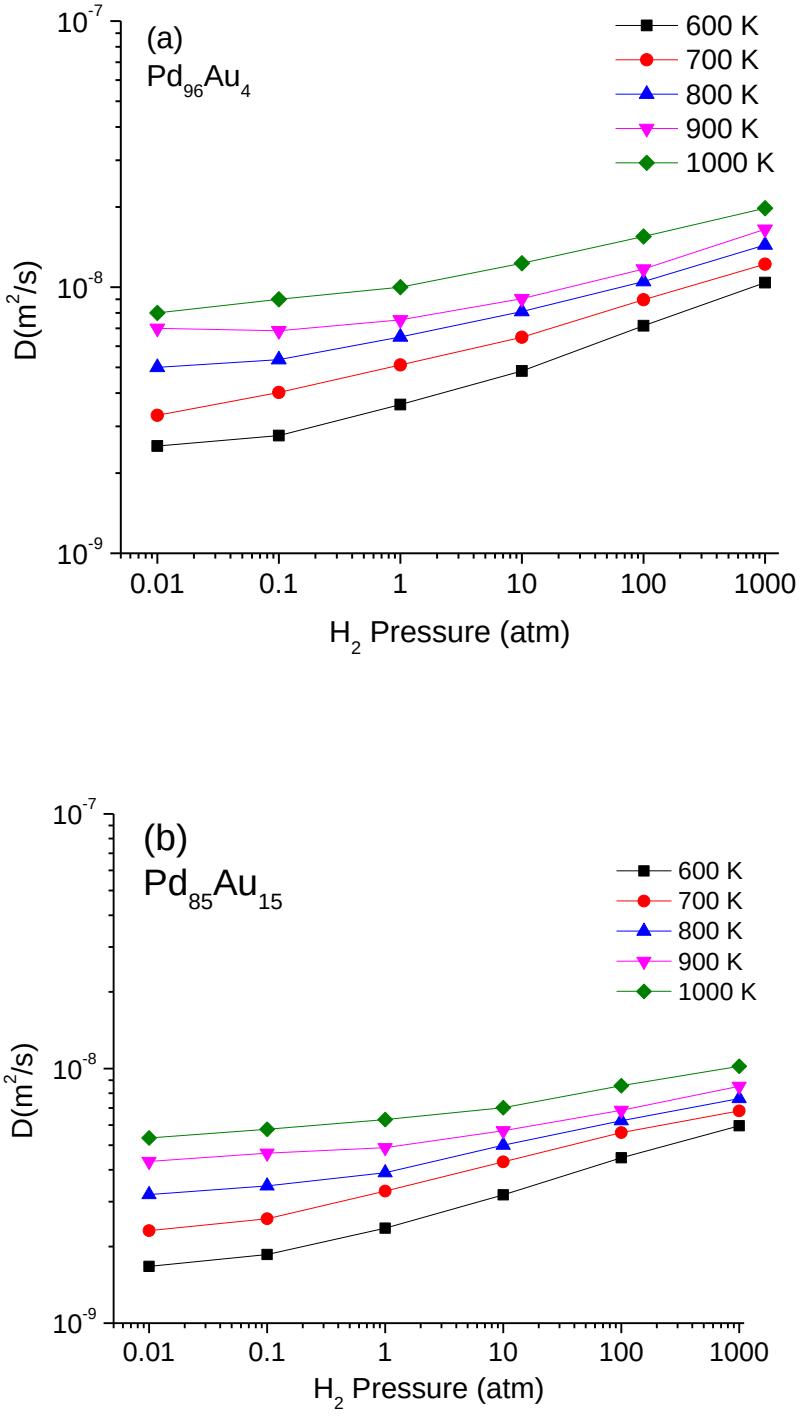

Figure 8.10: Diffusivity of H in (a) $Pd_{96}Au_4$ (b) $Pd_{85}Au_{15}$ as a function of the H_2 pressure.

As observed from Fig. 8.5, in $Pd_{96}Au_4$ ($Pd_{85}Au_{15}$) at 1000 K the diffusivity increases by a factor of 2.5 (1.9) due to the increase in H_2 pressure from 0.01 atm to 1000 atm. Similar trends of increasing diffusivity due to increased H_2 pressures are observed at all temperatures. However, an increase in H diffusivity due to high H concentration in the system is observed for non-hydrogen heat treated structures as well due to the hopping of H atoms between less favorable sites in addition to hops between the most favorable binding sites [2]. In order to determine the extent of increase in hydrogen diffusivity due to the rearrangement of metal atoms caused by H, the diffusivity of the hydrogen heat treated structures were compared with the diffusivity in the pure alloy (i.e., the alloy that has not been hydrogen heat treated), at various hydrogen pressures and temperatures. A comparison between the diffusivity of the hydrogen heat treated and pure structures is shown in Figure 8.6. For the calculation of H diffusion in the pure alloys, GCMC was performed at different hydrogen pressures ranging from 0.01 to 1000 atm and the diffusivity was calculated using KMC with activation energies obtained from the cluster expansion. In these calculations, the rearrangement of metal atoms was not considered.

The increase observed in the diffusivity in hydrogen heat treated structures in comparison to the pure alloys represents the influence of α on the diffusivity of H. Due to HHT, the diffusivity of H through $Pd_{96}Au_4$ increases by a factor of 1.8 in comparison to the pure alloy at 600 K and 1 atm P H_2. At higher temperatures (1000 K) and 1 atm P H_2, HHT results in an insignificant increase in diffusivity (a factor of 1.03). In $Pd_{85}Au_{15}$, the diffusivity increases at 600 K and 1 atm (1000 atm) by a factor of 3.6 (2). These results show that HHT has a nontrivial effect on H diffusion at 600 K, increasing the H diffusivity due to the rearrangement of metal atoms. At 1000 K, in $Pd_{96}Au_4$, the diffusivity increases by 3% due to HHT at 1 atm H_2 and by 3.1% at 1000 atm H_2. This increase in diffusivity due to HHT in comparison to the pure alloy at 1000 K is significantly lower than at 600 K because of the limited influence of H on SRO at the higher temperature.

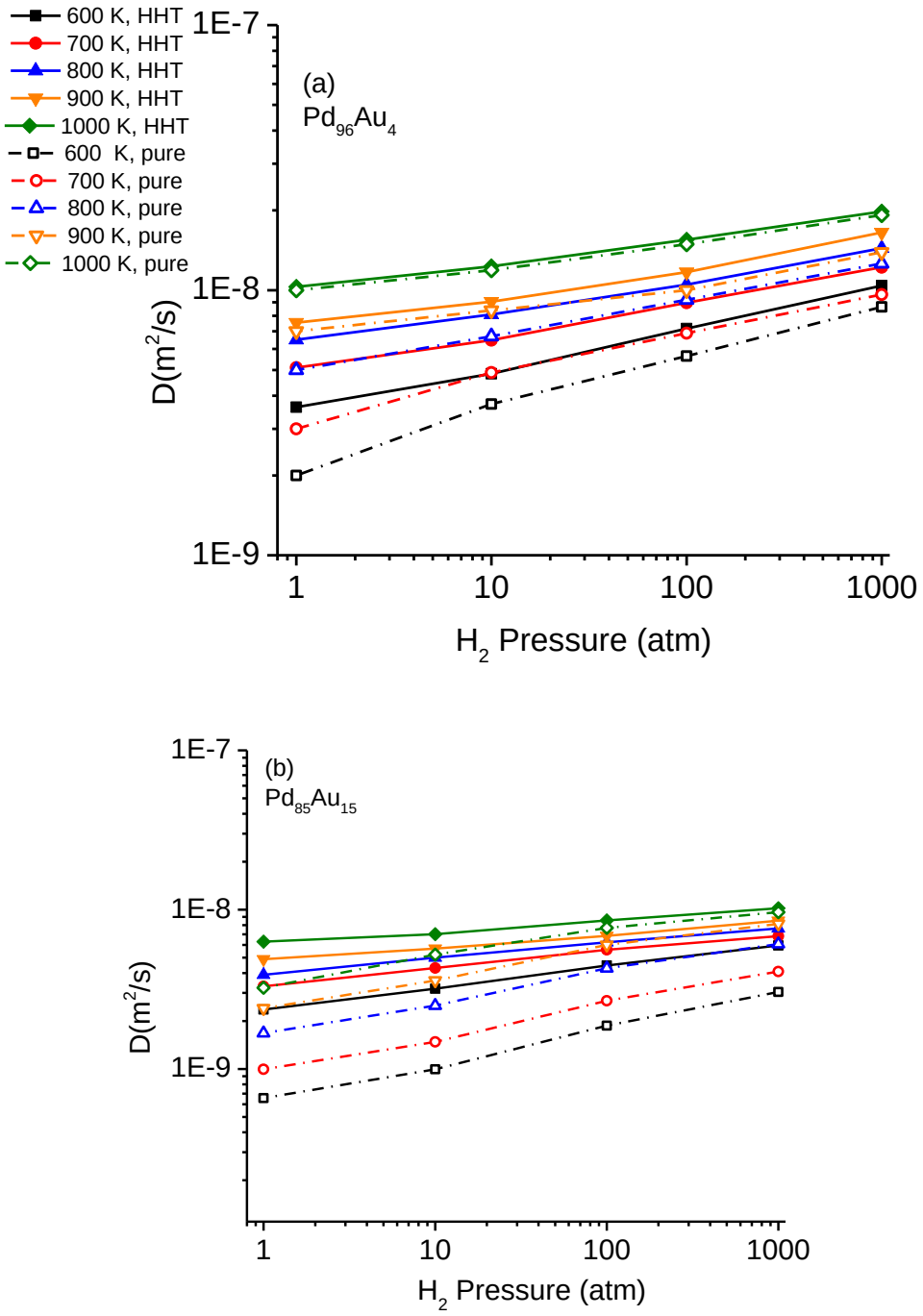

Figure 8.11: Diffusivity of H in HHT and pure (a) $Pd_{96}Au_4$ (b) $Pd_{85}Au_{15}$ at various temperatures and pressures. The pure (HHT) alloy is represented by open (filled) symbols and dashed (solid) lines. Identical color schemes are used in both (a) and (b). Lines are to guide the eye.

8.5 Permeability

Permeability is a convenient way to characterize flux through a metal membrane, and it can be defined as the product of solubility and diffusivity of H through a material at a given condition [5]. Using the solubility and diffusivity data calculated in previous sections, the permeability of H through $Pd_{96}Au_4$ and $Pd_{85}Au_{15}$ was calculated and is shown in Figure 8.7 as a function of H_2 pressure and temperature. The highest permeability is at 600 K and 1000 atm H_2 pressure in both alloys ($Pd_{96}Au_4$ and $Pd_{85}Au_{15}$). At these conditions, the solubility is high due to metal atom rearrangement and the diffusivity is also high due to the high H concentration resulting in high permeabilities.

There is a complex interplay of various factors such as extent of ordering, temperature and hydrogen pressure that influence the permeability of H at different conditions in $Pd_{96}Au_4$ and $Pd_{85}Au_{15}$. At low temperatures ($T \leq 700$ K), the high solubility of H in the rearranged alloy dominates over the diffusivity resulting in high values of permeability at all pressures. At high temperatures ($T > 700$ K), the high diffusivity of H through the material is the dominating effect in increasing the permeability of the alloy in comparison to the pure metal at all hydrogen pressures.

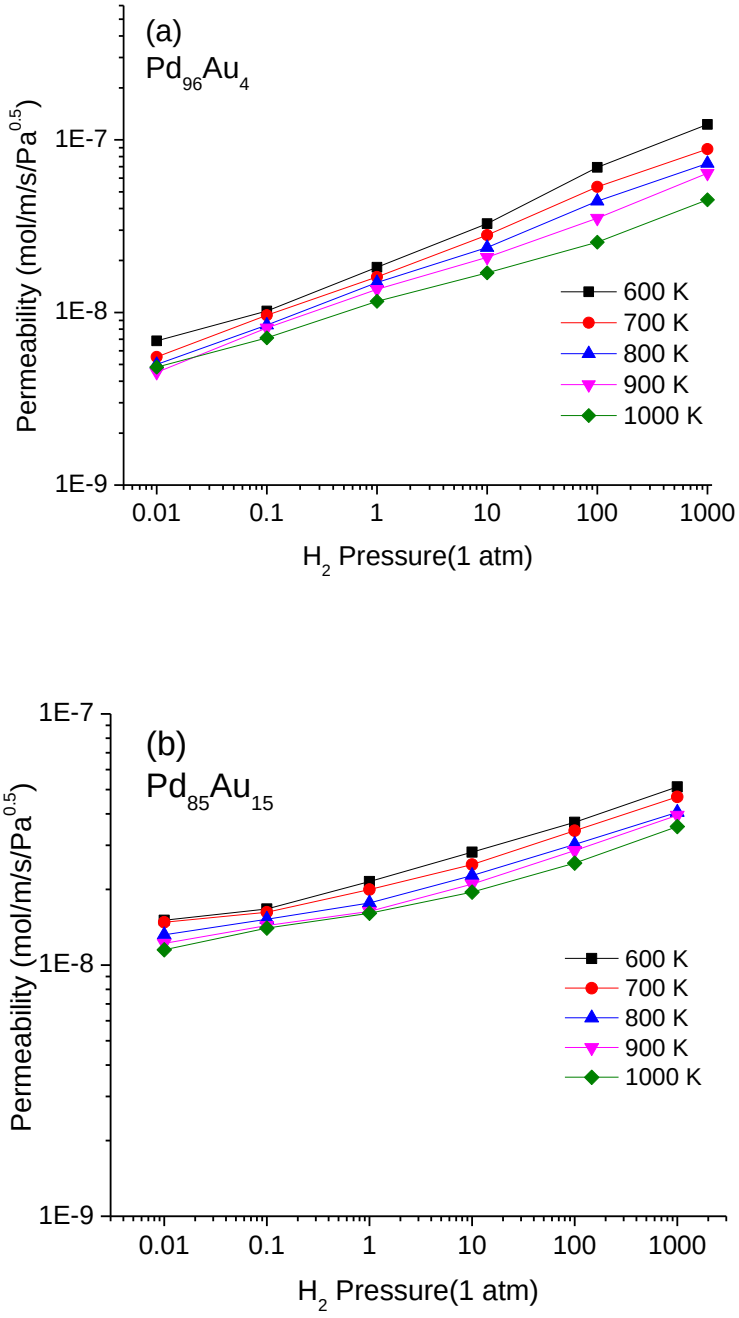

Figure 8.12: Permeability of (a) $Pd_{96}Au_4$ and (b) $Pd_{85}Au_{15}$ as a function of H_2 pressure. Lines are to guide the eye. Each set of symbols represent a particular temperature as listed in the legend.

To determine the increase in permeability of the alloys due to HHT alone, the permeability of pure alloys was calculated at various pressures and temperatures. In

Figure 8.8, the permeabilities of both HHT and pure $Pd_{96}Au_4$ and $Pd_{85}Au_{15}$ alloys are shown at various hydrogen pressures and temperatures. The permeability of the pure alloys is found to increase with increasing temperature. This is because the effect of increase in diffusivity at higher temperature is more prevalent over changes in solubility, leading to an overall increase in permeability at higher temperatures. This trend has been previously observed in $Pd_{96}Au_4$ alloys that have not been hydrogen heat treated [2].

In the case of hydrogen heat treated materials however, the increase in solubility due to H-induced metal atom rearrangement at lower temperatures is more significant than the increase in diffusivity at higher temperatures. Hence, the H permeability of hydrogen heat treated materials shows an opposite trend where the permeability decreases with increasing temperature. Nevertheless, HHT leads to a net increase in H permeability in the alloys as seen in Figure 8.8 (a) and (b). At 600 K, the permeability increases by a maximum of 5.4 (2.6) times in $Pd_{96}Au_4$ ($Pd_{85}Au_{15}$) after HHT at 1 atm H_2. At 1000 K and 1 atm H_2, the permeability increases by a factor of 2 (1.2) in $Pd_{96}Au_4$ ($Pd_{85}Au_{15}$) after HHT. Thus, as the temperature increases, the effect of HHT on the permeability of the alloy decreases. This trend is observed at all pressures of H_2 (from 0.01 to 1000 atm).

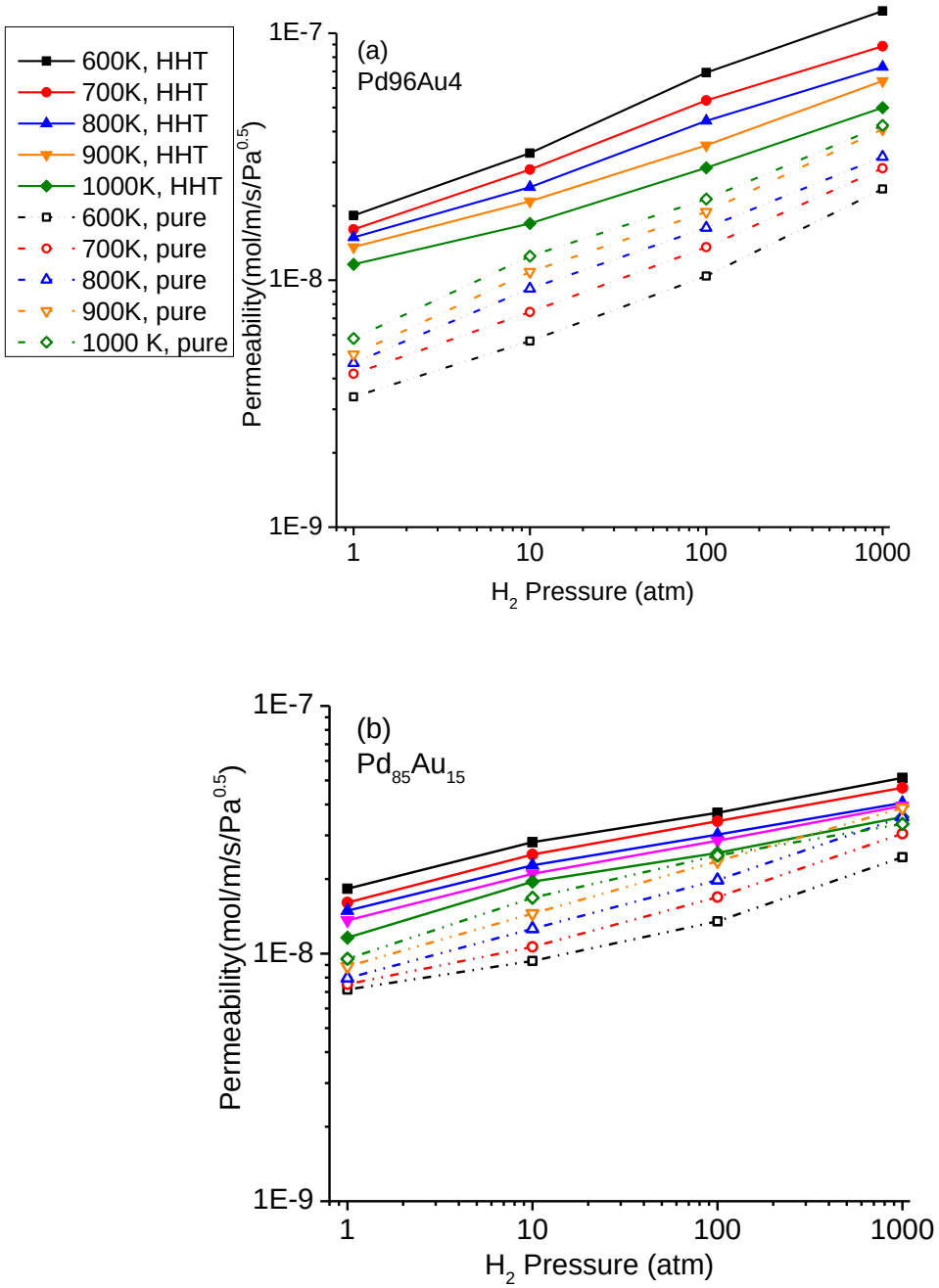

Figure 8.13: Permeability of H in HHT and pure (a) $Pd_{96}Au_4$ (b) $Pd_{85}Au_{15}$ at various temperatures and pressures. The pure (HHT) alloy is represented by open (filled) symbols and dashed (solid) lines. Identical color schemes are used in both (a) and (b). Lines are to guide the eye.

8.6 Conclusions

In this work, we have studied the rearrangement of metal atoms in two Pd-Au alloys of different compositions due to H at various pressures. The H atoms cause ordering in the alloys, which increases the solubility of H in the alloy. The hydrogen solubility is greatest for alloys that have been exposed to H_2 at the highest pressure at low temperatures (600-700 K), which is in agreement with experimental observations [4].

The permeability of the alloys treated with H is higher than the permeability of pure alloys. Thus, hydrogen heat-treated Pd-Au alloys are superior for membrane applications in comparison to alloys that have not been exposed to hydrogen. This increase in alloy performance for membrane applications after HHT could lead to identification of other alloy combinations or elements that have higher H permeabilities after exposure to H than in their pure (non-HHT) form. In this work, only two Pd-Au alloys were studied. The similarity of the results for the two alloys strongly suggests that our conclusions are valid for a broad range of Pd-Au compositions. The ordering observed due to H induced lattice rearrangement in this work is thermodynamic in nature. The kinetics of this process could be investigated to reveal the possibility of observing these effects under conditions of practical interest, but this investigation would best be pursued experimentally.

8.7 References

[1] S.G. Kang, K.E. Coulter, S.K. Gade, J.D. Way, D.S. Sholl, Identifying Metal Alloys with High Hydrogen Permeability Using High Throughput Theory and Experimental Testing, The Journal of Physical Chemistry Letters, 2 (2011) 3040-3044.

[2] L. Semidey-Flecha, D.S. Sholl, Combining density functional theory and cluster expansion methods to predict H_2 permeance through Pd-based binary alloy membranes, J. Chem. Phys., 128 (2008).

[3] P. Kamakoti, D.S. Sholl, Ab initio lattice-gas modeling of interstitial hydrogen diffusion in CuPd alloys, Physical Review B, 71 (2005) 9.

[4] S.M. Lee, H. Noh, B.F. Ted, S. Luo, Hydrogen-induced lattice rearrangement of a $Pd_{0.81}Au_{0.19}$ alloy, Journal of Physics: Condensed Matter, 19 (2007) 326222.

[5] P. Kamakoti, B.D. Morreale, M.V. Ciocco, B.H. Howard, R.P. Killmeyer, A.V. Cugini, D.S. Sholl, Prediction of hydrogen flux through sulfur-tolerant binary alloy membranes, Science, 307 (2005) 569-573.

CHAPTER 9

CONCLUSION AND OUTLOOK

9.1 Introduction

Metal membranes play a vital role in the production of pure H_2 from mixed gas streams. Ideal metal membranes must meet multiple objectives such as delivering high hydrogen fluxes, resistance to poisoning due to sulfur compounds in feed streams, having long operational lifetimes and be inexpensive to fabricate [1]. Defect-free dense metal membranes have a unique advantage over other types of membranes since they exhibit infinite selectivity towards hydrogen. This makes hydrogen separation using dense metal membranes attractive [2].

Experimental development of new membrane materials is hindered by the cost and effort required to experimentally fabricate and test hundreds of potential candidate materials. Many types of metal membranes such as pure metals, alloys, amorphous membranes have been studied extensively for hydrogen separation applications [1, 3-8]. Several favorable candidate materials have been successfully identified based on the computational methods developed to predict hydrogen fluxes through dense metal membranes [1, 4, 7]. The predicted permeabilities using these computational models are in excellent agreement with experimental results making these modeling methods invaluable in screening materials as membranes for hydrogen separation without any experimental input.

Using our modeling methods, we successfully identified 8 intermetallic materials that have permeabilities comparable to that of pure Pd which have not been studied previously. In this work, we have looked at hydrogen permeabilities of two different types of materials: intermetallics and alloys. The impact of this work and some future suggestions are discussed below for both types of materials.

9.2 Intermetallics

9.2.1 Impact and summary

This is the first work of its kind to screen binary intermetallics as potential candidates for hydrogen separation. We have successfully studied 1059 binary intermetallics. This is one of the largest sets of materials that have been computationally screened at this high level of theory. The 1059 binary intermetallics were divided into Pd-based and non-Pd based intermetallics and have been discussed in Part A of the thesis.

In order to examine this large set of materials, we have implemented a computational screening algorithm capable of predicting the performance of a large number of materials for hydrogen separation rapidly. This algorithm is based on prior models developed using a combination of first principles density functional theory (DFT) calculations and coarse grained lattice modeling. Two distinct properties together determine the permeability of H in the material – solubility and diffusivity. Atomic-scale DFT calculations of binding energies and vibrational frequencies were used as inputs to Sieverts' law, which was used to calculate the H solubility in an intermetallic. Calculation of permeability involves considerable computational efforts due to the large number of calculations involved in calculating the solubility of H in the various binding sites in the intermetallic and the activation barriers for the activated hops between binding sites that determine the diffusivity.

To reduce the number of DFT calculations we developed an algorithm that sorted the structures according to their space groups and used the knowledge of the binding site and activation barrier locations obtained by performing calculations on one representative structure from each space group across all the structures within the same space group. This method made the screening process 20 times more efficient while maintaining the level of theory at which these predictions were made. We chose the top 15 populated space groups in this work as described in Chapter 3.

Using the screening parameters and methods described in chapters 2 and 3, we were able to reduce the potential candidate materials significantly and performed detailed diffusivity and permeability calculations on a selected set of candidates. From our calculations on Pd-based binary intermetallics, we did not find any intermetallic that had H permeability that was higher or equal to pure Pd.

We also performed calculations on metastable states of Pd_3Mn to determine the influence of structure on the H solubility. Two metastable states were found to be stabilized in the presence of H at low pressures (10^{-12} atm). However, electrostatics and geometries of the binding sites of H in these materials did not show any particular trend explaining the favorable binding energies. We concluded that the binding of H in the material is a complex interplay of many factors such as chemical compositions, geometry and electrostatics.

8 intermetallics (non-Pd) were found to have permeability comparable to that of pure Pd. These 8 materials were found using our systematic screening procedure which would not have been discovered experimentally. It is interesting to note that only 2.5% of all the materials have solubility in the favorable range for H separation using membranes making computational tools indispensable for material screening and discovery. Most of the materials are also found to have higher diffusion barriers than pure Pd. It was also found that both diffusivity and solubility of a material need to be evaluated to estimate the permeability since no single property is dominant in influencing the H permeability of the material.

Predictions made using the models developed for H permeability prediction previously, which have also been used in this work, are in quantitative agreement with experimental results [1]. Based on this, we conclude that the predictions made for the intermetallics in this work are also quantitatively correct, despite the lack of experimental corroboration. These models can accurately predict hydrogen behavior in intermetallics without any experimental input. In all our permeability calculations, bulk

diffusion was assumed to be the rate-limiting step. In ultra-thin membranes, surface to subsurface diffusion plays an important role in the performance of the membrane. Extending our first principles approach to examine these effects will provide useful results in physical regimes where these effects become important.

9.3 Suggestions for future work

9.3.1 QSPR models

In our study on Pd-based intermetallics, we developed a QSPR model to predict binding energy rapidly. Although our model is not predictive in nature, the addition of other descriptors and higher order terms (our model was third order) may improve the model. The advantage of this approach is that if such an expression is developed, the calculation time for binding energy becomes negligible leading to rapid prediction of solubility. Potential energy surfaces of metals are complicated to predict, requiring complex higher order expressions involving a large number of quantum chemistry based descriptors which can be developed to rapidly calculate binding energies of materials.

9.3.2 New Materials

In this work, we looked at intermetallics that have been listed in the ICSD [9] and have been experimentally observed. Purely computational structures have not been included in this study. However, it is possible that there are many structures that have not been reported in ICSD, are not experimentally observed or do not exist. Computational quantum chemistry tools available today have the ability to predict the existence and properties of new materials or phases that are yet to be observed experimentally [10-14]. These powerful computational tools aid experimental efforts in the development of new materials and can lead to the identification and characterization of novel materials that is not achievable using experiments alone.

9.3.3 Ternary intermetallics

In this work, we have only examined all possible binary intermetallics. Ternary intermetallics that are a combination of three or more metals resulting in ordered compounds exist. The methods developed in this work are easily transferable to ternary systems and can be used to identify ternary intermetallics that are favorable for hydrogen separation.

9.3.4 Hydrogen storage

The methods we have developed will be useful in other applications where the solubility and diffusion of hydrogen in metals plays a role. Metal hydrides have received wide attention as possible hydrogen storage materials [15-17]. In these applications, solubility is crucial as it is closely related to the net storage capacity of the metal hydrides. There are differences between the membrane situation we have considered at length in this thesis and hydrogen storage in metal hydrides. For example, hydrogen storage involves high concentrations of hydrogen, unlike the dilute concentrations that characterize interstitial hydrogen in membrane applications. Nevertheless, the theoretical tools we have introduced here will be useful in screening materials for hydrogen storage in complex metal hydrides [16, 17].

9.4 Pd-Au alloys

9.4.1 Impact and summary

In part B of this thesis, a novel computational method was developed to study lattice rearrangements in alloys due to interstitial H. This method allowed us to calculate the extent of lattice rearrangement and predict conditions that maximize this effect. Most importantly, the effect of this lattice rearrangement on H permeability through these alloys was examined. Using a combination of cluster expansion models developed previously for hydrogen solubility and Pd-Au formation energies, a self-consistent procedure was developed that allows metal atom rearrangement and also calculates the

solubility of hydrogen in the equilibrium structure obtained. This is the first study of its kind to computationally predict an increase in solubility due to lattice ordering in Pd-Au alloys, in agreement with experimental observations. Using the tools developed in this work, we were also able to predict enhanced permeabilities in two Pd alloys ($Pd_{96}Au_4$ and $Pd_{85}Au_{15}$) due to H induced lattice ordering.

9.5 Suggestions for future work

In this work, only two alloys, $Pd_{96}Au_4$ and $Pd_{85}Au_{15}$, have been studied. Both of these alloys show enhanced permeability after H induced lattice rearrangement. However, there may be other alloys that show similar enhancement in permeability after HHT (hydrogen heat treatment). The methods developed in this work enable the study of other similar alloy systems and can predict element combinations that result in favorable H permeabilities after HHT.

9.6 References

[1] P. Kamakoti, B.D. Morreale, M.V. Ciocco, B.H. Howard, R.P. Killmeyer, A.V. Cugini, D.S. Sholl, Prediction of hydrogen flux through sulfur-tolerant binary alloy membranes, Science, 307 (2005) 569-573.

[2] N.W. Ockwig, T.M. Nenoff, Membranes for hydrogen separation, Chemical Reviews, 107 (2007) 4078-4110.

[3] B.D. Morreale, M.V. Ciocco, R.M. Enick, B.I. Morsi, B.H. Howard, A.V. Cugini, K.S. Rothenberger, The permeability of hydrogen in bulk palladium at elevated temperatures and pressures, Journal of Membrane Science, 212 (2003) 87-97.

[4] S.G. Kang, K.E. Coulter, S.K. Gade, J.D. Way, D.S. Sholl, Identifying Metal Alloys with High Hydrogen Permeability Using High Throughput Theory and Experimental Testing, The Journal of Physical Chemistry Letters, 2 (2011) 3040-3044.

[5] L. Semidey-Flecha, C. Ling, D.S. Sholl, Detailed first-principles models of hydrogen permeation through PdCu-based ternary alloys, Journal of Membrane Science, 362 (2010) 384-392.

[6] L. Semidey-Flecha, D.S. Sholl, Combining density functional theory and cluster expansion methods to predict H-2 permeance through Pd-based binary alloy membranes, Journal of Chemical Physics, 128 (2008) 1-10.

[7] S.Q. Hao, D.S. Sholl, Using first-principles calculations to accelerate materials discovery for hydrogen purification membranes by modeling amorphous metals, Energy & Environmental Science, 1 (2008) 175-183.

[8] C. Ling, D.S. Sholl, First principles investigation of metal sulfides as membranes in hydrogen purification, Journal of Membrane Science, 329 (2009) 153-159.

[9] G. Bergerhoff, I.D. Brown, Crystallographic Databases, International Union of Crystallography, Chester, 1987.

[10] M. Jahnátek, O. Levy, G.L.W. Hart, L.J. Nelson, R.V. Chepulskii, J. Xue, S. Curtarolo, Ordered phases in ruthenium binary alloys from high-throughput first-principles calculations, Physical Review B, 84 (2011) 214110.

[11] G.L.W. Hart, S. Curtarolo, T.B. Massalski, O. Levy, Comprehensive Search for New Phases and Compounds in Binary Alloy Systems Based on Platinum-Group Metals, Using a Computational First-Principles Approach, Physical Review X, 3 (2013) 041035.

[12] O. Levy, G.L.W. Hart, S. Curtarolo, Hafnium binary alloys from experiments and first principles, Acta Mater., 58 (2010) 2887-2897.

[13] R.H. Taylor, S. Curtarolo, G.L.W. Hart, Predictions of the Pt8Ti Phase in Unexpected Systems, Journal of the American Chemical Society, 132 (2010) 6851-6854.

[14] L.J. Nelson, G.L.W. Hart, S. Curtarolo, Ground-state characterizations of systems predicted to exhibit $L1_1$ or $L1_3$ crystal structures, Physical Review B, 85 (2012) 054203.

[15] S.V. Alapati, J.K. Johnson, D.S. Sholl, Large-scale screening of metal hydride mixtures for high-capacity hydrogen storage from first-principles calculations, Journal of Physical Chemistry C, 112 (2008) 5258-5262.

[16] K.M. Nicholson, D.S. Sholl, Computationally efficient determination of hydrogen isotope effects on the thermodynamic stability of metal hydrides, Physical Review B, 86 (2012) 134113.

[17] K.C. Kim, A.D. Kulkarni, J.K. Johnson, D.S. Sholl, Large-scale screening of metal hydrides for hydrogen storage from first-principles calculations based on equilibrium reaction thermodynamics, Physical Chemistry Chemical Physics, 13 (2011) 7218-7229.

APPENDIX A

LATTICE PARAMETERS AND QSPR MODELS

Table A.1: Comparison of the experimental and the DFT calculated structural parameters of intermetallics. All distances are in Angstroms.

Compound	Space Group	ICSD values	Calculated lattice parameters	Calculated Volume/ICSD volume
PdSc	Pm-3m	a=3.28	a=3.29	0.990
Pd_3Sc	Pm-3m	a=3.98	a=3.97	1.009
PdTi	Pm-3m	a=3.18	a=3.16	1.019
$PdTi_2$	I4/mmm	a=3.09,c=10.05	a=3.02,c=10.05	1.045
Pd_2Ti	Immm	a=3.46,b=3.1,c=8.73	a=3.45,b=3.07,c=8.67	0.996
Pd_3Ti	Pm-3m	a=3.93	a=3.92	1.007
Pd_3Ti_2	Cmcm	a=14.33,b=4.64,c=4.61	a=14.31,b=4.68,c=4.64	1.008
Pd_5Ti_3	P4/mmm	a=3.3,c=11.51	a=3.30,c=11.55	0.994
PdV_3	Pm-3n	a=4.83	a=4.79	1.022
Pd_2V	Immm	a=2.75,b=8.25,c=3.75	a=2.75,b=8.25,c=3.75	1.000
Pd_3V	I4/mmm	a=3.85,c=7.75	a=3.84,c=7.75	1.002
PdMn	P4/mmm	a=2.88,c=3.59	a=2.96,c=3.12	1.094
Pd_3Mn	I4mm	a=3.91,c=15.5	a=3.92,c=15.45	1.001
PdFe	P4/mmm	a=3.86,c=3.71	a=3.88,c=3.75	0.980
Pd_3Fe	Pm-3m	a=3.85	a=3.86	0.996
$PdFe_3$	Pm-3m	a=3.82	a=3.73	1.059
PdCo	Fm-3m	a=3.75	a=3.756	1.003
PdNi	Fm-3m	a=3.76	a=3.64	1.099
PdCu	Im-3m	a=3.06	a=3.07	1.007
$PdCu_3$	Pm-3m	a=3.72	a=3.70	1.018
$PdCu_4$	P42/M	a=5.83,c=7.33	a=5.99,c=7.24	0.958
PdZn	P4/mmm	a=2.9,c=3.35	a=2.89,c=3.34	1.006
Pd_5Ga_2	Pnma	a=5.49,b=4.08,c=18.4	a=5.48,b=4.08,c=18.2	1.024
Pd_5Ga_3	Pbam	a=10.51,b=5.42,c=4.03	a=10.50,b=5.40,c=4.01	0.991
Pd_7Ga_3	Im-3m	a=8.77	a=8.76	0.974
Pd_3Y	Pm-3m	a=4.07	a=4.05	1.004
$PdZr_2$	I4/mmm	a=3.31	a=3.30	0.987
Pd_2Zr	I4/mmm	a=3.41	a=3.40	0.979
Pd_4Zr_3	R-3H	a=12.50,c=5.54	a=12.42,c=5.51	1.023
PdNb	Fm-3m	a=4.02	a=4.10	1.061
Pd_3Nb	I4/mmm	a=3.9,c=7.92	a=3.87,c=7.98	1.007
$PdNb_3$	Im-3m	a=3.24	a=3.24	1.002
PdRh	Fm-3m	a=3.9	a=3.89	0.975
PdAg	Fm-3m	a=3.98	a=3.98	1.000

Table A.1 continued

Compound	Space Group	ICSD values	Calculated lattice parameters	Calculated Volume/ICSD volume
Pd_3Cd	Fm-3m	a=3.97	a=3.96	1.064
Pd_8Cd_{43}	P4-3M	a=9.94	a=9.93	0.972
Pd_3Pb	Pm-3m	a=4.01	a=4.01	0.983
Pd_3Hf	P63/mmc	a=5.6,c=9.19	a=5.5,c=9.10	1.000
Pd_3Zr	P63/mmc	a=5.61,c=9.24	a=5.61,c=9.24	1.000
PdIn	Pm-3m	a=3.25	a=3.401	1.149
Pd_2In	Pnma	a=5.61,b=4.22,c=8.24	a=5.67,b=4.28,c=8.28	0.971
Pd_3In	P4/mmm	a=4.07	a=4.07	0.931
Pd_2In_3	P3-m1	a=4.52,c=5.49	a=4.56,c=5.62	0.831
Pd_5In_3	Pbam	a=5.6,b=11.02,c=4.24	a=5.67,b=11.13,c=4.39	0.945
$PdSn_2$	I41/ACDS	a=6.49,c=24.38	a=6.19,c=24.73	1.084
Pd_3Sn	Pm-3m	a=3.976	a=4.02	0.949
PdSn	PCMN	a=6.32,b=3.87,c=6.13	a=6.21,b=4.05,c=6.37	0.932
$PdSn_4$	ABA2	a=6.39,b=6.44,c=11.44	a=6.39,b=6.45,c=11.52	0.955
$PdHf_2$	I4/mmm	a=3.25,c=11.06	a=3.81,c=8.22	0.976
Pd_5Hf	Cmmm	a=12,b=4.07,c=14.07	a=12.39,b=4.16,c=3.34	3.983
Pd_3Tl	Pm-3m	a=3.82	a=3.70	1.100
Pd_2Ta	Immm	a=2.9,b=8.4,c=3.8	a=2.89,b=8.47,c=3.85	0.977
Pd_3Ta	I4/mmm	a=3.88,c=7.98	a=4.47,c=6.12	1.018
PdTa	Fm-3m	a=4.0	a=4.01	1.000
PdIr	fm-3m	a=3.86	a=3.91,c=3.99	0.943
PdPt	Fm-3m	a=3.9	a=3.95	0.963
PdAu	Fm-3m	a=3.98	a=4.034	0.959
PdHg	P4/mmm	a=3.02,c=3.71	a=4.04	1.936
Pd_2Hg_5	P4/mbm	a=9.46,c=3.03	a=9.23,c=2.97	1.074
PdZr	Cmcm	a=3.33, b=10.30, c=4.37	a=3.33,b=10.28,c=4.35	1.009
Pd_2Ga	Pnma	a=4.06,b=5.49,c=7.81	a=4.3,b=5.5,c=7.96	0.973
Pd_4Zr	Fm-3m	a=3.96	a=3.96	0.927
PdMo	P63/mmc	a=2.78,c=4.49	a=2.97,b=5.17	1.001
PdCd	P4/mmm	a=3.03,c=3.63	a=3.11,b=3.63	0.947
Pd_2Sn	Pnma	a=4.31,b=5.65,c=8.12	a=4.365,b=5.7,c=8.2	0.948
Pd_3Sn	Pm-3m	a=3.98	a=4.027	0.971
$PdAu_3$	Pm-3m	a=4.04	a=4.01	0.962
Pd_3Au	Pm-3m	a=3.95	a=3.75	1.021
$PdTl_2$	I4/mcm	a=5.55	a=6.12	1.163
$PdPb_2$	!4/mcm	a=5.67	a=5.81	1.130
$PdBi_2$	C12/M1	a=4.25,b=5.66,c=6.72	a=4.3,b=5.60,c=5.12	0.997
PdBi	P1211	a=7.2,b=8.71,c=10.66	a=6.9,b=8.5,c=10.0	1.030
Pd_3Bi	Pmmma	a=9.94,b=5.76,c=4.95	a=9.54,b=5.83,c=5.01	1.004
Pd_5Bi_2	C12/M1	a=14.43,b=5.78,c=6.75	a=14.04,b=5.4,c=6.24	0.996

Table A.2: The various QSPR models tested in this work. The R^2 value was highest for Model M11 (0.58). The description of the various descriptors used is listed in the legend below the table.

Model	Equation	R^2
M1	1.6468×DH-0.002×V+0.7749×WEN+0.0417×WFN+0.5228×WBE-0.138	0.28
M2	1.7867×DH-0.002×V+0.2197×WEN+0.0756×WFN+0.3625×WBE+0.2056×DH^2+0.3806×WEN^2+0.1026×WBE^2-0.07	0.28
M3	-0.811×DH-0.002×V+1.3818×WEN-0.101×WFN+0.7716×WBE+4.5173×DH×WEN-0.636×WEN×WBE-0.819×DH×WBE-0.163	0.34
M4	-0.914×DH-0.002×V+1.4664×WEN-0.104×WFN+0.7789×WBE+4.7709×DH×WEN-0.701×WEN×WBE-0.34×DH×WBE-DH×WBE×WEN-0.183	0.34
M5	-0.914×DH-0.002×V+1.4664×WEN-0.104×WFN+0.7789×WBE-0.701×WEN×WBE-5.111×DH×WBE-DH×WBE×WEN+4.7709×DH(WBE+WEN)-0.183	0.34
M6	-0.897×DH-0.002×V+1.4606×WEN-0.102×WFN+0.7835×WBE-0.668×WEN×WBE-5.135×DH×WBE-0.894×DH×WBE×WEN+4.7467×DH(WBE+WEN)-0.019×WBE×WFN-0.184	0.34
M7	0.4945×DH-0.002×V+2.9008×WEN-0.642×WFN+0.8236×WBE-1.651×WEN×WBE-12.79×DH×WBE-0.62×DH×WBE×WEN+11.556×DH(WBE+WEN)+0.2822×WBE×WFN-0.001×DH×V-4.225×DH×WFN-0.3	0.44
M8	0.3707×DH-0.002×V+2.4561×WEN-0.723×WFN+0.8323×WBE-1.62×WEN×WBE-12.53×DH×WBE-0.588×DH×WBE×WEN+11.278×DH(WBE+WEN)+0.2545×WBE×WFN-0.001×DH×V-4.09×DH×WFN+0.2246×WEN×WFN-0.172	0.44
M9	-0.058×DH-0.002×V+2.5202×WEN-1.003×WFN+0.6739×WBE-1.604×WEN×WBE-13.22×DH×WBE+0.2605×DH×WBE×WEN+11.673×DH(WBE+WEN)+0.3084×WBE×WFN+0.0036×DH×V-4.58×DH×WFN+0.6971×WEN×WFN+0.001×WBE×V-0.565×WEN^3-0.0003	0.46
M10	-0.058×DH-0.002×V+2.5202×WEN-1.003×WFN+0.6739×WBE-1.604×WEN×WBE-13.22×DH×WBE+0.2605×DH×WBE×WEN+12.239×DH(WBE+WEN)+0.3084×WBE×WFN+0.0036×DH×V-4.58×DH×WFN+0.6971×WEN×WFN+0.001×WBE×V-0.565×WEN^3+DH(WBE+WFE)-0.0003	0.46
M11	2.0128×DH-0.0008×V+1.4243×WEN-0.03×WFN+0.5909×WBE-0.17×WEN×WBE-7.491×DH×WBE+4.3283×DH×WBE×WEN+4.2897×DH(WBE+WEN)-0.084×WBE×WFN+0.0043×DH×V-2.635×DH×WFN-0.377×WEN×WFN+0.0003×WBE×V-0.139×WEN^3-0.1167	0.58

Legend	Description	Legend	Description
DH	**Heat of hydride formation from Griessen's model**	**WFN**	**Weighted work function**
V	**Volume of unit cell**	**WBE**	**Weighted elemental binding energy**
WEN	**Weighted electronegativity difference**		

APPENDIX B

$Pd_{85}Au_{15}$ AND $Pd_{96}Au_4$ CLUSTER EXPANSION MODELS

Cluster Expansion for H binding sites and transition sites in $Pd_{85}Au_{15}$

To generate the cluster expansion to calculate the binding energies in O and T sites in fcc-$Pd_{85}Au_{15}$ alloy, we followed the procedure developed by Semidey-Flecha et. al in calculation of the cluster expansion for $Pd_{96}Au_4$ alloys.[1] To parameterize the cluster expansion for $Pd_{85}Au_{15}$,we performed 21 DFT calculations for O-site energies and 21 calculations for T-site energies. These calculations were performed using PW91 generalized gradient approximation functional, a plane wave cut off of 240 eV and a Γ-centered grid of 4×4×4 kpoints. Each calculation had a 27 atom supercell with 4 Au atoms and 23 Pd atoms resulting in an atomic composition of $Pd_{85.2}Au_{14.8}$ which we refer to as $Pd_{85}Au_{15}$ for convenience. The positions of the atoms were allowed to relax until the forces on all the atoms were less than 0.03 eV/ Å. For the TS, a truncated CE with 29 distinct interactions from a combination of the CE for T-sites and O-sites was generated using the procedure previously developed by Semidey Flecha et. al.[1]

In the tables below the final terms of the CE used to generate the binding and transition site energies are shown. Table S1 and S3 list the details of the interactions considered during the generation of the cluster expansion.[1] L refers to the lattice constant of the Pd alloys. An entry shown by a dash indicates a parameter that was not considered in the LOO-based CE analysis. All energies are reported in eV.

Reference:

[1] L.Semidey-Flecha and D.S. Sholl, J.Chem. Phys. **128** (2008).

Table B.1: Description of O Site Cluster Expansion parameters*

Parameter ID #:	Description
1	Number of Pd atoms in the 2 x N shell normalized by 2
2	Number of Pd atoms in the 3 x N shell n0rmalized by 3
3	Number of Cu (M in the case of the binary alloys) atoms in the 2 x N shell normalized by 2
4	Number of Cu (M in the case of the binary alloys) atoms in the 3 x N shell normalized by 3
5	Number of M (in the ternary alloys) atoms in the 2 x N shell normalized by 2
6	Number of M (in the ternary alloys) atoms in the 3 x N shell normalized by 3
7	2 body interactions between metal atoms separated by L/sqrt(2) in the 2 x N shell normalized by L/sqrt(2)
8	2 body interactions between metal atoms separated by L in the 2 x N shell normalized by L
9	2 body interactions between metal atoms separated by L in the 3 x N shell normalized by L
10	2 body interactions between metal atoms separated by sqrt(2)*L in the 3 x N shell normalized by sqrt(2)*L
11	2 body interactions between metal atoms separated by sqrt(3)*L in the 3 x N shell normalized by sqrt(3)*L
12	2 body interactions between metal atoms in the 2 x N shell separated by L/sqrt(2) to atoms in the 3 x N shell normalized by L/sqrt(2)
13	3 body interactions between metal atoms in the 2 x N shell where each atom is separated by L/sqrt(2) normalized by L/sqrt(2)
14	3 body interactions between metal atoms in the 3 x N shell where each atom is separated by Lnormalized by L
15	4 body interactions between metal atoms in the 2 x N shell where each atom is separated by L/sqrt(2) normalized by 2
16	4 body interactions between metal atoms in the 3 x N shell where each atom is separated by sqrt(2) *L normalized by 3
17	Number of Pd atoms in the 4 x N shell normalized by 4
18	Number of Cu (M in the binary alloys) atoms in the 4 x N shell normalized by 4
19	Number of M (in ternary alloys) atoms in the 4 x N shell normalized by 4
20	Number of Pd atoms in the 5 x N shell normalized by 5

*L.Semidey-Flecha and D.S. Sholl, J.Chem. Phys. **128** (2008).

Table B.2: $Pd_{96}Au_4$ O site binding energies and ZPE in eV*

	E_b	ZPE
E_o	0.7067	0.9206
1	0.3194	0.2929
2	-	-
3	-	-0.2296
4	0.0325	-
5	-	-
6	-	-
7	-	0.0169
8	0.1510	-0.0541
9	-	-
10	-	-
11	-	-
12	-	-
13	-	-
14	-	-
15	-	-
16	-	-
17	-	-
18	-	-
19	-	-
20	-	-

*L.Semidey-Flecha and D.S. Sholl, J.Chem. Phys. **128** (2008).

Table B.3: Description of T Site Cluster Expansion parameters*

Parameter ID	Description
1	Number of Pd atoms in the 2 x N shell normalized by 2
2	Number of Pd atoms in the 3 x N shell n0rmalized by 3
3	Number of Cu (M in the case of the binary alloys) atoms in the 2 x N shell normalized by 2
4	Number of Cu (M in the case of the binary alloys) atoms in the 3 x N shell normalized by 3
5	Number of M (in the ternary alloys) atoms in the 2 x N shell normalized by 2
6	Number of M (in the ternary alloys) atoms in the 3 x N shell normalized by 3
7	2 body interactions between metal atoms separated by L/sqrt(2) in the 2 x N shell normalized by L/sqrt(2)
8	2 body interactions between metal atoms separated by L/sqrt(2) in the 3x N shell normalized by L/sqrt(2)
9	2 body interactions between metal atoms separated by (sqrt(6)*L)/2 in the 3 x N shell normalized by (sqrt(6)*L)/2
10	2 body interactions between metal atoms separated by sqrt(2)*L in the 3 x N shell normalized by sqrt(2)*L
11	2 body interactions between metal atoms separated by (sqrt(10)*L) /2 in the 3 x N shell normalized by (sqrt(10)*L)/2
12	2 body interactions between metal atoms in the 2 x N shell separated by L/sqrt(2) to atoms in the 3 x N shell normalized by L/sqrt(2)
13	2 body interactions between metal atoms in the 2 x N shell separated by L to atoms in the 3 x N shell normalized by L
14	2 body interactions between metal atoms in the 2 x N shell separated by(sqrt(6)*L)/2 to atoms in the 3 x N shell normalized by (sqrt(6)*L)/2
15	Number of Pd atoms in the 4 N shell normalized by 4
16	Number of Cu (M in the binary alloys) atoms in the 4 x N shell normalized by 4
17	Number of M (in ternary alloys) atoms in the 4 x N shell normalized by 4
18	2 body interactions between metal atoms separated by L/sqrt(2) in the 4 x N shell normalized by L/sqrt(2)
19	2 body interactions between metal atoms in the 3 x N shell separated by L/sqrt(2) to atoms in the 4 x N shell normalized by L/sqrt(2)
20	2 body interactions between metal atoms in the 2 x N shell separated by L to atoms in the 4 x N shell normalized by L
21	Number of Pd atoms in the 5 N shell normalized by 5
22	Number of Cu (M in the binary alloys) atoms in the 5 x N shell normalized by 5
23	Number of M (in ternary alloys) atoms in the 5 x N shell normalized by 5
24	3 body interactions between metal atoms in the 2 x N shell separated by L/sqrt(2) normalized by L/sqrt(2)
25	3 body interactions between metal to metal atoms separated by L/sqrt(2) in the 2 x N shell to atoms in the 3 x N shell separated by L/sqrt(2) normalized by L/sqrt(2)

Table B.3 continued

26	3 body interactions between metal atoms in the 3 x N shell separated by L/sqrt(2) normalized by L/sqrt(2)
27	3 body interactions between two metal atoms separated by L/sqrt(2) in the 3 x N shell to atoms in the the 2 x N shell separated by L/sqrt(2) normalized by L/sqrt(2)
28	3 body interactions between two metal atoms separated by (sqrt(6)*L)/2 in the 3 x N shell to atoms in the the 2 x N shell separated by L/sqrt(2) normalized by (sqrt(6)*L)/2
29	3 body interactions between metal atoms in the 4 x N shell separated by L/sqrt(2) normalized by L/sqrt(2)
30	3 body interactions between two metal atoms separated by L/sqrt(2) in the 3 x N shell to atoms in the the 4 x N shell separated by L/sqrt(2) normalized by L/sqrt(2)

*L.Semidey-Flecha and D.S. Sholl, J.Chem. Phys. **128** (2008).

Table B.4: $Pd_{96}Au_4$ T site binding energies and ZPE in eV*

	E_b	ZPE
E_o	0.8591	0.1960
1	0.5054	0.0100
2	-	-
3	-	-
4	-	-
5	-	-
6	-	-
7	0.0086	0.0043
8	-	-
9	-	-
10	-	-
11	-0.0040	-
12	-	-
13	0.0260	-
14	-0.0056	0.0012
15	-	-
16	-	-
17	-	-
18	-	-
19	-0.0005	-
20	-0.0019	-0.0013
21	-	-
22	-	-
23	-	-
24	-	-
25	-	-
26	-	-
27	-	-
28	-	-
29	-	-
30	-	-

*L.Semidey-Flecha and D.S. Sholl, J.Chem. Phys. **128** (2008).

Table B.5: Binding energy and ZPE of H in Transition State sites in $Pd_{96}Au_4$ *

	E_b	ZPE
E_o	1.4747	0.2027
O 1	-	-0.0044
O 2	-	-
O 3	-	-
O 4	-	-
O 5	-	-
O 6	-	-
O 7	-	-
O 8	-	-
O 9	-	-
O 10	-	-
O 11	-	-
O 12	-0.0081	-
O 13	-	-
O 14	-	-
O 15	-	-
O 16	-	-
O 17	-	-
O 18	-	-
O 19	-	-
O 20	-	-
T 1	0.4336	0.0170
T 2	-	0.0070
T 3	-	-
T 4	-	-
T 5	-	-
T 6	-	-
T 7	-	-
T 8	-	-0.0009
T 9	-0.0360	-
T 10	-	0.0024
T 11	-	-
T 12	-	0.009
T13	-	-
T14	-	0.0022
T15	0.2455	0.0013
T16	-	-
T17	-	-
T18	-	-
T19	-	-
T20	0.0665	-
T21	-	-
T22	-	-

T23	-	-
T24	-	-
T25	-	-
T26	-	-
T27	-	-
T28	-	-
T29	-	-
T30	-	-

*L.Semidey-Flecha and D.S. Sholl, J.Chem. Phys. **128** (2008).

Table B.6: O binding site and ZPE energies for $Pd_{85}Au_{15}$

O-parameters	E_b (eV)	ZPE (ev)
E_o	-0.0995	0.0038
1	0.0353	0.0552
2	0	0
3	0.1491	0.2387
4	0	0
5	0	0
6	0	0
7	-0.0254	0.0479
8	0.1120	0.0024
9	0	0
10	0	0
11	0	0
12	0	0
13	0	0
14	0	0
15	0	0
16	0	0
17	-0.0056	-0.0039
18	0	0
19	0	0
20	0	0

Table B.7:T binding site and ZPE energies for $Pd_{85}Au_{15}$

T-parameters	E_b (eV)	ZPE (ev)
E_o	0.8914	0.1913
1	0.4974	0.0049
2	0	0
3	0	0
4	0	0
5	0	0
6	0	0
7	0.0209	0.0046
8	0	0
9	0	0
10	0	0
11	0	0
12	0	0
13	0	0
14	0	0
15	0.0451	0.0040
16	0	0
17	0	0
18	0	0
19	0	0
20	0	0
21	0	0
22	0.0105	-0.0003
23	0	0
24	0	0
25	0	0
26	0.0029	0.0002
27	0	0
28	0.0015	0
29	0	0
30	0	0

Table B.8: Binding energy and ZPE of H in Transition State sites in $Pd_{85}Au_{15}$

	E_b	ZPE
E_o	3.256	0.3427
O 1	-	-0.0143
O 2	-	-
O 3	-	-
O 4	-	-
O 5	1.4532	-
O 6	-	-
O 7	-	-
O 8	-	-
O 9	-	-
O 10	-	-
O 11	-	-
O 12	-0.032	-
O 13	-	-
O 14	-	-
O 15	-	-
O 16	-	-
O 17	-	-
O 18	-	-
O 19	-	-
O 20	-	-
T 1	0.4236	0.0570
T 2	-	0.6070
T 3	-	-
T 4	-	-
T 5	-	-
T 6	-	-
T 7	-	-
T 8	-	-0.00323
T 9	-0.023	-
T 10	-	0.0644
T 11	-	-
T 12	0.435	0.069
T13	-	-
T14	-	0.0122
T15	0.2555	0.0313
T16	-	-
T17	-	-
T18	-	-
T19	-	-
T20	0.4665	-
T21	-	-
T22	-	-

Table B.8 continued

T23	-	-
T24	-	-
T25	-	-
T26	-	-
T27	-	-
T28	-	-
T29	-	-
T30	-	-

APPENDIX C

SRO AND H/M AS A FUNCTION OF H_2 PRESSURE

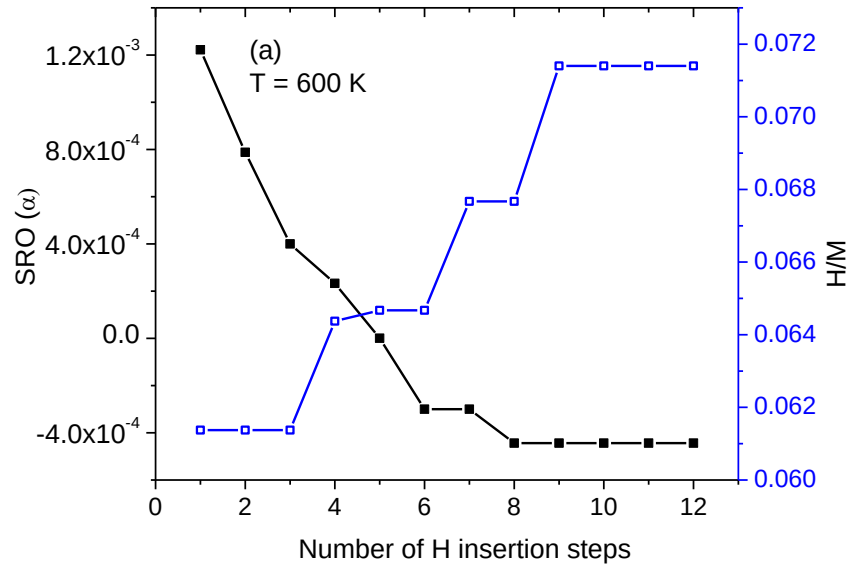

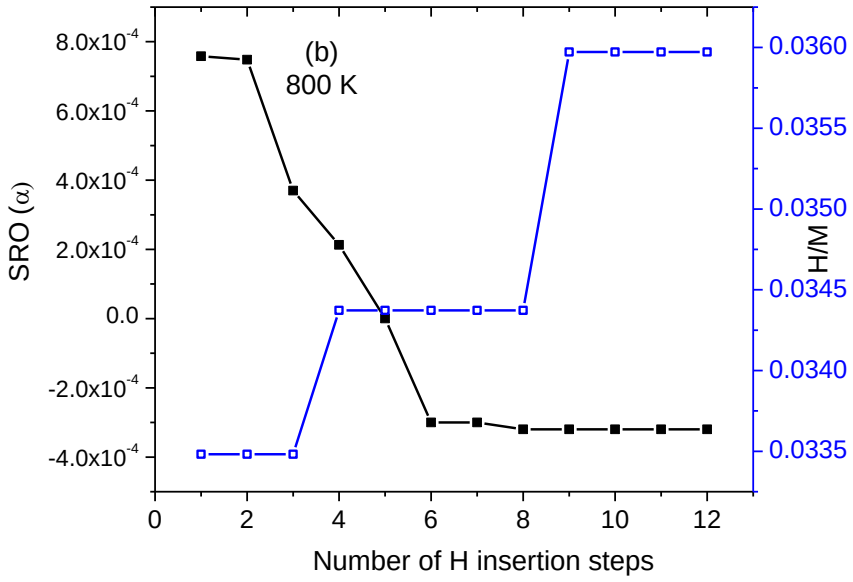

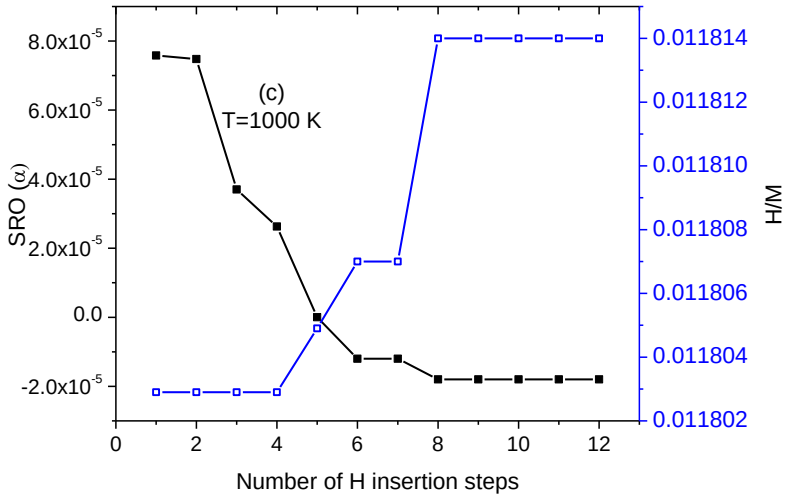
(c)
T=1000 K
SRO (α)
H/M
Number of H insertion steps

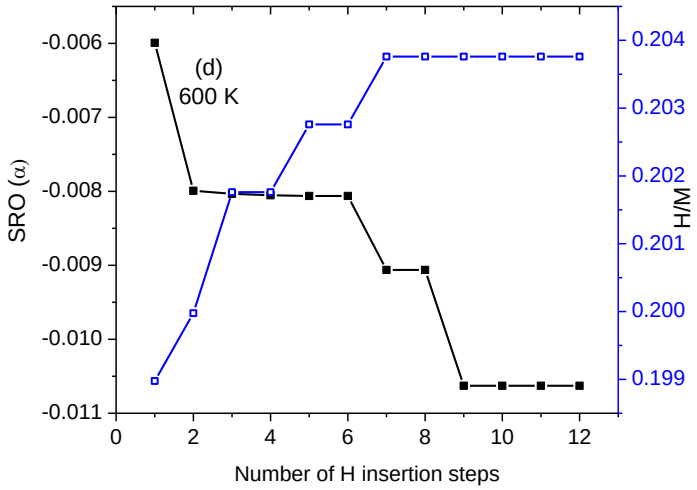
(d)
600 K
SRO (α)
H/M
Number of H insertion steps

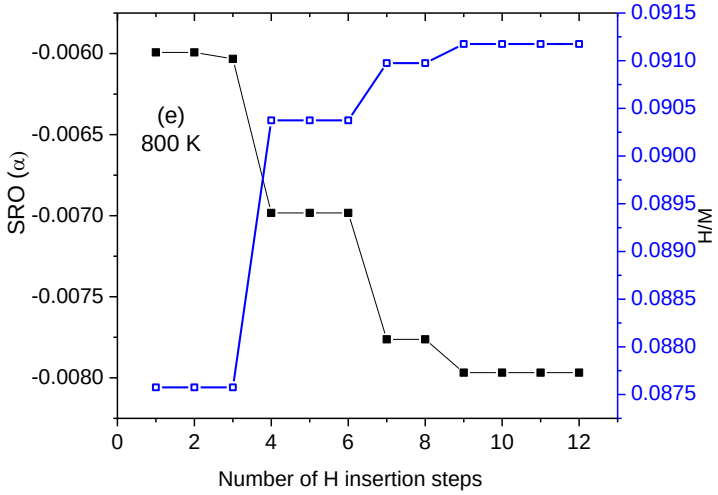
(e)
800 K
SRO (α)
H/M
Number of H insertion steps

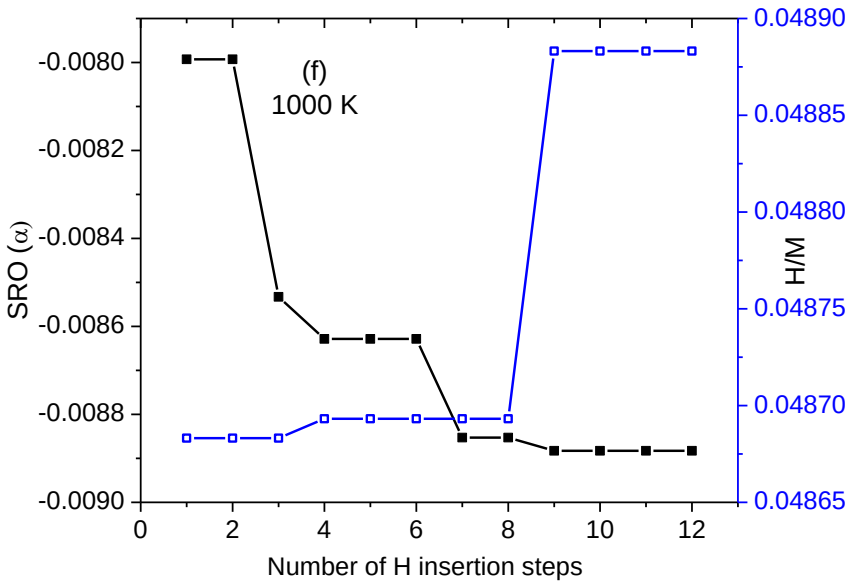

Figure C.15: SRO and H/M as a function of H insertion steps at P H_2=0.01 atm for $Pd_{96}Au_4$ at (a) 600 K (b) 800K and (c) 1000 K and for $Pd_{85}Au_{15}$ at (d) 600 K (e) 800 K (f) 1000 K

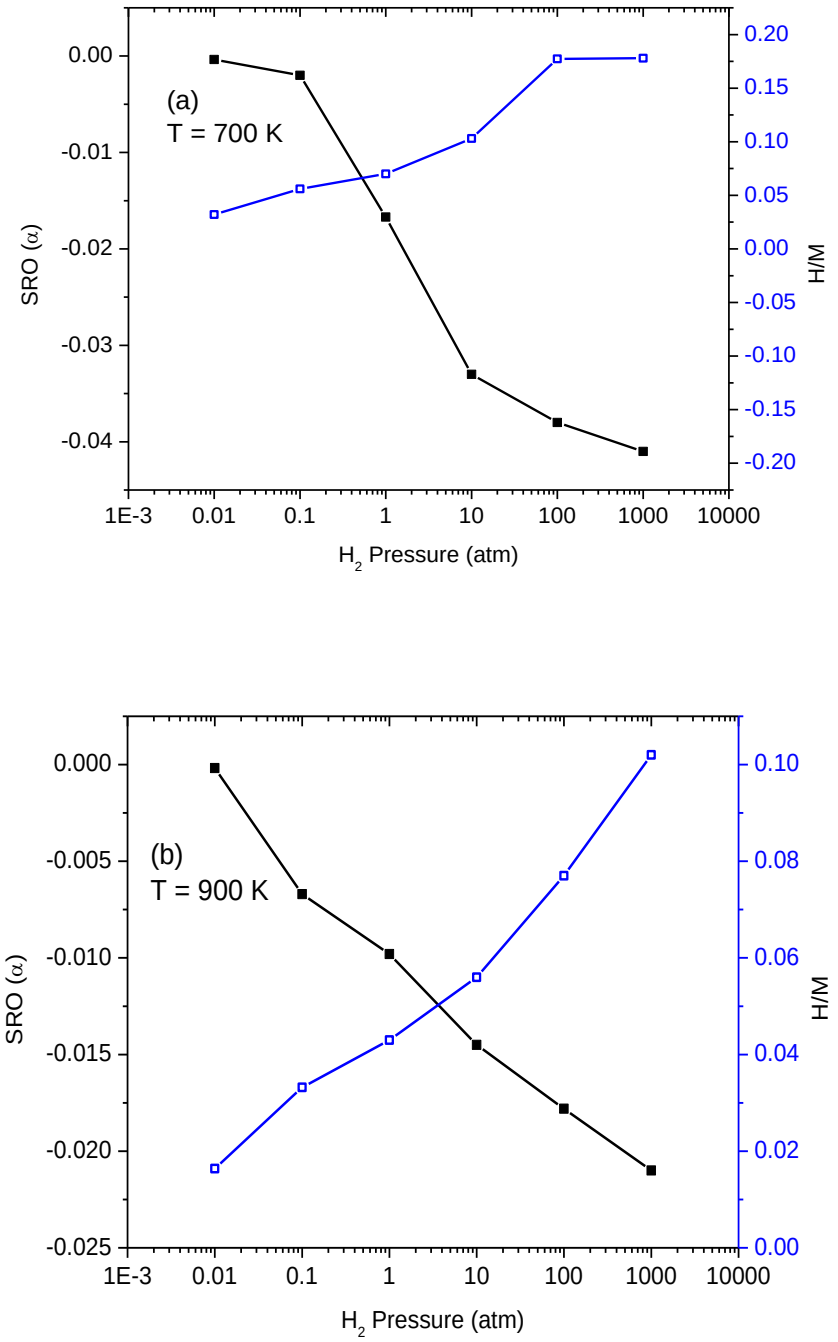

Figure C.16: SRO and H_2 loadings (H/M) as a function of hydrogen pressure for $Pd_{96}Au_4$ at (a) 700 K and (b) 900 K. The filled squares represent the SRO and the open squares are the hydrogen loadings.

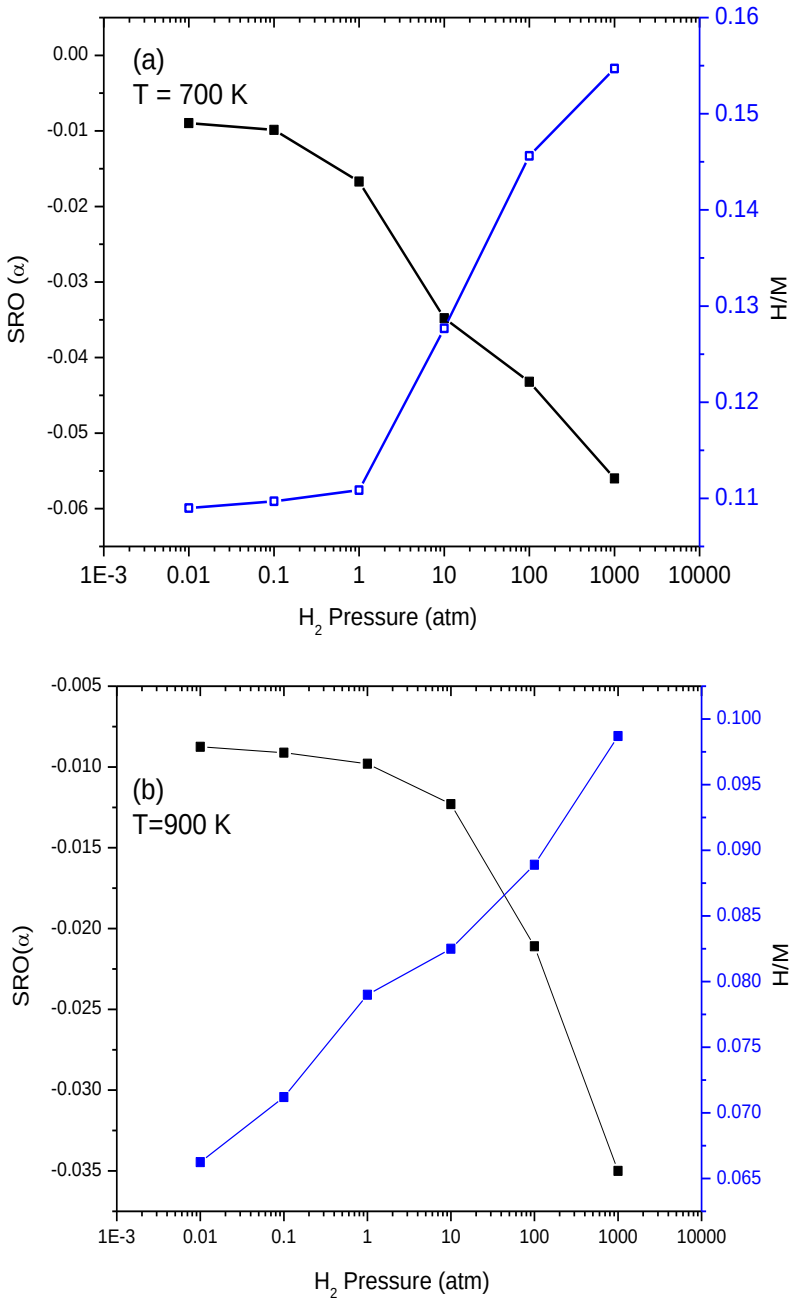

Figure C.3: SRO and H_2 loadings (H/M) as a function of hydrogen pressure for $Pd_{85}Au_{15}$ at (a) 700 K and (b) 900 K. The filled squares represent the SRO and the open squares are the hydrogen loadings.

APPENDIX D

THERMODYNAMIC CORRECTION FACTORS

a.

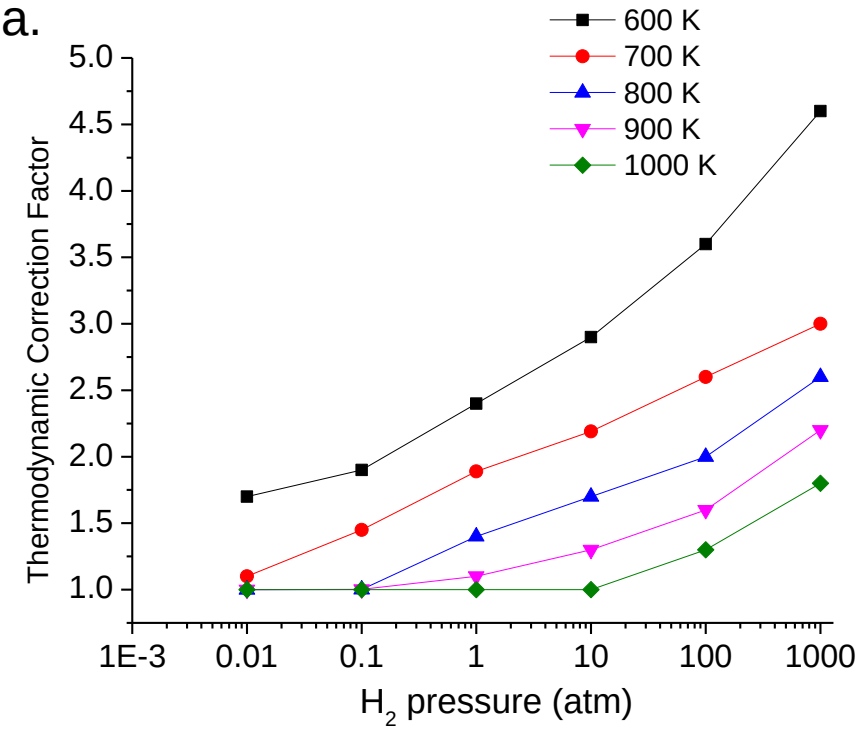

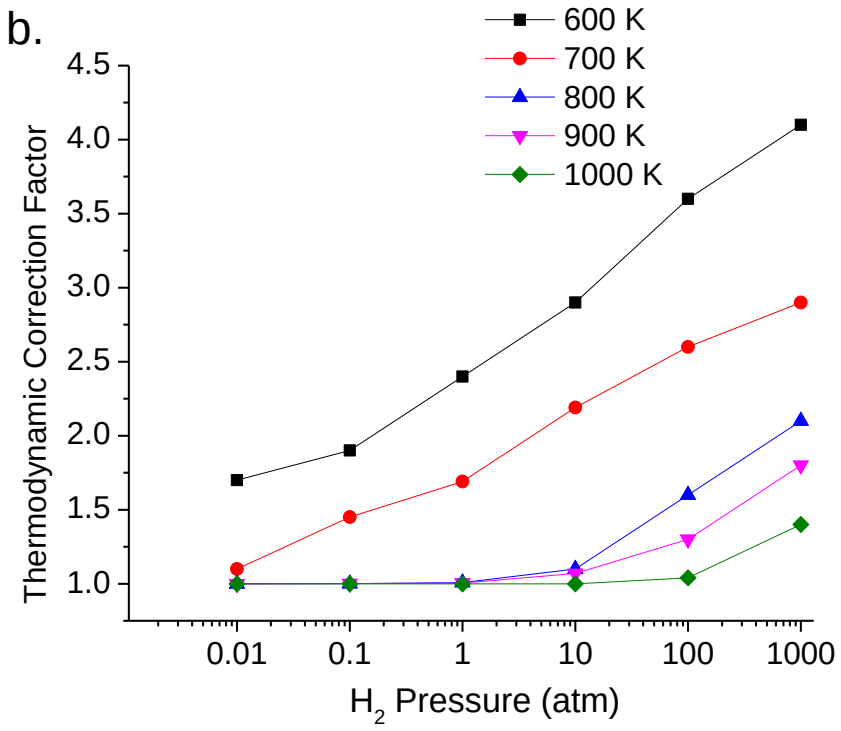

Figure D.1: Thermodynamic Correction Factors of a) $Pd_{96}Au_4$ b) $Pd_{85}Au_{15}$ as a function of H_2 pressure at various temperatures.

APPENDIX E

Figure E.1: Solubility (H/M) of hydrogen at 600 K and 1 atm H_2 in intermetallics belonging to a specific space group. Each data point is labeled by the respective intermetallic. The solubility (H/M) for pure Pd computed with the same methods is shown as a horizontal solid line for comparison. The volume/metal atom for pure Pd is 15.9 Å^3. The black solid line and the red dashed line show the favorable solubility range used to screen candidates (10^{-1}-10^{-5} H/M). Intermetallics belonging to 14 space groups are shown here, with the identity of the space group indicated on each figure.

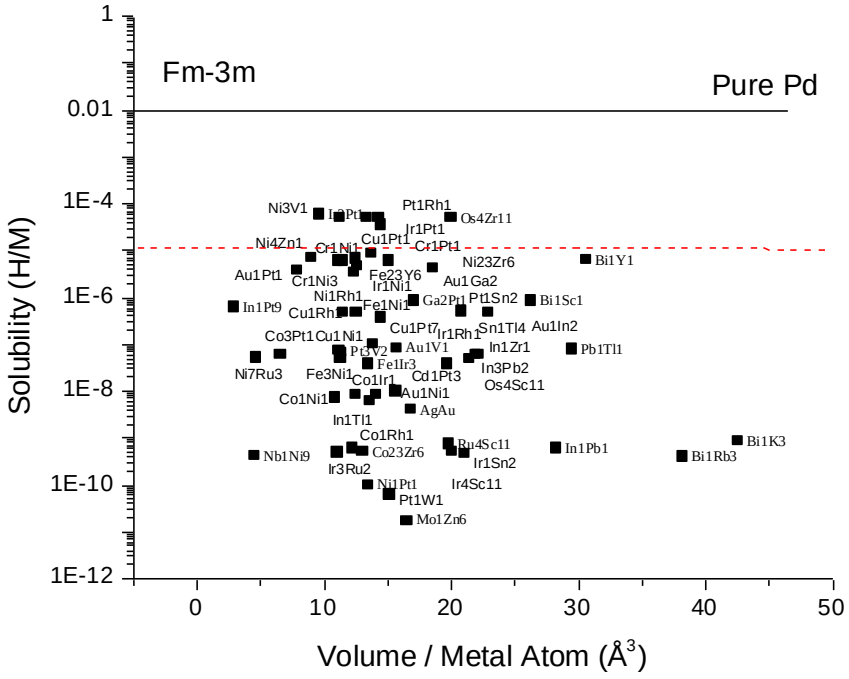

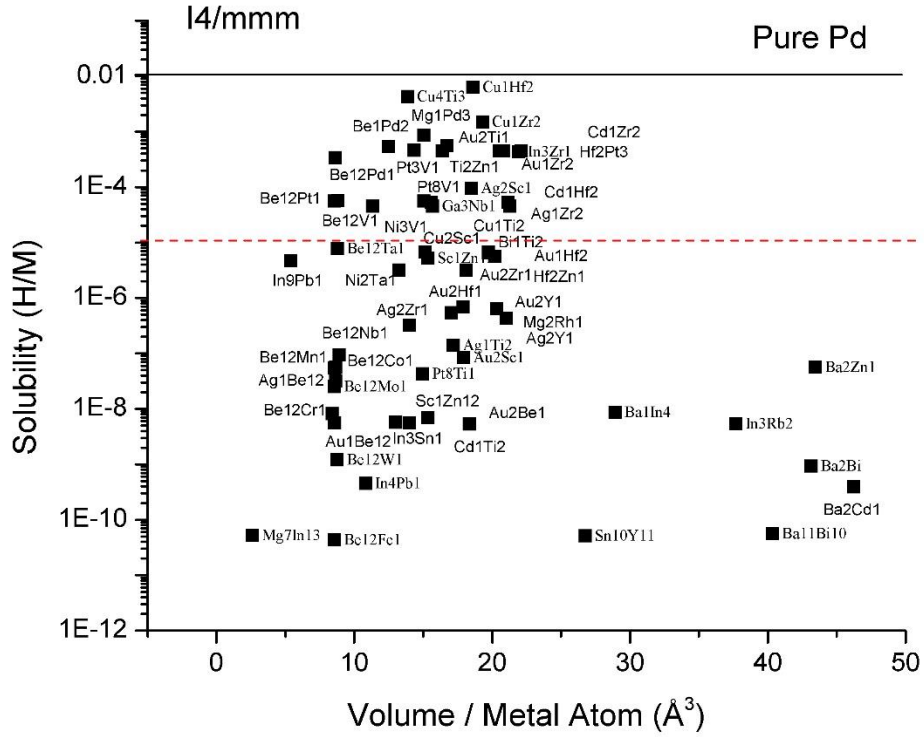
I4/mmm
Pure Pd
Solubility (H/M)
Volume / Metal Atom (Å3)
0.01
1E-4
1E-6
1E-8
1E-10
1E-12
0
10
20
30
40
50
Cu1Hf2
Cu4Ti3
Mg1Pd3
Be1Pd2
Cu1Zr2
Au2Ti1
Cd1Zr2
In3Zr1
Hf2Pt3
Be12Pd1
Pt3V1
Ti2Zn1
Au1Zr2
Pt8V1
Ag2Sc1
Cd1Hf2
Be12Pt1
Ga3Nb1
Ag1Zr2
Be12V1
Ni3V1
Cu1Ti2
Cu2Sc1
Bi1Ti2
Be12Ta1
Sc1Zn1
Au1Hf2
In9Pb1
Ni2Ta1
Au2Zr1
Hf2Zn1
Au2Hf1
Au2Y1
Ag2Zr1
Mg2Rh1
Be12Nb1
Ag1Ti2
Ag2Y1
Be12Mn1
Be12Co1
Au2Sc1
Ba2Zn1
Ag1Be12
Be12Mo1
Pt8Ti1
Sc1Zn12
Be12Cr1
Au2Be1
Ba1In4
In3Rb2
Au1Be12
In3Sn1
Cd1Ti2
Be12W1
Ba2Bi
In4Pb1
Ba2Cd1
Mg7In13
Be12Fe1
Sn10Y11
Ba11Bi10

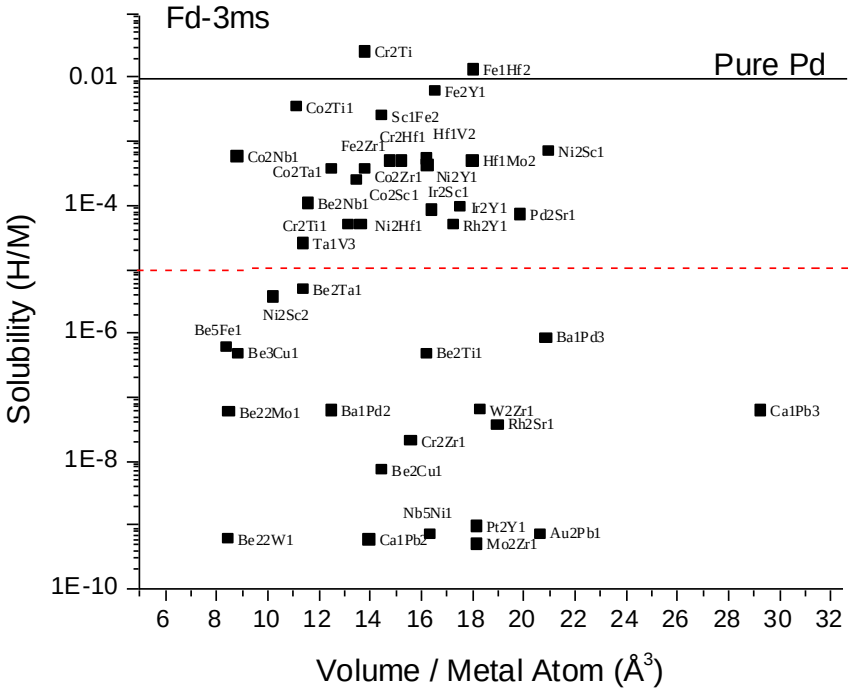
Fd-3ms
Pure Pd
Solubility (H/M)
Volume / Metal Atom (Å3)
0.01
1E-4
1E-6
1E-8
1E-10
6
8
10
12
14
16
18
20
22
24
26
28
30
32
Cr2Ti
Fe1Hf2
Fe2Y1
Co2Ti1
Sc1Fe2
Cr2Hf1
Hf1V2
Fe2Zr1
Co2Nb1
Ni2Sc1
Co2Ta1
Co2Zr1
Hf1Mo2
Ni2Y1
Co2Sc1
Ir2Sc1
Be2Nb1
Ir2Y1
Pd2Sr1
Cr2Ti1
Ni2Hf1
Rh2Y1
Ta1V3
Be2Ta1
Ni2Sc2
Be5Fe1
Ba1Pd3
Be3Cu1
Be2Ti1
Be22Mo1
Ba1Pd2
W2Zr1
Ca1Pb3
Rh2Sr1
Cr2Zr1
Be2Cu1
Nb5Ni1
Pt2Y1
Au2Pb1
Be22W1
Ca1Pb2
Mo2Zr1

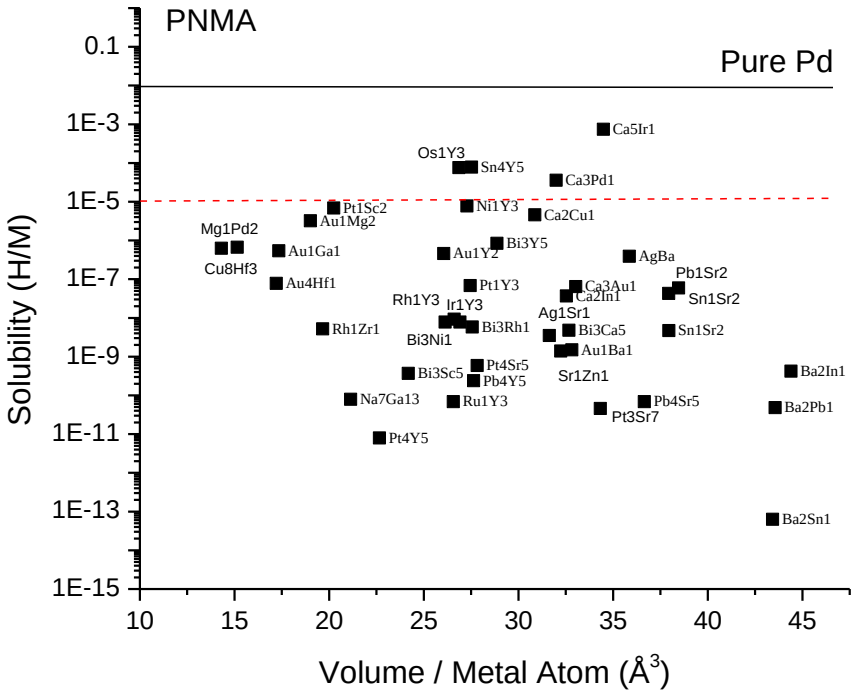
PNMA
Pure Pd
Solubility (H/M)
Volume / Metal Atom (Å3)
0.1
1E-3
1E-5
1E-7
1E-9
1E-11
1E-13
1E-15
10
15
20
25
30
35
40
45
Ca5Ir1
Os1Y3
Sn4Y5
Ca3Pd1
Pt1Sc2
Ni1Y3
Ca2Cu1
Au1Mg2
Mg1Pd2
Au1Ga1
Au1Y2
Bi3Y5
AgBa
Cu8Hf3
Au4Hf1
Pt1Y3
Ca3Au1
Pb1Sr2
Ca2In1
Sn1Sr2
Rh1Y3
Ir1Y3
Ag1Sr1
Rh1Zr1
Bi3Rh1
Bi3Ca5
Sn1Sr2
Bi3Ni1
Au1Ba1
Pt4Sr5
Bi3Sc5
Sr1Zn1
Ba2In1
Pb4Y5
Na7Ga13
Ru1Y3
Pb4Sr5
Ba2Pb1
Pt3Sr7
Pt4Y5
Ba2Sn1

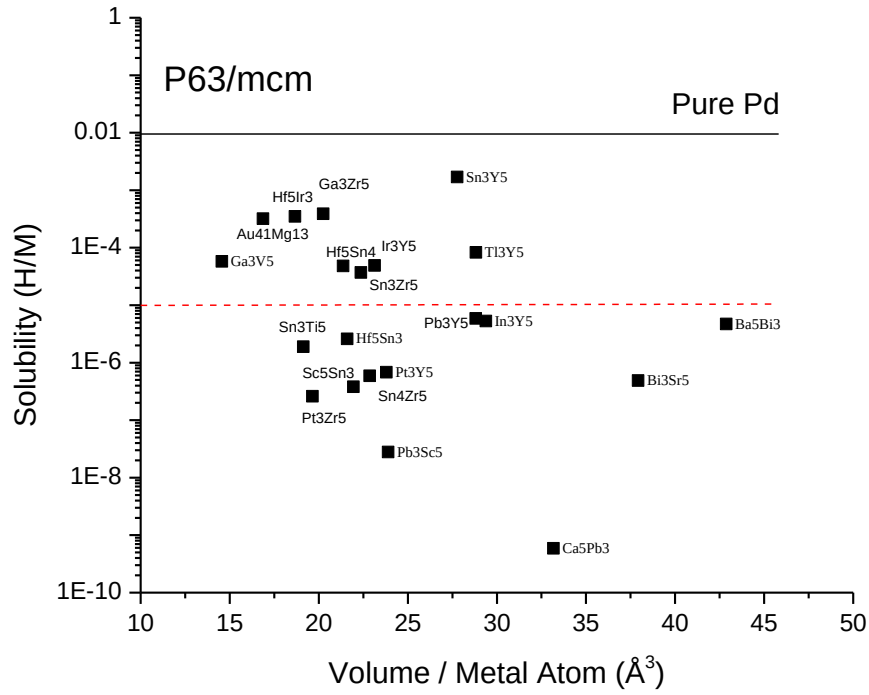
P63/mcm
Pure Pd
Solubility (H/M)
Volume / Metal Atom (Å3)
1
0.01
1E-4
1E-6
1E-8
1E-10
10
15
20
25
30
35
40
45
50
Sn3Y5
Ga3Zr5
Hf5Ir3
Au41Mg13
Ga3V5
Hf5Sn4
Ir3Y5
Tl3Y5
Sn3Zr5
Pb3Y5
In3Y5
Ba5Bi3
Sn3Ti5
Hf5Sn3
Sc5Sn3
Pt3Y5
Bi3Sr5
Sn4Zr5
Pt3Zr5
Pb3Sc5
Ca5Pb3

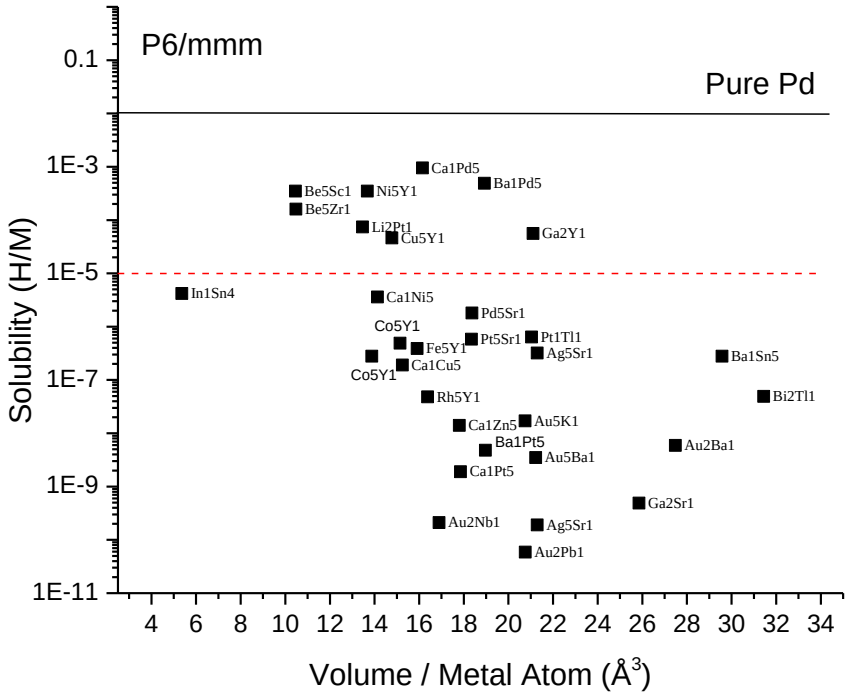
P6/mmm
Pure Pd
Solubility (H/M)
Volume / Metal Atom (Å3)
0.1
1E-3
1E-5
1E-7
1E-9
1E-11
4 6 8 10 12 14 16 18 20 22 24 26 28 30 32 34
Ca1Pd5
Ba1Pd5
Be5Sc1
Ni5Y1
Be5Zr1
Li2Pt1
Cu5Y1
Ga2Y1
In1Sn4
Ca1Ni5
Pd5Sr1
Co5Y1
Pt5Sr1
Pt1Tl1
Fe5Y1
Ag5Sr1
Ba1Sn5
Co5Y1
Ca1Cu5
Rh5Y1
Bi2Tl1
Ca1Zn5
Au5K1
Ba1Pt5
Au2Ba1
Au5Ba1
Ca1Pt5
Ga2Sr1
Au2Nb1
Ag5Sr1
Au2Pb1

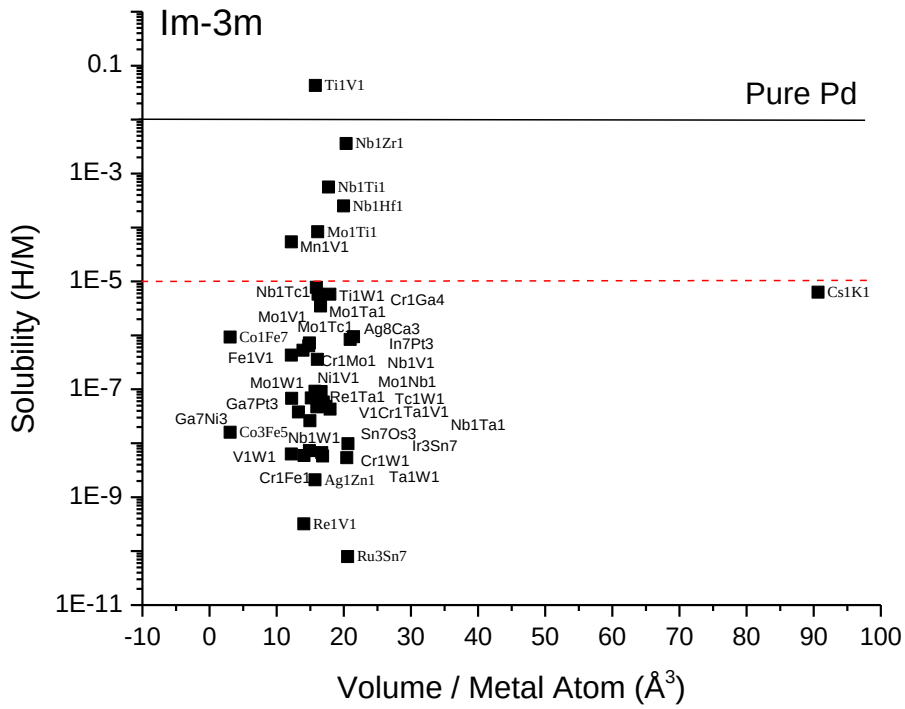
Im-3m
Pure Pd
Solubility (H/M)
Volume / Metal Atom (Å3)
0.1
1E-3
1E-5
1E-7
1E-9
1E-11
-10 0 10 20 30 40 50 60 70 80 90 100
Ti1V1
Nb1Zr1
Nb1Ti1
Nb1Hf1
Mo1Ti1
Mn1V1
Nb1Tc1
Ti1W1
Cr1Ga4
Mo1Ta1
Mo1V1
Mo1Tc1
Ag8Ca3
Co1Fe7
In7Pt3
Fe1V1
Cr1Mo1
Nb1V1
Mo1W1
Ni1V1
Mo1Nb1
Ga7Pt3
Re1Ta1
Tc1W1
V1Cr1Ta1V1
Ga7Ni3
Nb1Ta1
Co3Fe5
Nb1W1
Sn7Os3
Ir3Sn7
V1W1
Cr1W1
Cr1Fe1
Ag1Zn1
Ta1W1
Re1V1
Ru3Sn7
Cs1K1

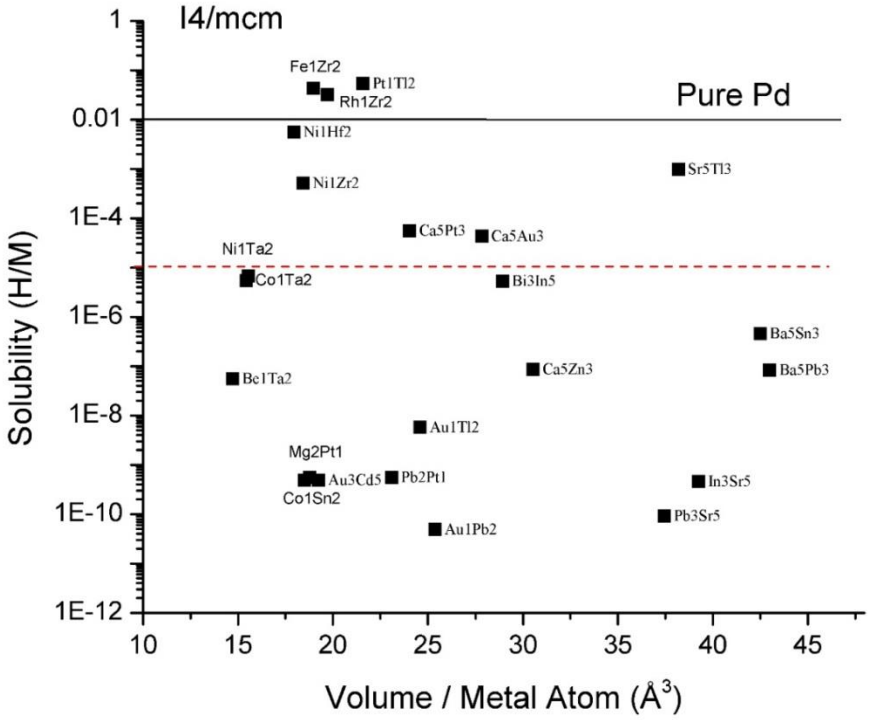
I4/mcm
Pure Pd
Fe1Zr2
Pt1Tl2
Rh1Zr2
Ni1Hf2
Sr5Tl3
Ni1Zr2
Ca5Pt3
Ca5Au3
Ni1Ta2
Co1Ta2
Bi3In5
Ba5Sn3
Ca5Zn3
Ba5Pb3
Be1Ta2
Au1Tl2
Mg2Pt1
Au3Cd5
Pb2Pt1
In3Sr5
Co1Sn2
Pb3Sr5
Au1Pb2
Solubility (H/M)
Volume / Metal Atom (Å3)

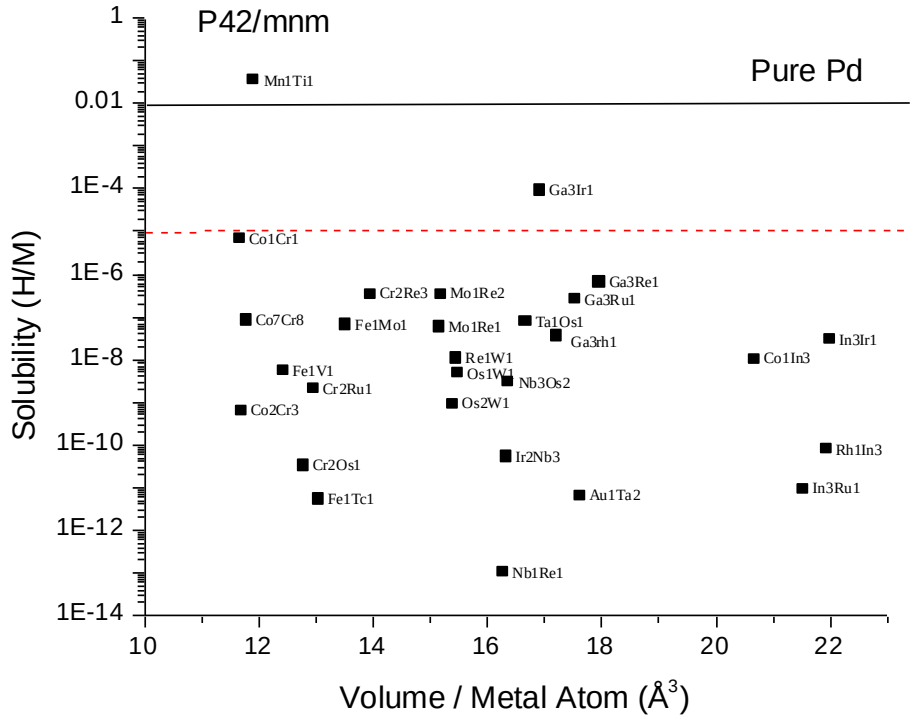
P42/mnm
Pure Pd
Mn1Ti1
Ga3Ir1
Co1Cr1
Ga3Re1
Cr2Re3
Mo1Re2
Ga3Ru1
Co7Cr8
Fe1Mo1
Mo1Re1
Ta1Os1
Ga3rh1
In3Ir1
Re1W1
Co1In3
Fe1V1
Os1W1
Nb3Os2
Cr2Ru1
Co2Cr3
Os2W1
Rh1In3
Ir2Nb3
Cr2Os1
In3Ru1
Au1Ta2
Fe1Tc1
Nb1Re1
Solubility (H/M)
Volume / Metal Atom (Å3)

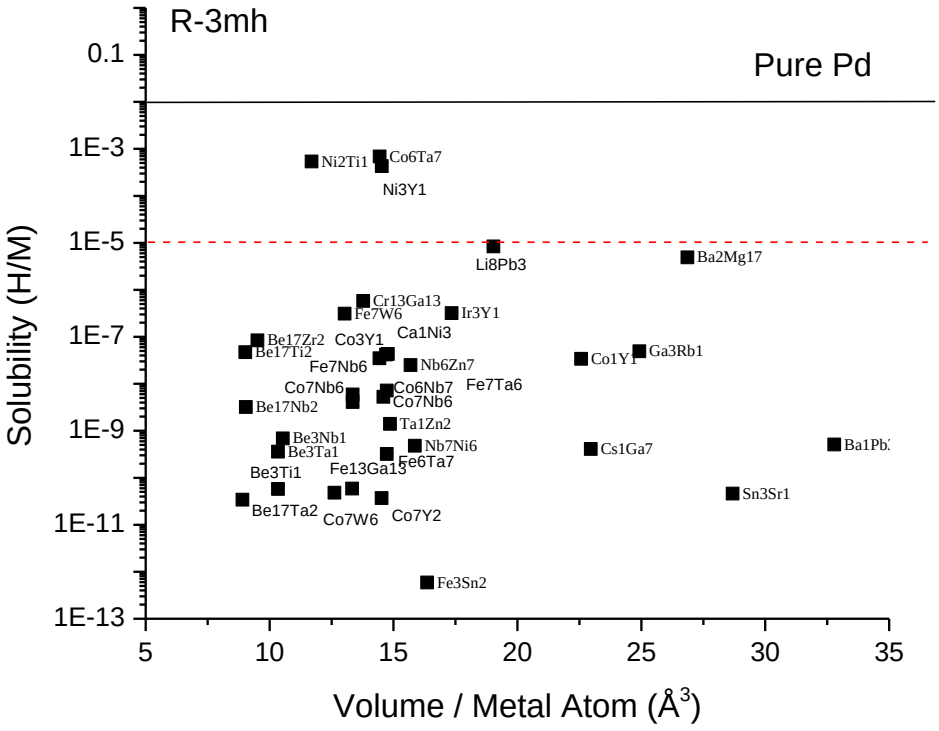
R-3mh
Pure Pd
Solubility (H/M)
Volume / Metal Atom (Å3)
0.1
1E-3
1E-5
1E-7
1E-9
1E-11
1E-13
5
10
15
20
25
30
35
Ni2Ti1
Co6Ta7
Ni3Y1
Li8Pb3
Ba2Mg17
Cr13Ga13
Fe7W6
Ir3Y1
Be17Zr2
Co3Y1
Ca1Ni3
Be17Ti2
Fe7Nb6
Nb6Zn7
Co1Y1
Ga3Rb1
Co7Nb6
Co6Nb7
Fe7Ta6
Co7Nb6
Be17Nb2
Ta1Zn2
Be3Nb1
Be3Ta1
Nb7Ni6
Cs1Ga7
Ba1Pb1
Be3Ti1
Fe13Ga13
Fe6Ta7
Sn3Sr1
Be17Ta2
Co7W6
Co7Y2
Fe3Sn2

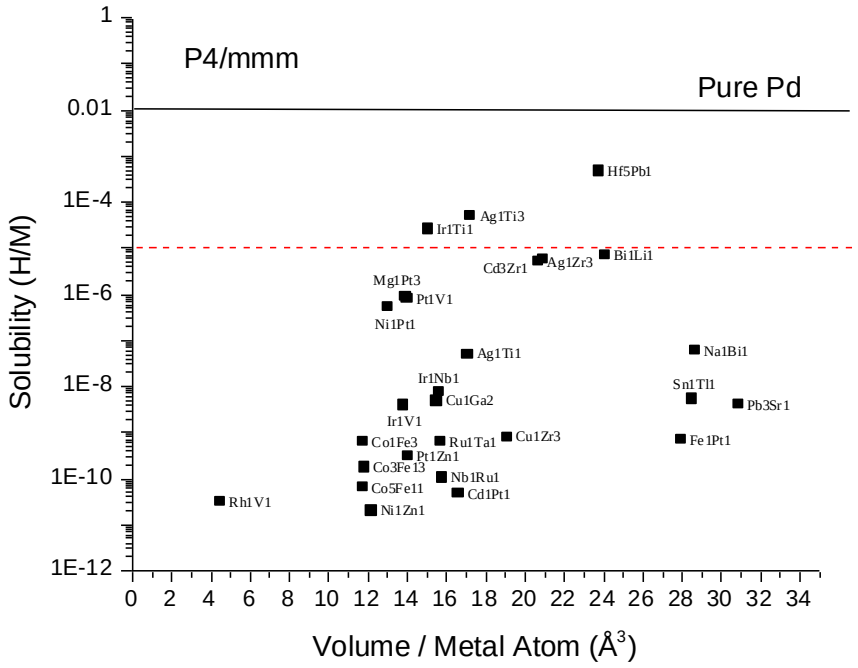
P4/mmm
Pure Pd
Solubility (H/M)
Volume / Metal Atom (Å3)
1
0.01
1E-4
1E-6
1E-8
1E-10
1E-12
0
2
4
6
8
10
12
14
16
18
20
22
24
26
28
30
32
34
Hf5Pb1
Ag1Ti3
Ir1Ti1
Bi1Li1
Cd3Zr1
Ag1Zr3
Mg1Pt3
Pt1V1
Ni1Pt1
Ag1Ti1
Na1Bi1
Ir1Nb1
Sn1Tl1
Cu1Ga2
Pb3Sr1
Ir1V1
Co1Fe3
Ru1Ta1
Cu1Zr3
Fe1Pt1
Pt1Zn1
Co3Fe13
Nb1Ru1
Co5Fe11
Cd1Pt1
Rh1V1
Ni1Zn1

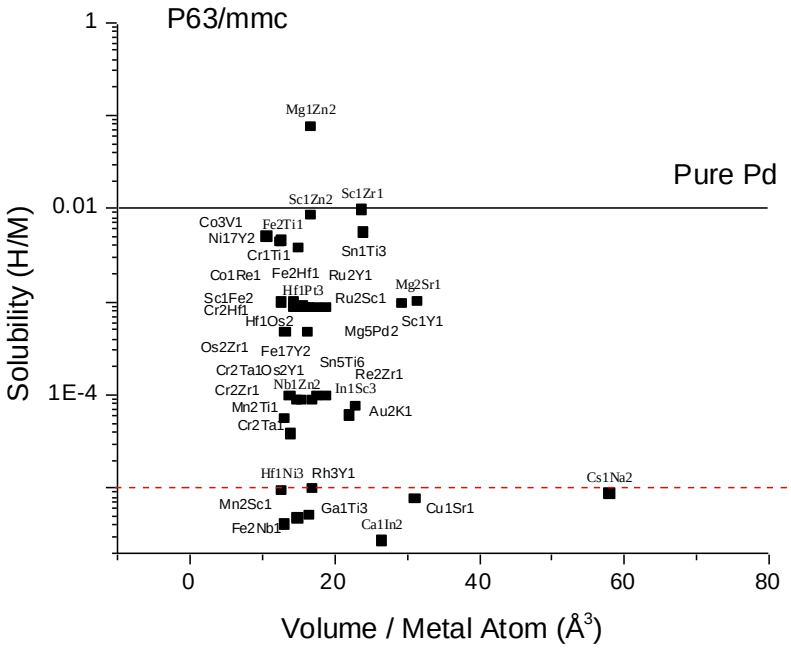
P63/mmc
Pure Pd
Solubility (H/M)
Volume / Metal Atom (Å3)
1
0.01
1E-4
0
20
40
60
80
Mg1Zn2
Sc1Zn2
Sc1Zr1
Co3V1
Fe2Ti1
Ni17Y2
Cr1Ti1
Sn1Ti3
Co1Re1
Fe2Hf1
Ru2Y1
Mg2Sr1
Sc1Fe2
Hf1Pt3
Ru2Sc1
Cr2Hf1
Hf1Os2
Sc1Y1
Mg5Pd2
Os2Zr1
Fe17Y2
Sn5Ti6
Cr2Ta1Os2Y1
Re2Zr1
Cr2Zr1
Nb1Zn2
In1Sc3
Mn2Ti1
Au2K1
Cr2Ta1
Hf1Ni3
Rh3Y1
Cs1Na2
Mn2Sc1
Ga1Ti3
Cu1Sr1
Fe2Nb1
Ca1In2

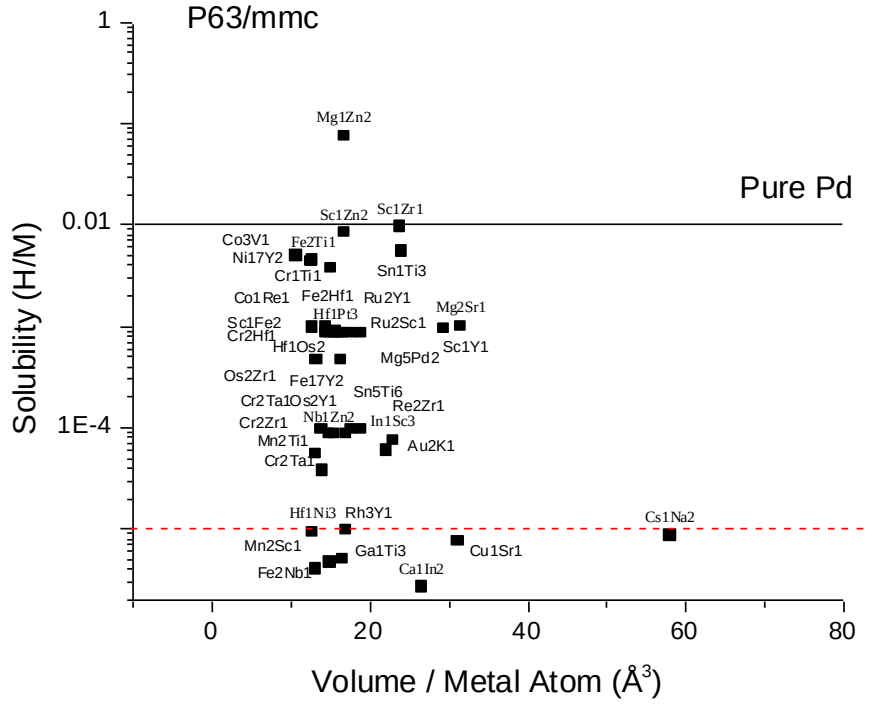
P63/mmc
Pure Pd
Solubility (H/M)
Volume / Metal Atom (Å3)
1
0.01
1E-4
0
20
40
60
80
Mg1Zn2
Sc1Zn2
Sc1Zr1
Co3V1
Fe2Ti1
Ni17Y2
Cr1Ti1
Sn1Ti3
Co1Re1
Fe2Hf1
Ru2Y1
Mg2Sr1
Sc1Fe2
Hf1Pt3
Ru2Sc1
Cr2Hf1
Hf1Os2
Sc1Y1
Mg5Pd2
Os2Zr1
Fe17Y2
Sn5Ti6
Cr2Ta1Os2Y1
Re2Zr1
Cr2Zr1
Nb1Zn2
In1Sc3
Mn2Ti1
Au2K1
Cr2Ta1
Hf1Ni3
Rh3Y1
Cs1Na2
Mn2Sc1
Ga1Ti3
Cu1Sr1
Fe2Nb1
Ca1In2

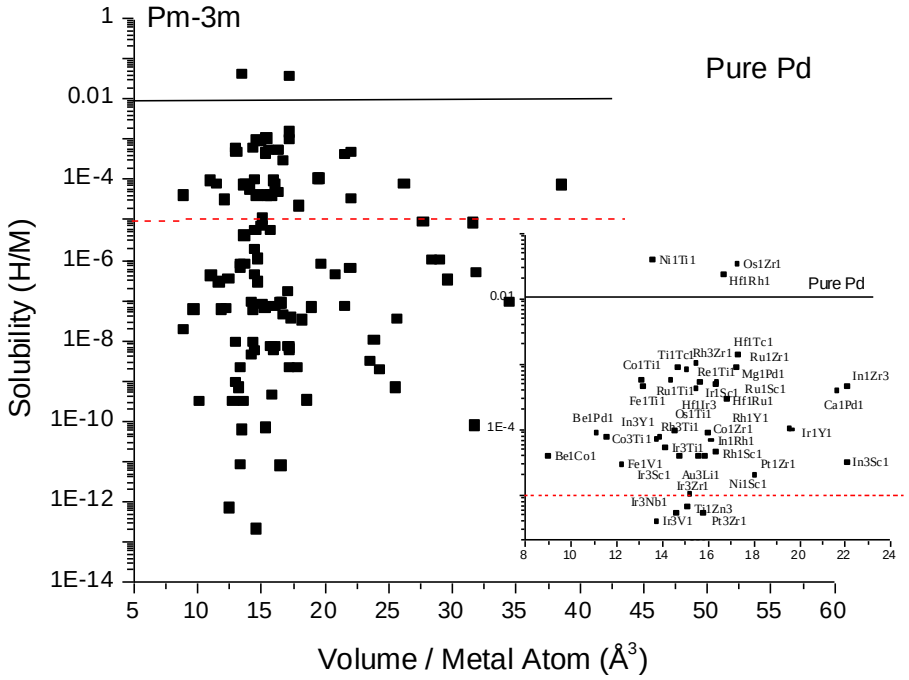
Pm-3m
Pure Pd
Solubility (H/M)
Volume / Metal Atom (Å3)
1
0.01
1E-4
1E-6
1E-8
1E-10
1E-12
1E-14
5
10
15
20
25
30
35
40
45
50
55
60
Ni1Ti1
Os1Zr1
Hf1Rh1
Pure Pd
Hf1Tc1
Ti1Tc1
Rh3Zr1
Ru1Zr1
Co1Ti1
Re1Ti1
Mg1Pd1
In1Zr3
Ru1Ti1
Ir1Sc1
Ru1Sc1
Fe1Ti1
Hf1Ir3
Hf1Ru1
Ca1Pd1
Os1Ti1
Be1Pd1
In3Y1
Rh3Ti1
Rh1Y1
Co1Zr1
Co3Ti1
In1Rh1
Ir1Y1
Ir3Ti1
Be1Co1
Rh1Sc1
Fe1V1
Pt1Zr1
In3Sc1
Ir3Sc1
Au3Li1
Ir3Zr1
Ni1Sc1
Ir3Nb1
Ti1Zn3
Ir3V1
Pt3Zr1
8
10
12
14
16
18
20
22
24

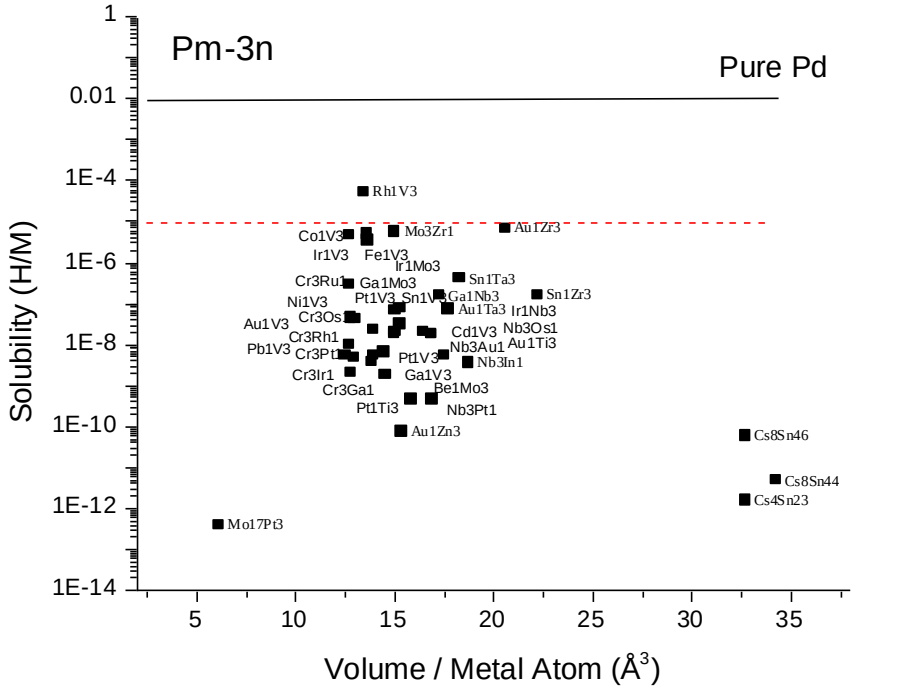
Pm-3n
Pure Pd
Solubility (H/M)
Volume / Metal Atom (Å3)
1
0.01
1E-4
1E-6
1E-8
1E-10
1E-12
1E-14
5
10
15
20
25
30
35
Rh1V3
Au1Zr3
Mo3Zr1
Co1V3
Ir1V3
Fe1V3
Ir1Mo3
Sn1Ta3
Cr3Ru1
Ga1Mo3
Sn1Zr3
Pt1V3
Sn1V3
Ga1Nb3
Ni1V3
Au1Ta3
Ir1Nb3
Cr3Os
Au1V3
Cd1V3
Nb3Os1
Cr3Rh1
Nb3Au1
Au1Ti3
Pb1V3
Cr3Pt1
Pt1V3
Nb3In1
Cr3Ir1
Ga1V3
Be1Mo3
Cr3Ga1
Pt1Ti3
Nb3Pt1
Au1Zn3
Cs8Sn46
Cs8Sn44
Cs4Sn23
Mo17Pt3

Table E.1: List of all intermetallics considered in this work ordered by space group and decreasing H/M at 1 atm H_2 and 600 K. Materials with binding energies < -0.3 eV are not listed below.

Space group	Material	H/M at 600 K , 1 atm H_2
Cmcm		
	Pt2Ta1	6.40E-04
	Rh5Zr3	5.40E-04
	Ir1Zr1	4.30E-04
	Ni1Zr1	4.30E-04
	Hf1Ni1	2.30E-04
	Pb2Y1	4.50E-05
	Ti1Zn16	4.50E-05
	Ba1Pd1	2.40E-05
	Nb1Zn16	5.60E-06
	Ba1Sn1	5.40E-06
	Ag1Ca1	3.40E-06
	Ba1Zn5	4.50E-07
	Au1Ca1	2.30E-07
	Ba1In1	2.30E-07
	Co1Zr3	1.60E-07
	Au1Y1	1.00E-07
	Ag7Ca2	6.70E-08
	In5Y3	6.70E-08
	Ba3Sn5	6.50E-08
	Pb1Sr1	5.70E-08
	Sr3Tl5	4.50E-08
	Fe1Zr3	1.90E-08
	Bi1Zr1	6.70E-09
	Sn4Sr1	5.60E-09
	Na9Sn4	5.30E-09
	Cd7Sc1	4.50E-09
	Na5Sn13	3.40E-09
	Sn2Y1	7.80E-10
	Ba1Pb1	4.50E-10
	Sn5Sr3	8.90E-11
Fd3-ms		
	Cr2Ti	0.023
	Fe1Hf2	0.012
	Fe2Y1	0.0056
	Co2Ti1	0.0032
	Sc1Fe2	0.0023

Table E.1 continued

	Ni2Sc1	6.50E-04
	Co2Nb1	5.40E-04
	Hf1V2	4.90E-04
	Fe2Zr1	4.50E-04
	Cr2Hf1	4.50E-04
	Hf1Mo2	4.50E-04
	Ni2Y1	3.80E-04
	Co2Ta1	3.40E-04
	Co2Zr1	3.40E-04
	Co2Sc1	2.30E-04
	Be2Nb1	9.80E-05
	Ir2Y1	8.70E-05
	Ir2Sc1	7.80E-05
	Pd2Sr1	6.70E-05
	Cr2Ti1	4.50E-05
	Ni2Hf1	4.50E-05
	Rh2Y1	4.50E-05
	Ta1V3	2.30E-05
	Be2Ta1	4.50E-06
	Ni2Sc2	3.40E-06
	Ba1Pd3	7.80E-07
	Be5Fe1	5.60E-07
	Be2Ti1	4.50E-07
	Be3Cu1	4.50E-07
	W2Zr1	5.80E-08
	Ca1Pb3	5.70E-08
	Ba1Pd2	5.60E-08
	Be22Mo1	5.40E-08
	Rh2Sr1	3.40E-08
	Cr2Zr1	1.90E-08
	Be2Cu1	6.80E-09
	Pt2Y1	8.60E-10
	Au2Pb1	6.70E-10
	Nb5Ni1	6.70E-10
	Be22W1	5.60E-10
	Ca1Pb2	5.40E-10
	Mo2Zr1	4.60E-10
Fm3-m		
	Ir2Pt1	5.40E-05
	Os4Zr11	4.50E-05
	Pt1Rh1	4.50E-05
	Cu1Pt1	4.50E-05

Table E.1 continued

	Ni3V1	4.50E-05
	Ir1Pt1	3.20E-05
	Cr1Pt1	7.80E-06
	Ni4Zn1	6.50E-06
	Ni23Zr6	6.25E-06
	Bi1Y1	5.70E-06
	Cr1Ni1	5.60E-06
	Cr1Ni3	5.60E-06
	Fe23Y6	5.60E-06
	Ir1Ni1	4.30E-06
	Au1Ga2	3.80E-06
	Au1Pt1	3.40E-06
	Ni1Rh1	3.10E-06
	Bi1Sc1	7.80E-07
	Ga2Pt1	7.80E-07
	In1Pt9	5.60E-07
	Pt1Sn2	4.60E-07
	Fe1Ni1	4.50E-07
	Au1In2	4.50E-07
	Cu1Rh1	4.50E-07
	Cu1Pt7	3.32E-07
	Ir1Rh1	9.40E-08
	Au1V1	7.80E-08
	Pb1Tl1	7.30E-08
	Cu1Ni1	6.70E-08
	Pt3V2	6.30E-08
	In3Pb2	5.70E-08
	Co3Pt1	5.60E-08
	Sn1Tl4	5.60E-08
	Ni7Ru3	4.80E-08
	Fe3Ni1	4.50E-08
	In1Zr1	4.50E-08
	Os4Sc11	3.50E-08
	Fe1Ir3	3.40E-08
	Cd1Pt3	8.90E-09
	Au1Ni1	7.80E-09
	Co1Ir1	7.80E-09
	Co1Ni1	6.70E-09
	In1Tl1	5.60E-09
	AgAu	3.80E-09
	Bi1K3	7.80E-10
	Ru4Sc11	6.80E-10

Table E.1 continued

	Co1Rh1	5.60E-10
	In1Pb1	5.60E-10
	Co23Zr6	4.80E-10
	Ir4Sc11	4.80E-10
	Ir3Ru2	4.50E-10
	Ir1Sn2	4.30E-10
	Nb1Ni9	3.80E-10
	Bi1Rb3	3.70E-10
	Ni1Pt1	9.30E-11
	Pt1W1	5.60E-11
	Mo1Zn6	1.60E-11
I4/mcm		
	Pt1Tl2	0.054
	Fe1Zr2	0.043
	Rh1Zr2	0.032
	Ni1Hf2	0.0056
	Sr5Tl3	9.80E-04
	Ni1Zr2	5.10E-04
	Ca5Pt3	5.60E-05
	Ca5Au3	4.30E-05
	Ni1Ta2	6.70E-06
	Co1Ta2	5.40E-06
	Bi3In5	5.30E-06
	Ba5Sn3	4.60E-07
	Ca5Zn3	8.60E-08
	Ba5Pb3	8.30E-08
	Be1Ta2	5.60E-08
	Au1Tl2	5.70E-09
	Mg2Pt1	5.60E-10
	Pb2Pt1	5.60E-10
	Au3Cd5	4.90E-10
	Co1Sn2	4.90E-10
	In3Sr5	4.60E-10
	Pb3Sr5	9.20E-11
	Au1Pb2	4.90E-11
I4/mmm		
	Cu1Hf2	0.0063
	Cu4Ti3	0.0043
	Cu1Zr2	0.0015
	Be1Pd2	5.40E-04
	Cd1Zr2	4.50E-04
	Ti2Zn1	4.50E-04

Table E.1 continued

	Be12Pd1	3.40E-04
	Ag2Sc1	9.50E-05
	Be12V1	5.70E-05
	Be12Pt1	5.60E-05
	Pt8V1	5.60E-05
	Cd1Hf2	5.30E-05
	Cu1Ti2	5.30E-05
	Ag1Zr2	4.50E-05
	Ni3V1	4.50E-05
	Be12Ta1	7.80E-06
	Bi1Ti2	6.70E-06
	Cu2Sc1	6.70E-06
	Hf2Zn1	6.50E-06
	Hf2Pt3	5.70E-06
	Au1Hf2	5.60E-06
	Sc1Zn12	5.20E-06
	In9Pb1	4.70E-06
	Au2Zr1	3.20E-06
	Ni2Ta1	3.20E-06
	Au2Hf1	6.80E-07
	Au1Zr2	6.40E-07
	Au2Y1	6.30E-07
	Ag2Y1	4.30E-07
	Ag2Zr1	3.20E-07
	Ag1Ti2	1.40E-07
	Be12Nb1	9.30E-08
	Au2Sc1	8.40E-08
	Au2Ti1	8.30E-08
	Pt3V1	5.90E-08
	Be12Mn1	5.60E-08
	Ba2Zn1	5.60E-08
	Be12Co1	5.40E-08
	Pt8Ti1	4.30E-08
	Ag1Be12	3.20E-08
	Be12Mo1	2.50E-08
	Ba1In4	8.60E-09
	Be12Cr1	8.20E-09
	Sc1Zn12	6.90E-09
	In3Sn1	5.70E-09
	Au1Be12	5.60E-09
	Au2Be1	5.60E-09
	In3Rb2	5.40E-09

Table E.1 continued

	Be12W1	1.20E-09
	Ba2Bi	9.30E-10
	In3Zr1	9.10E-10
	In4Pb1	4.50E-10
	Ba2Cd1	3.90E-10
	Ba11Bi10	5.60E-11
	Mg7In13	5.20E-11
	Sn10Y11	5.10E-11
	Be12Fe1	4.30E-11
Im3-m		
	Ti1V1	0.043
	Hf1Ta1	0.023
	Nb1Zr1	0.0036
	Nb1Ti1	5.60E-04
	Ta1Ti1	4.50E-04
	Cr1Ti1	4.30E-04
	Mo1Zr1	4.30E-04
	Hf1Mo1	3.40E-04
	Nb1Hf1	2.50E-04
	Mo1Ti1	8.30E-05
	Mn1V1	5.40E-05
	Nb1Tc1	7.80E-06
	Cs1K1	6.30E-06
	Cr1Ga4	5.80E-06
	Ti1W1	5.80E-06
	Mo1Ta1	3.50E-06
	Ag8Ca3	9.40E-07
	Co1Fe7	9.30E-07
	In7Pt3	8.40E-07
	Mo1Tc1	7.20E-07
	Mo1V1	6.40E-07
	Cr1Mo1	5.30E-07
	Fe1V1	4.30E-07
	Nb1V1	3.60E-07
	Mo1W1	9.20E-08
	Mo1Nb1	9.10E-08
	Tc1W1	6.90E-08
	Ni1V1	6.80E-08
	Ga7Pt3	5.80E-08
	Re1Ta1	4.80E-08
	Ta1V1	4.70E-08
	Nb1Ta1	4.30E-08

Table E.1 continued

	V1Cr1	3.80E-08
	Ga7Ni3	2.60E-08
	Co3Fe5	1.60E-08
	Sn7Os3	9.80E-09
	V1W1	7.30E-09
	Nb1W1	6.70E-09
	Cr1Fe1	6.30E-09
	Cr1W1	5.90E-09
	Ta1W1	5.80E-09
	Ir3Sn7	5.40E-09
	Ag1Zn1	2.10E-09
	Re1V1	3.20E-10
	Ru3Sn7	7.90E-11
P4/mmm		
	Hf5Pb1	4.30E-04
	Ag1Ti3	4.50E-05
	Ir1Ti1	2.40E-05
	Bi1Li1	6.50E-06
	Cd3Zr1	5.40E-06
	Ag1Zr3	4.80E-06
	Mg1Pt3	8.30E-07
	Pt1V1	7.30E-07
	Ni1Pt1	4.80E-07
	Na1Bi1	5.60E-08
	Ag1Ti1	4.60E-08
	Ir1Nb1	6.90E-09
	Sn1Tl1	4.80E-09
	Cu1Ga2	4.30E-09
	Pb3Sr1	3.70E-09
	Ir1V1	3.60E-09
	Cu1Zr3	7.30E-10
	Fe1Pt1	6.50E-10
	Co1Fe3	5.90E-10
	Ru1Ta1	5.80E-10
	Pt1Zn1	2.80E-10
	Co3Fe13	1.60E-10
	Nb1Ru1	9.60E-11
	Co5Fe11	5.90E-11
	Cd1Pt1	4.30E-11
	Rh1V1	2.90E-11
	Ni1Zn1	1.80E-11

Table E.1 continued

P42/mnm		
	Mn1Ti1	0.032
	Ga3Ir1	8.10E-05
	Co1Cr1	5.90E-06
	Ga3Re1	5.80E-07
	Cr2Re3	3.10E-07
	Mo1Re2	3.10E-07
	Ga3Ru1	2.40E-07
	Co7Cr8	7.40E-08
	Ta1Os1	6.80E-08
	Fe1Mo1	5.80E-08
	Mo1Re1	5.20E-08
	Ga3rh1	3.20E-08
	In3Ir1	2.70E-08
	Re1W1	9.40E-09
	Co1In3	9.30E-09
	Fe1V1	4.80E-09
	Os1W1	4.30E-09
	Nb3Os2	2.70E-09
	Cr2Ru1	1.80E-09
	Os2W1	8.30E-10
	Co2Cr3	5.80E-10
	Rh1In3	7.00E-11
	Ir2Nb3	4.70E-11
	Cr2Os1	2.90E-11
	In3Ru1	8.40E-12
	Au1Ta2	5.80E-12
	Fe1Tc1	4.80E-12
	Nb1Re1	9.20E-14
P6/mmm		
	Ca1Pd5	9.50E-04
	Ba1Pd5	4.90E-04
	Be5Sc1	3.50E-04
	Ni5Y1	3.50E-04
	Be5Zr1	1.60E-04
	Li2Pt1	7.40E-05
	Ga2Y1	5.60E-05
	Cu5Y1	4.60E-05
	In1Sn4	4.20E-06
	Ca1Ni5	3.60E-06
	Pd5Sr1	1.80E-06
	Pt1Tl1	6.40E-07

Table E.1 continued

	Pt5Sr1	5.80E-07
	Co5Y1	4.90E-07
	Fe5Y1	3.90E-07
	Ag5Sr1	3.20E-07
	Ba1Sn5	2.80E-07
	Co5Y1	2.80E-07
	Ca1Cu5	1.90E-07
	Bi2Tl1	4.90E-08
	Rh5Y1	4.80E-08
	Au5K1	1.70E-08
	Ca1Zn5	1.40E-08
	Au2Ba1	5.90E-09
	Ba1Pt5	4.80E-09
	Au5Ba1	3.50E-09
	Ca1Pt5	1.90E-09
	Ga2Sr1	4.90E-10
	Au2Nb1	2.10E-10
	Ag5Sr1	1.90E-10
	Au2Pb1	5.90E-11
P63/mcm		
	Sn3Y5	0.0017
	Ga3Zr5	3.90E-04
	Hf5Ir3	3.50E-04
	Au41Mg13	3.20E-04
	Tl3Y5	8.30E-05
	Ga3V5	5.80E-05
	Ir3Y5	4.90E-05
	Hf5Sn4	4.80E-05
	Sn3Zr5	3.70E-05
	Pb3Y5	5.90E-06
	In3Y5	5.30E-06
	Ba5Bi3	4.70E-06
	Hf5Sn3	2.60E-06
	Sn3Ti5	1.90E-06
	Pt3Y5	6.80E-07
	Sc5Sn3	5.90E-07
	Bi3Sr5	4.90E-07
	Sn4Zr5	3.80E-07
	Pt3Zr5	2.60E-07
	Pb3Sc5	2.80E-08
	Ca5Pb3	5.90E-10

Table E.1 continued

P63/mmc		
	Mg1Zn2	0.073
	Sc1Zr1	0.0091
	Sc1Zn2	0.0081
	Sn1Ti3	0.0053
	Co3V1	0.0048
	Fe2Ti1	0.0043
	Ni17Y2	0.0042
	Cr1Ti1	0.0036
	Mg2Sr1	9.60E-04
	Sc1Fe2	9.40E-04
	Co1Re1	9.30E-04
	Sc1Y1	9.20E-04
	Hf1Pt3	8.40E-04
	Fe2Hf1	8.30E-04
	Mg5Pd2	8.30E-04
	Os2Zr1	8.30E-04
	Ru2Sc1	8.30E-04
	Ru2Y1	8.20E-04
	Cr2Hf1	8.20E-04
	Fe17Y2	4.50E-04
	Hf1Os2	4.50E-04
	Os2Y1	9.30E-05
	Sn5Ti6	9.30E-05
	Cr2Ta1	9.20E-05
	Cr2Zr1	8.40E-05
	Nb1Zn2	8.30E-05
	Re2Zr1	8.30E-05
	In1Sc3	7.20E-05
	Au2K1	5.70E-05
	Mn2Ti1	5.30E-05
	Cr2Ta1	3.60E-05
	Rh3Y1	9.30E-06
	Hf1Ni3	9.10E-06
	Cs1Na2	8.30E-06
	Cu1Sr1	7.30E-06
	Ga1Ti3	4.90E-06
	Mn2Sc1	4.50E-06
	Fe2Nb1	3.90E-06
	Ca1In2	2.60E-06
	Tc2Y1	9.40E-07
	Os1Tc1	9.30E-07

Table E.1 continued

	Ni1Tc1	9.20E-07
	Os2Sc1	8.30E-07
	Hf1Mo2	8.20E-07
	Cr2Ti1	7.30E-07
	Re2Y1	7.30E-07
	Ga5Ta6	5.80E-07
	In1Sc2	5.60E-07
	Be2Cr1	5.20E-07
	Co1Mo1	5.10E-07
	Ir1Ru1	4.90E-07
	Ba1Na2	4.30E-07
	Be2V1	4.30E-07
	In2Sr1	4.30E-07
	Bi1Cu1	4.20E-07
	Mg17Sr2	3.60E-07
	Ba1Tl2	1.60E-07
	Ru2Zr1	9.50E-08
	Ti1Zn2	9.40E-08
	Co3Mo1	9.30E-08
	Pt3Ti1	9.30E-08
	Re2Sc1	9.20E-08
	In1Y2	8.30E-08
	Na1Tl1	8.30E-08
	Fe2W1	8.20E-08
	Co1Ru1	8.20E-08
	Os1Re1	7.20E-08
	Sr1Tl2	6.90E-08
	Re1Tc1	6.40E-08
	Cd1Cu2	5.90E-08
	Be2Mo1	4.30E-08
	Be2W1	4.20E-08
	Mg1Ir2	3.20E-08
	Fe3Ga1	9.40E-09
	Cu2In1	9.30E-09
	Ru1Tc1	9.20E-09
	Mo1Rh3	8.50E-09
	Be2Fe1	6.30E-09
	Ga1Ni2	5.70E-09
	Ba1Sn3	5.20E-09
	Ni7Y2	4.30E-09
	Mo1Ni1	3.80E-09
	Be2Mn1	3.20E-09

Table E.1 continued

	Cu3Sn1	9.20E-10
	Ni1Ru1	8.30E-10
	Ta6Zn7	8.30E-10
	Mo1Pt1	7.30E-10
	Pt2Sn3	7.20E-10
	Ir3W1	6.50E-10
	Be17Hf2	6.20E-10
	Mg5Rh2	6.20E-10
	Ga5V6	5.90E-10
	Ir1Tc1	5.30E-10
	Fe2Ta1	4.80E-10
	Mg4Sr1	4.20E-10
	Os1Ru1	3.90E-10
	Bi1In2	3.90E-10
	Cr1Ir1	3.80E-10
	Ni7Sc2	3.10E-10
	Pt1Sn1	9.40E-11
	Ni3Sn2	9.30E-11
	Cd3Sc1	9.20E-11
	In1Ni2	8.30E-11
	Ni1Tl1	8.20E-11
	Fe3Y1	8.20E-11
	Ba1Pt1	5.90E-11
	Co3W1	5.90E-11
	Cs6Rb7	5.90E-11
	Ba1Cu1	5.30E-11
	Co1Os1	5.30E-11
	Cd5Cu2	5.20E-11
	Co1Tc1	5.20E-11
	Cr1Rh1	5.20E-11
	Cu1Sn1	4.90E-11
	Ir9Ru11	4.90E-11
	Mg1Ni2	4.80E-11
	Os1Tc3	4.20E-11
	Ir1Sn1	3.90E-11
	Be2Re1	3.60E-11
	Sn1Ti2	2.90E-11
	Fe2Sn1	2.90E-11
	Hf1Re2	2.80E-11
	Bi1Rh1	2.60E-11
	Au1Sn1	9.40E-12
	Bi1Rb3	9.30E-12

Table E.1 continued

	Cd58Sr13	3.80E-12
	Pt2Re3	9.50E-13
	Fe1Ru1	4.90E-13
	Pb1Pt1	9.60E-14
	Rh1Tc1	9.40E-14
	Rh1Ru1	9.40E-18
Pm3-m		
	Ni1Ti1	0.036
	Os1Zr1	0.032
	Hf1Tc1	0.0013
	Rh3Zr1	9.20E-04
	Ti1Tc1	8.40E-04
	Ru1Zr1	8.40E-04
	Re1Ti1	7.40E-04
	Ru1Ti1	5.30E-04
	Co1Ti1	5.20E-04
	Ir1Sc1	4.80E-04
	Mg1Pd1	4.80E-04
	Ru1Sc1	4.60E-04
	Fe1Ti1	4.30E-04
	In1Zr3	4.10E-04
	Hf1Ir3	3.90E-04
	Ca1Pd1	3.60E-04
	Hf1Ru1	2.60E-04
	Ir1Y1	9.20E-05
	Rh1Y1	9.10E-05
	Os1Ti1	8.90E-05
	Be1Pd1	8.30E-05
	Co1Zr1	8.30E-05
	Rh3Ti1	6.90E-05
	Tl1Y1	6.90E-05
	Co3Ti1	6.80E-05
	In3Y1	6.40E-05
	Cs1Au1	6.30E-05
	In1Rh1	6.30E-05
	Ir3Ti1	5.00E-05
	Rh1Sc1	4.10E-05
	Be1Co1	3.60E-05
	Au3Li1	3.60E-05
	Ni1Sc1	3.60E-05
	Ir3Sc1	3.50E-05
	In3Sc1	2.90E-05

Table E.1 continued

	Fe1V1	2.70E-05
	Pt1Zr1	1.90E-05
	Ir3Zr1	9.20E-06
	Pb3Y1	7.80E-06
	BiTl1	7.30E-06
	Ti1Zn3	5.90E-06
	Pt3Zr1	4.80E-06
	Ir3Nb1	4.70E-06
	Ir3V1	3.60E-06
	Pt3V1	1.60E-06
	Mg1Rh1	9.30E-07
	Na1Pb3	9.10E-07
	Ca3Pb1	8.60E-07
	Tc1V1	7.20E-07
	Ga1Ir1	6.90E-07
	Ag1Sc1	6.80E-07
	Rh1Zn1	5.90E-07
	In1Sc3	5.30E-07
	Cd1Sr1	4.30E-07
	Ir3Ta1	3.80E-07
	Cu1Y1	3.80E-07
	Fe1Ni3	3.60E-07
	Cu3Pt1	2.90E-07
	Mg1Sr1	2.80E-07
	Co1Fe15	2.50E-07
	Rh3Sc1	2.50E-07
	Au1Ti1	1.50E-07
	Nb1Rh3	8.20E-08
	Au1Rb1	7.90E-08
	Hf1Rh1	7.60E-08
	In1Pt3	7.30E-08
	Nb1Zn3	6.90E-08
	Pt1Ti1	6.30E-08
	Cd1Sc1	6.30E-08
	Au1Sc1	5.90E-08
	Pt3Sc1	5.70E-08
	Ni1Zn1	5.40E-08
	Be1Cu1	5.20E-08
	Ga1Ni1	5.20E-08
	Fe1Pt3	4.80E-08
	Pt3Y1	3.70E-08
	Pt1Sc1	3.20E-08

Table E.1 continued

	Cd1Y1	2.90E-08
	Au1Cd1	2.80E-08
	Be1Ni1	1.70E-08
	Mg1Tl1	9.20E-09
	Fe1Ir1	7.90E-09
	Cr1Pt3	7.90E-09
	Tc1Ta1	6.20E-09
	Cu1Sc1	6.10E-09
	Ru1Ta1	6.10E-09
	Ag3Mg1	5.90E-09
	Cu1Zr1	5.20E-09
	Nb1Ru3	5.10E-09
	Nb1Ru1	4.90E-09
	Rh3Ta1	3.80E-09
	Ag1Y1	2.70E-09
	Ag1Mg1	1.90E-09
	Au1Mg1	1.90E-09
	Rh3V1	1.80E-09
	Mg1In3	1.70E-09
	Ni3Pt1	7.90E-10
	Ru1V1	5.90E-10
	Tl3Y1	5.90E-10
	Pt3Sn1	3.80E-10
	Nb1Cd3	2.90E-10
	Be1Rh1	2.80E-10
	Cr1Ir3	2.80E-10
	Fe3Pt1	2.70E-10
	Bi3Sr1	6.80E-11
	Au1Zn1	5.90E-11
	V1Os1	5.20E-11
	Ga1Rh1	7.20E-12
	Pb1Pt3	6.90E-12
	Fe3Ga1	6.10E-13
	Pt3Zn1	1.80E-13
Pm3-n		
	Rh1V3	4.90E-05
	Au1Zr3	6.30E-06
	Mo3Zr1	5.20E-06
	Fe1V3	4.50E-06
	Co1V3	4.10E-06
	Ir1V3	3.10E-06
	Sn1Ta3	3.80E-07

Table E.1 continued

	Cr3Ru1	2.60E-07
	Sn1Zr3	1.50E-07
	Ga1Nb3	1.40E-07
	Ir1Mo3	7.20E-08
	Au1Ta3	6.50E-08
	Ga1Mo3	6.20E-08
	Cr3Os1	4.10E-08
	Ni1V3	3.70E-08
	Sn1V3	2.80E-08
	Pt1V3	2.10E-08
	Au1Ti3	1.90E-08
	Cd1V3	1.90E-08
	Nb3Os1	1.70E-08
	Ir1Nb3	1.70E-08
	Pb1V3	1.60E-08
	Cr3Rh1	9.10E-09
	Au1V3	5.90E-09
	Pt1V3	5.10E-09
	Nb3Au1	5.10E-09
	Cr3Ga1	5.10E-09
	Cr3Pt1	4.50E-09
	Ga1V3	3.40E-09
	Nb3In1	3.20E-09
	Cr3Ir1	1.80E-09
	Be1Mo3	1.60E-09
	Nb3Pt1	4.10E-10
	Pt1Ti3	4.10E-10
	Au1Zn3	6.90E-11
	Cs8Sn46	5.40E-11
	Cs8Sn44	4.50E-12
	Cs4Sn23	1.40E-12
	Mo17Pt3	3.60E-13
Pnma		
	Ca5Ir1	7.40E-04
	Sn4Y5	7.80E-05
	Os1Y3	7.60E-05
	Ca3Pd1	3.60E-05
	Ni1Y3	7.80E-06
	Pt1Sc2	6.90E-06
	Ca2Cu1	4.60E-06
	Au1Mg2	3.20E-06
	Bi3Y5	8.40E-07

Table E.1 continued

	Mg1Pd2	6.70E-07
	Cu8Hf3	6.30E-07
	Au1Ga1	5.40E-07
	Au1Y2	4.60E-07
	AgBa	3.90E-07
	Au4Hf1	7.80E-08
	Pt1Y3	6.80E-08
	Ca3Au1	6.40E-08
	Pb1Sr2	5.90E-08
	Sn1Sr2	4.30E-08
	Ca2In1	3.70E-08
	Rh1Y3	9.30E-09
	Bi3Ni1	7.80E-09
	Ir1Y3	7.80E-09
	Bi3Rh1	5.80E-09
	Rh1Zr1	5.20E-09
	Bi3Ca5	4.80E-09
	Sn1Sr2	4.70E-09
	Ag1Sr1	3.50E-09
	Au1Ba1	1.50E-09
	Sr1Zn1	1.40E-09
	Pt4Sr5	5.90E-10
	Ba2In1	4.20E-10
	Bi3Sc5	3.70E-10
	Pb4Y5	2.40E-10
	Na7Ga13	7.90E-11
	Pb4Sr5	6.90E-11
	Ru1Y3	6.90E-11
	Ba2Pb1	4.80E-11
	Pt3Sr7	4.60E-11
	Pt4Y5	7.90E-12
	Ba2Sn1	6.30E-14
R3-mh		
	Co6Ta7	6.90E-04
	Ni2Ti1	5.40E-04
	Ni3Y1	4.30E-04
	Li8Pb3	8.40E-06
	Ba2Mg17	4.90E-06
	Cr13Ga13	5.80E-07
	Ir3Y1	3.20E-07
	Fe7W6	3.10E-07
	Be17Zr2	8.40E-08

Table E.1 continued

	Ga3Rb1	4.90E-08
	Be17Ti2	4.70E-08
	Ca1Ni3	4.30E-08
	Co3Y1	4.20E-08
	Fe7Nb6	3.50E-08
	Co1Y1	3.40E-08
	Nb6Zn7	2.50E-08
	Fe7Ta6	7.20E-09
	Co7Nb6	5.90E-09
	Co6Nb7	5.30E-09
	Co7Nb6	4.10E-09
	Be17Nb2	3.20E-09
	Ta1Zn2	1.40E-09
	Be3Nb1	6.90E-10
	Ba1Pb3	5.10E-10
	Nb7Ni6	4.80E-10
	Cs1Ga7	4.10E-10
	Be3Ta1	3.60E-10
	Fe6Ta7	3.20E-10
	Fe13Ga13	5.90E-11
	Be3Ti1	5.80E-11
	Co7W6	4.80E-11
	Sn3Sr1	4.60E-11
	Co7Y2	3.70E-11
	Be17Ta2	3.40E-11
	Fe3Sn2	5.90E-13

Table E.2: Diffusion activation energies of intermetallics shortlisted using H solubility at 600 K and 1 atm H_2 as a criterion. All values are in eV.

Intermetallic	Ea	Intermetallic	Ea	Intermetallic	Ea	Intermetallic	Ea
Sc1Fe2	0.19	Pd2Sr1	0.33	Ru2Y1	0.39	Ga2Y1	0.46
Rh1V3	0.21	Cu1Pt1	0.33	Ti2Zn1	0.39	Os4Zr11	0.46
Ni17Y2	0.22	Ba1Pd1	0.33	Hf5Pb1	0.39	Ca5Au3	0.46
Pt8V1	0.22	Co3V1	0.34	Pt1Rh1	0.39	Sr5Tl3	0.47
Fe2Y1	0.23	Ga3Zr5	0.34	Ag1Zr2	0.39	Ca5Ir1	0.47
Mn1V1	0.23	Ni1Ti1	0.35	Cr1Ti1	0.4	In1Sc3	0.47
Mg1Zn2	0.24	Os2Zr1	0.35	Be1Pd2	0.4	Rh3Ti1	0.47
Hf1Ta1	0.24	Be12Pd1	0.35	Cr1Ti1	0.4	Cr2Ti1	0.47
Sc1Fe2	0.24	Ir2Y1	0.35	Ni3V1	0.4	Ca3Pd1	0.47
Ni2Ti1	0.25	Ga3Ir1	0.35	Ni3V1	0.4	Cr2Hf1	0.48
Fe2Hf1	0.26	Ir2Pt1	0.35	Rh1Sc1	0.4	Re1Ti1	0.48
Fe1Ti1	0.26	Ti1V1	0.36	Ru2Sc1	0.41	Ir1Sc1	0.48
Mn1Ti1	0.27	Cu1Zr2	0.36	Hf5Sn4	0.41	Ni2Y1	0.48
Hf1V2	0.27	Hf1Pt3	0.36	Ti1Zn16	0.41	Hf1Ru1	0.48
Cs1Au1	0.27	Ni1Zr2	0.36	Pt1Zr1	0.41	Sc1Y1	0.49
Ru1Zr1	0.28	Cd1Zr2	0.36	Fe1Zr2	0.42	Fe17Y2	0.49
Hf1Mo2	0.28	Fe2Zr1	0.36	Cr2Ti	0.42	In1Zr3	0.49
Sn4Y5	0.28	Ni1Zr1	0.36	Cr2Hf1	0.42	Ca1Pd1	0.49
Mn2Ti1	0.28	Hf1Mo1	0.36	Nb1Zn2	0.42	Ca5Pt3	0.5
Pb2Y1	0.28	Ag1Ti3	0.36	Tl3Y5	0.42	Ca5Pt3	0.5
Ir1Ti1	0.28	In3Sc1	0.36	Ta1V3	0.42	Sn3Zr5	0.5
Pt1Tl2	0.29	Cu4Ti3	0.367	Rh5Zr3	0.43	Ir2Sc1	0.51
Fe1Hf2	0.29	Fe2Ti1	0.37	Co1Ti1	0.43	Ag2Sc1	0.52
Nb1Ti1	0.29	Pt2Ta1	0.37	Ta1Ti1	0.43	Hf1Tc1	0.53
Ni3Y1	0.29	Ni5Y1	0.37	Rh1Y1	0.43	Ni1Sc1	0.53
Hf1Ni1	0.29	Nb1Hf1	0.37	Mo1Ti1	0.43	Cr2Zr1	0.54
Ni1Hf2	0.3	Be5Zr1	0.37	Be12Pt1	0.43	Be1Co1	0.54
Nb1Zr1	0.3	Os2Y1	0.37	Ir3Y5	0.43	Hf1Ir3	0.55
Pt8V1	0.3	Be1Pd1	0.37	Rh2Y1	0.43	Tl1Y1	0.55
Ni2Hf1	0.3	Sc1Zn2	0.38	Sc1Zr1	0.44	Co1Zr1	0.56
Co6Ta7	0.31	Cu1Hf2	0.38	Sn3Y5	0.44	Ga3V5	0.56
Hf1Os2	0.31	Co2Ti1	0.38	Ni2Sc1	0.44	Mg5Pd2	0.57
Ir1Zr1	0.32	Mg2Sr1	0.38	Li2Pt1	0.44	Sn5Ti6	0.61
Be5Sc1	0.32	Ru1Sc1	0.38	Be12V1	0.44	Be2Nb1	0.63
Co2Sc1	0.32	Mo1Zr1	0.38	Co2Nb1	0.45	Ca1Pd5	0.64
In3Y1	0.32	Co2Ta1	0.38	Co2Zr1	0.45	Ru1Ti1	0.64
Cu1Ti2	0.32	Re2Zr1	0.38	Cr2Ta1	0.45	Co3Ti1	0.64
Cu5Y1	0.32	Cd1Hf2	0.38	Au2K1	0.45	Au41Mg13	0.65
Ir1Pt1	0.32	Ir3Sc1	0.38	Ir3Ti1	0.45	Os1Ti1	0.66
Mg1Pd1	0.33	Rh1Zr2	0.39	Ti1Tc1	0.46	Au3Li1	0.67
Hf5Ir3	0.33	Co1Re1	0.39	Ir1Y1	0.46	Os1Zr1	0.78
Os1Y3	0.33	Rh3Zr1	0.39	In1Rh1	0.46	Sn1Ti3	0.86

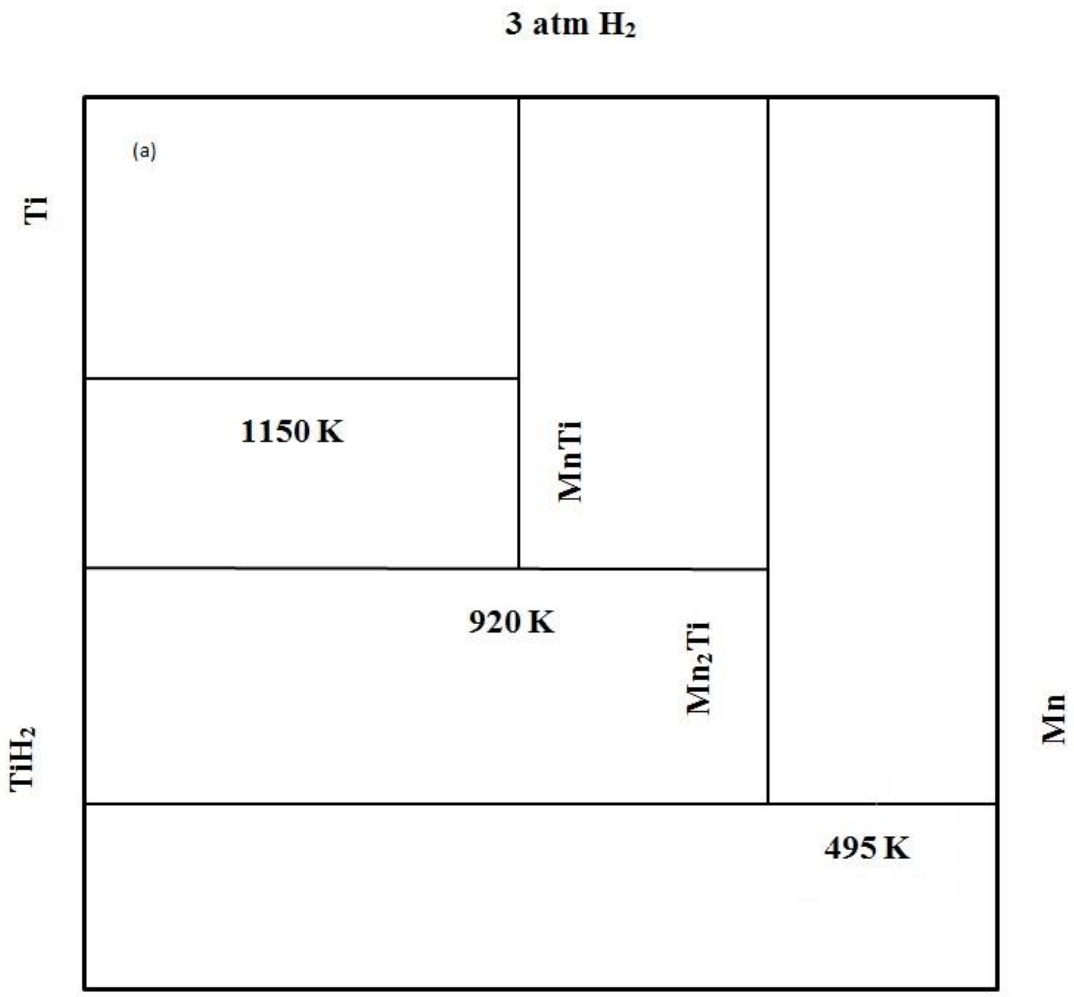
3 atm H_2
(a)
Ti
1150 K
MnTi
920 K
Mn_2Ti
TiH_2
Mn
495 K

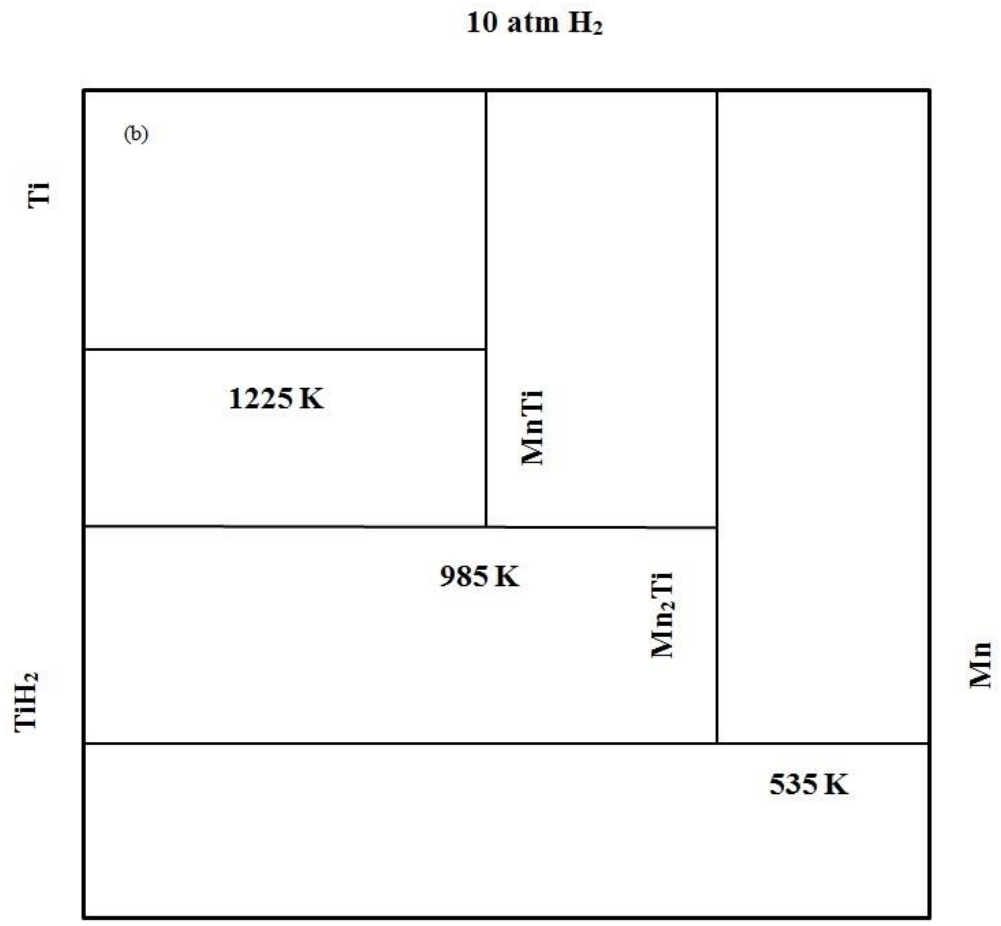

Figure E.3: Mn-Ti-H calculated equilibrium phase diagram at (a) 3 atm H_2 (b) 10 atm H_2.The decomposition temperatures of various phases are shown using horizontal lines. The vertical lines indicate the compounds formed. No entropic (vibration effects) were considered in these calculations.

VITA
NITA CHANDRASEKHAR

Nita Chandrasekhar was born in Jabalpur, Madhya Pradesh, India. She attended schools all over India in Jabalpur, Chennai and Kota. She attended the Birla Institute of Technology and Science, Pilani and received her B.E (Hons.) in Chemical Engineering in 2009. She came to Georgia Tech to pursue a doctorate in Chemical Engineering and began working with Dr. David Sholl in January 2010. Nita is a nature and dog-lover, avid reader, painter, loves to experiment in the kitchen and enjoys swimming and playing tennis. She has also taken up running after coming to Georgia Tech and participates in many runs organized in Atlanta. She is a volunteer at the Atlanta Humane Society and enjoys walking and feeding the dogs in the shelter.